Multiscale modelling of deformation and fracture in metal foams

Kodanda Ram Mangipudi

Multiscale modelling of deformation and fracture in metal foams
Kodanda Ram Mangipudi

PhD Thesis
University of Groningen
The Netherlands

University of Groningen
Zernike Institute
for Advanced Materials

Zernike Institute PhD thesis series: 2012-01
ISSN 1570-1530
ISBN 978-90-367-5163-6

RIJKSUNIVERSITEIT GRONINGEN

Multiscale modelling of deformation and fracture in metal foams

Proefschrift

ter verkrijging van het doctoraat in de
Wiskunde en Natuurwetenschappen
aan de Rijksuniversiteit Groningen
op gezag van de
Rector Magnificus, dr. E. Sterken,
in het openbaar te verdedigen op
vrijdag 20 januari 2012
om 14.30 uur

door

Kodanda Ram Mangipudi

geboren op 8 juli 1979
te Motugudem, Khammam Dt., India

Promotor:	Prof. dr. ir. P.R. Onck
Beoordelingscommissie:	Prof. dr. ir. J.Th.M. De Hosson
	Prof. dr. N.A. Fleck
	Prof. dr. A. Mortensen

ISBN 978-90-367-5163-6

To my parents, my wife
and
my teachers

Contents

Chapter 1

Introduction

We know very little, and yet it is astonishing that we know so much, and still more astonishing that so little knowledge can give us so much power.

Betrand Russel

1.1 Cellular solids

A cellular solid is an interconnected network of struts or plates. Wood, coral, cork, honeycombs and bone are a few naturally occurring examples. Nature uses cellular solids to build optimized structures. Wood is well known to man as a structural material to carry high compressive loads. The long beak of the Brazilian bird Toucan, made of a keratin shell around closed-cell foam of protein, is another excellent example of Nature's design for optimized structures (Seki et al., 2005). Nature optimizes the properties of bone in animals by remodelling its structure to adjust to the changes in loading during their life. Inspired by nature, man has been producing polymeric, ceramic and metallic foams. Figure 1.1 shows a few natural and man-made cellular solids.

Cellular solids can be classified based on various grounds. A primary classification based on the dimensionality distinguishes honeycombs from three-dimensional cellular solids. Honeycombs possess a cellular structure in one plane and extend in the out-of-plane direction. The in-plane cellular structure may be regular or irregular. In three-dimensions, regular lattice structures may be distinguished from random foams. The material distribution in a cellular solid is discontinuous such that material is collected in cell faces, edges and nodes, leaving the rest of the space to air/gas. Based on the material distribution, the cellular structure can broadly be classified into two categories: open-cell and closed-cell. A further internal classification is possible for both these categories on the basis of cell wall connectivity, cell size, cell size distribution and cell shape anisotropy. Cellular solids are also often distinguished based on the constituent material, which could either be metal, ceramic or polymer. Metal foams, cellular solids made of metals or alloys, have been manufactured using various metals. Although the majority of the metal foams are made of aluminium

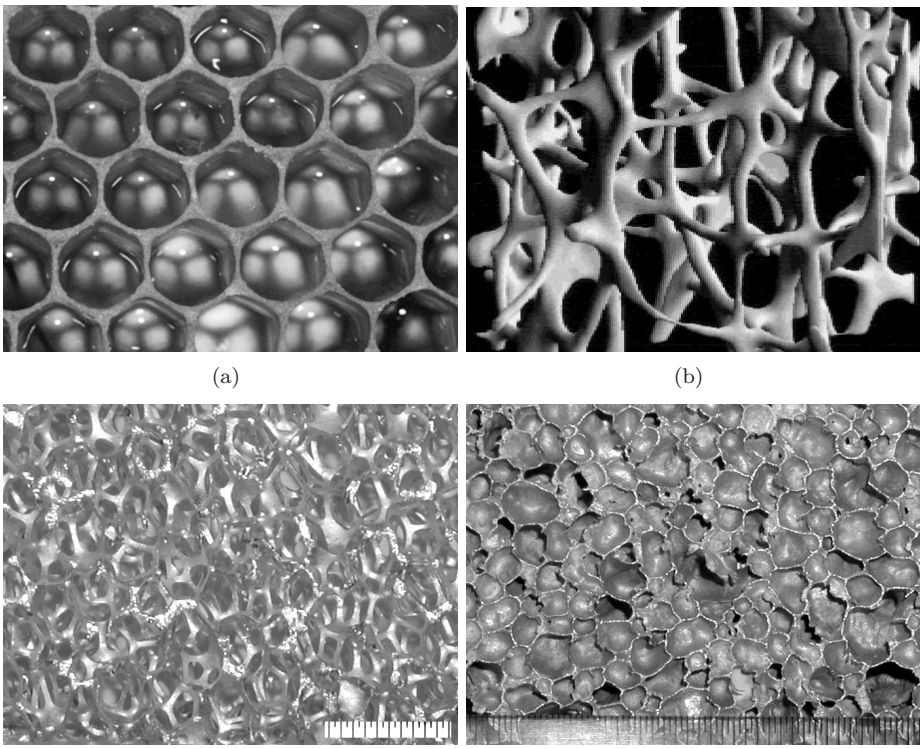

(a) (b)

(c) (d)

Figure 1.1: Examples of cellular solids: (a) beehive with an average cell size of ≈ 4 mm, (b) tomographic reconstruction of a typical trabecular bone from the lumber spine with average trabecular length ≈ 1 mm, (c) open-cell and (d) closed-cell Aluminum foams with cell sizes on the order of a few mm. (Courtesy: (a) Free Online Pictures (2010), (b) Hildebrand et al. (1999), (c) Van Merkerk (2002) and (d) Amsterdam (2008)).

alloys, copper, nickel and steel foams are also commercially available. Cymat, Alulight, Alporas, Duocel and Inco are a few examples of commercially available metal foams. Focus in this thesis is mainly on metal foams, although one chapter will be dedicated to study the mechanical behaviour of trabecular bone.

Metal foams possess attractive thermomechanical properties that find many engineering applications. Among the mechanical properties, the high specific bending stiffness is the most extensively exploited property to produce sandwich panels in light weight structural engineering applications. Metal foams exhibit high efficiency of impact energy absorption at relatively constant stress suitable for crash protection

and blast mitigation systems. Open-cell metal foams have a high thermal conductivity and high heat transferability due to the open-cell structure and high internal surface area and are used as heat sinks in high power electronic devices. The open-cell structure is also exploited in controlling fluid flow and is used as baffles and antisplash structures in space applications. An extensive list of applications of this new class of materials can be found elsewhere (Ashby et al., 2000; Banhart, 2001; Degischer and Kriszt, 2002). This thesis is concerned with their mechanical behaviour only.

Mechanical properties of cellular metals depend on the microstructure of the cell walls, relative density (ratio of the density of the cellular metal to the density of the cell wall material) and the mesoscopic cellular architecture. These primary variables are determined and limited to varying extent by the manufacturing technology. In the following section, the influence of a specific manufacturing technology on the structure of the foam in relevance to the foam's macroscopic mechanical properties is reviewed. For a detailed description of the manufacturing processes, the reader is referred to Banhart (2001), and the references therein.

1.2 The structure of metal foams

Metal foams feature a two level structure, with the cellular architecture at the *mesoscale* and the microstructure of the cell wall material at the *microscale*. The cell type (closed or open), shape and size distribution, the cell wall geometry and relative density define the mesostructure, while the grain size and grain-size distribution, morphology and distribution of secondary phases in the matrix, voids and foreign inclusions make-up the description of the microstructure.

The range of cell size and densities attainable along with the solid material vary with the foam manufacturing technology (see Fig. 1.2). For example, melt gas injection (bubbling gas through molten metal added with viscosity enhancing agents) is developed particularly for closed-cell Al and Mg foams with typical cell sizes in the range from 3 to 25 mm and relative densities in the range from 0.02 to 0.2 (Banhart, 2001), whereas chemical vapour deposition (CVD) of nickel carbonyl on polymer precursors, commercially known as the INCO process, can produce open-cell Ni foam with hollow struts having typical cell sizes of 450-3200 μm and a relative density that can be as low as 0.02 (Paserin et al., 2004).

Each manufacturing technology is responsible for a specific foam morphology depending on the underlying physics of the foaming process. For instance, the closed-cell Cymat foam produced by melt gas injection suffers from a gradient in density, inhomogeneity in pore size and anisotropy in cell shape as a consequence of gravity-induced drainage (Beals and Thompson, 1997; Simone and Gibson, 1998). Moreover, the shear forces due to the conveyor belt that withdraws the foam create a variation

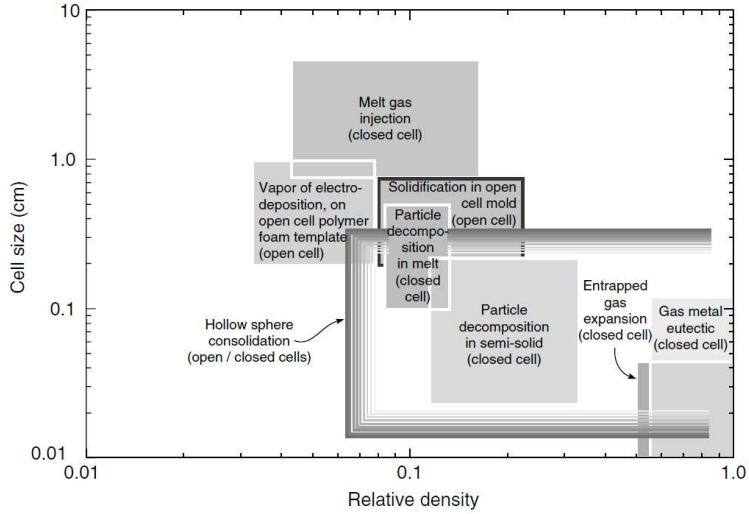

Figure 1.2: The range of cell size and relative densities attainable through different metal foam manufacturing technologies (adopted from Ashby et al. (2000)).

in the cell shape anisotropy through the thickness of the panel. The anisotropy in cell shape will lead to anisotropy in the mechanical properties (Beals and Thompson, 1997; Benouali et al., 2005). Defects like cell wall corrugations were also observed, which have been linked to the liquid foam handling methods. Due to the inhomogeneity and defects present in these foams, the elastic modulus and the collapse stress remain lower compared to aluminium alloy foams with an isotropic cell structure, such as Alporas (Simone and Gibson, 1998). The closed-cell Alporas foam is produced by foaming close to the melting temperature of aluminium. Ca is added to enhance the viscosity and the controlled decomposition of TiH_2 is employed to release hydrogen gas. Due to its significantly homogeneous structure and reduced defects compared to Cymat foam, Alporas displays much better mechanical properties (Simone and Gibson, 1998). Alulight foams are produced by a powder compaction route to achieve a homogeneous distribution of the foaming agent, typically TiH_2, and does not show any anisotropy in the cell structure and mechanical properties (Andrews et al., 1999). Another example of a strong influence of the structure on the mechanical properties is the GASAR foam, which shows a peculiar compressive stress strain response due to the highly elongated pores with inhomogeneous pore size produced by directional solidification of metal-hydrogen eutectic melts under high pressure (Simone and Gibson, 1997). On the other hand, casting and deposition techniques exploit the matured technologies of polymer foam production and can produce foams

with a narrow cell size distribution by copying the polymer foam structure; however, these are limited to open-cell morphologies. Examples are Duocel foam produced by investment casting and INCO Nickel foam prepared by CVD or electrodeposition. The anisotropy of the polymer foams is thus inherited, making them mechanically anisotropic.

The microstructure of the cell wall material is different from that of the corresponding metal or alloy in the bulk form due to different solidification conditions and additives and impurities introduced in the foaming process. Additional materials have often been added to the melts to gain more control on the foaming process to produce a better foam structure. Silicon carbide, aluminium oxide or magnesium oxide particles are used as foam stabilizing additives to increase the melt viscosity. These particles are embedded in the cell walls near the surface (Prakash et al., 1995; Simone and Gibson, 1998; Amsterdam et al., 2006a). Sharp needle-like Al_5FeSi phases have been reported to be formed from the presence of iron, a contamination that severely embrittles the material (Amsterdam et al., 2006a). In Alporas foams, Ca is generally added to enhance the viscosity. This forms Al_4Ca, Al_3Ti and $Al_{22}CaTi_2$ inside the grains with particle-like morphologies (Sugimura et al., 1997; Simone and Gibson, 1998; Markaki and Clyne, 2001; Amsterdam et al., 2006b). Since the cell wall thickness is small, the cell wall contains one to two grains across its minimum thickness. The struts in open-cell Duocel foam also usually contain one grain across their thickness and feature a bamboo-like grain structure along its length. Iron is also a common impurity in these foams, which is responsible for two kinds of AlFeSi precipitates, one with a diffuse matrix-precipitate interface having a complex morphology (α-AlFeSi) and the other with a sharp interface (β-AlFeSi) mostly covering the grain boundaries.

1.3 Deformation and failure in metal foams

Fig. 1.3 shows the typical uniaxial tensile and compressive behaviour of a foam. Compressive loading of metal foams has received a lot of attention in the literature revealing many *mesoscopic* deformation mechanisms. In compression, after a linear regime, a ductile foam (e.g. Alporas) exhibits a nearly constant plateau stress extending up to large overall strains. Local inhomogeneities in density, cell shape and cell wall curvature are thought to initiate early local yielding during elastic loading (almost immediately after loading) of Cymat (Prakash et al., 1995; Simone and Gibson, 1998) and Alporas (Simone and Gibson, 1998) foams producing a significantly higher unloading modulus compared to the loading modulus (Sugimura et al., 1997; Simone and Gibson, 1998). In Duocel foams, however, both the loading and unloading moduli are equal, which can be connected to the absence of curved struts

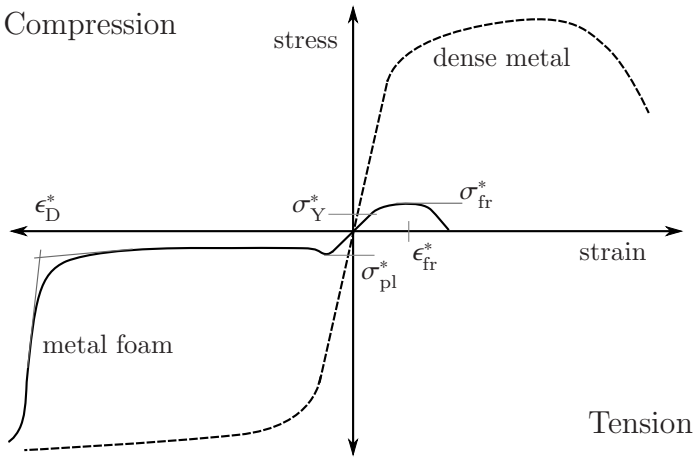

Figure 1.3: Schematic stress-strain curves of ductile dense and cellular solids.

(Andrews et al., 1999).

The primary deformation mechanisms under compression are cell wall bending and buckling (Zhou et al., 2004). During the elastic deformation stage, the strains are more or less homogeneous throughout the structure. Localized deformation bands begin to form at the onset of non-linearity (Bart-Smith et al., 1998; Bastawros et al., 2000). Defects like missing or fractured cell walls provide the nucleation centers for the deformation bands (Silva and Gibson, 1997a). In addition to these defects, elliptical cells with T-shaped cell wall junctions and cells with non-planar cell walls are the critical cells which yield/fail first. The surrounding cells are then forced to deform in a coordinated manner to accommodate these deformations. This leads to the formation of deformation bands (roughly at the peak stress) with local strains that can be one order of magnitude larger than the applied strain (Bart-Smith et al., 1998). These deformation bands cover the entire cross section of the specimen with their normal within 20° (and in a few instances close to 40°) to the loading direction. Three principal modes of cell-level deformation within these bands have been reported: (a) distortion only, (b) distortion combined with rotation and (c) distortion combined with shear. With further straining new bands originate in a similar manner as the initial band and are spaced with a characteristic separation distance (Bastawros et al., 2000) in contrast to the deformation in regular honeycombs, where a single deformation band spreads and consumes the entire gauge length. The characteristic spacing is related to the specific material volume above and below each band to elastically accommodate the deformation in these bands.

As the macroscopic straining is continued, cell wall collapse decreases the macro-

scopic stress. When the cell walls inside a deformation band come in contact with each other, the macroscopic stress will again start to increase. Formation of more than one collapse band produces oscillations in the stress-strain curve around the plateau stress. Serrations in the compressive stress-stain curve are characteristic of brittle failure of the cell walls due to precipitates, for example in Cymat foams, while smooth oscillations are a signature of a more ductile foam (e.g. Alporas) (for example, see Sugimura et al. (1997) for typical stress-strain curves). Such a plastic deformation in foams is not macroscopically volume conserving and very low plastic Poisson ratios, as low as 0.01, have been reported at low densities (Deshpande and Fleck, 2000). When all the foam material is consumed into these bands, densification begins and the stress rises quickly (see Fig. 1.3). The plateau/plastic collapse stress $\sigma^*_{\rm pl}$ and the densification strain $\epsilon^*_{\rm D}$ together form a combination with high engineering significance in energy absorption applications.

In contrast to the compression failure mode, the mechanisms that lead to tensile failure are less well studied. In general, deformation has been found to be relatively homogeneous under tension and no strain localization has been observed without the occurrence of damage. Instead, a uniform distribution of isolated high strain regions of approximately one cell in diameter, formed presumably from the stretching of curved cell walls, have been reported by Motz and Pippan (2001). In random structures, plastic deformation usually follows the weakest path and may be altered by the presence of structural defects (Silva and Gibson, 1997a). In tension, the redistribution of active strain regions is attributed to the local hardening caused by the stretching of cell walls (Motz and Pippan, 2001). The relative distribution of the material in the plateau borders and cell wall (Warren and Kraynik, 1987; Harders et al., 2005; Kim and Al-Hasani, 2002, 2001; Gong et al., 2005) and the anisotropy in cell shape also have a strong influence on the elasto-plastic properties of foams (Silva et al., 1995; McCullough et al., 1999b; Nieh et al., 2000; Amsterdam et al., 2008d). Clearly, the mesoscopic structure introduces a characteristic length scale (the cell size), which becomes important especially when dealing with structures having dimensions on the order of the cell size or in case of inhomogeneous deformation at localization bands, cracks, notches or holes.

In random foam structures, it has been established that the cell wall bending (and cell face stretching if the cells are closed) is the dominant deformation mode under uniaxial loading. However, as the hydrostatic component of the stress increases, stretching deformation becomes important. For example, in regular hexagonal honeycombs subjected to equi-biaxial loading, the bending moment in the members vanishes, leaving the members under axial loading. However, structural defects like missing cell walls, cell wall curvature and wavyness (corrugations) of the walls induce bending in the structure even under hydrostatic loading conditions and knock-down

the hydrostatic strength (Andrews et al., 1999; Chen et al., 1999).

At the *microscopic* length scale, i.e. at length scales smaller than the strut or cell wall thickness, the constitutive behaviour of the material is directly related to its internal microstructure characterized by the matrix phases, the grain structure, non-metallic inclusions and precipitates. The specific strut or cell wall microstructure is a direct consequence of the specific production method. Microscopically, second phase particles are often found responsible for the fracture initiation. In metal foams made from (recycled) metal matrix composites, failure occurs by cleavage of the brittle SiC particles and β-AlFeSi precipitates and propagates through the ductile aluminium matrix joining other particles, rendering the foam to be very brittle (Amsterdam et al., 2006a). In Alporas, microcrack formation due to particle cleavage of Ca-containing precipitates, followed by the ductile failure of the matrix between the precipitates leads to cell wall fracture. Similarly, in Duocel foams, the grain boundary β-AlFeSi precipitates are the primary failure initiation sites (Amsterdam et al., 2006c). Struts that contain no large precipitates are characterized by a ductile failure mode found in pure metals, involving necking down to a point due to extensive slip (Marchi et al., 2004; Amsterdam et al., 2006c; Aly et al., 2009). When fine precipitates are present in foams like Alporas, typical dimpled fractured surfaces are found (Sugimura et al., 1997; Paul et al., 1999), indicative of void growth and coalescence. High Silicon content has also been reported to enhance brittleness in similar classes of open-cell foams (McCullough et al., 1999b; Marchi et al., 2004). These findings clearly emphasize that the deformation and failure mechanisms at the strut level are strongly correlated to the cell wall microstructure and the foam manufacturing process.

Since the processing parameters such as foaming temperature, viscosity enhancing additions and chemical foaming agents can only be varied within a narrow range to generate a uniform cell-structure, one often resorts to post-processing techniques to alter the physical microstructure of the cell-wall material. Heat treatments are generally adopted for both open-cell and closed cell foams to increase the overall flow strength and energy absorption efficiency (see e.g. Thornton and Magee (1975); Zhou et al. (2005); Krishna et al. (2007); Amsterdam et al. (2008b)). Tempering heat treatments for Al-alloys usually result in a decreased strain hardening capacity and ductility while enhancing the yield and fracture strengths. On the other hand, annealing produces exactly the opposite effect. Krishna et al. (2007) observed that annealing of the as-cast microstructure in Duocel leads to grain coarsening and precipitate coarsening with an associated degradation in the plastic collapse stress. A change in the precipitate nature and/or distribution achieved through heat treatment may also lead to different fracture mechanisms. Clearly, the choice of processing parameters and post-processing treatments affect the internal microstructure of the

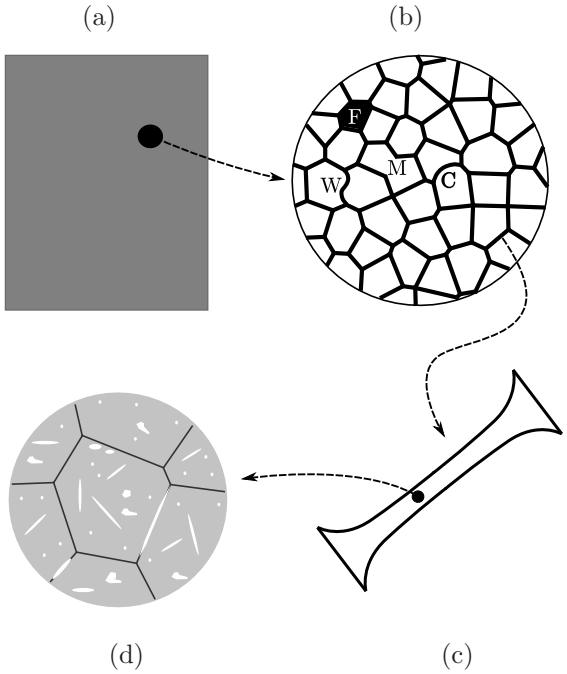

Figure 1.4: Size scales involved in foam structures. (a) bulk foam as continuum, (b) cellular structure with cell level defects: F – filled cells, M – missing cell walls, C – curved cell walls, W – cell wall wiggles, (c) cell walls as plates or beams and (d) material behaviour governed by the cell wall microstructure which includes a combination of grain boundary precipitates, brittle precipitates, second phase particles, non-metallic inclusions, voids, etc. (white) inside a ductile matrix (gray).

struts and cell walls, and through this, the solid material's yield stress, hardening behaviour and fracture resistance. Not only from a processing point-of-view, but also for an enhanced fundamental understanding it is of interest to investigate how a change in microscopic properties carries over to the macroscopic scale through an alteration of the mesoscopic damage and fracture mechanisms.

1.4 Scope of the thesis

The multiple length scales involved in the foam structure (as discussed in the previous sections) are summarized in Fig. 1.4. At the macroscopic scale (see Fig. 1.4a), i.e. when the structural dimensions are much larger than the cell size, continuum models have been developed (e.g. Deshpande and Fleck (2000); Miller (2000) and Badiche

et al. (2000)), which heavily depend on large experimental data needed to extract the phenomenological parameters (see section 2.1.1 for a brief review of various modelling approaches). The amount of experimental data required can be greatly reduced with the help of simple mechanistic models based on the deformation mechanisms (Gibson and Ashby, 1997) at the scale of Fig. 1.4c. These well established and extensively verified scaling laws express the foam's elastic and plastic properties in terms of the constituent solid's elasto-plastic properties and the foam relative density, and only require a limited set of experiments to determine the dimensionless pre-factors that are functions of the cellular architecture only. At this scale discrete finite element modelling has been proven useful. For example, the influence of cell level defects and structural randomness (see Fig. 1.4b) on the elastic and yield behaviour has been intensively studied (e.g. Chen et al. (1999); Zhu et al. (2001a)). We aim to extend the scope of these mechanistic laws up to the fracture strength using a similar discrete modelling approach, where the microscopic failure process (Fig. 1.4d) will be incorporated by an appropriate softening relation.

The goal of this thesis is therefore to investigate the role of the cell wall microstructure and cellular architecture on the macroscopic mechanical behaviour and the mesoscopic mechanisms of deformation and fracture in cellular metals under tension. The approach is based on a discrete representation of the cellular architecture, with the mesostructure represented by Voronoi tessellations. Structural randomness will be introduced by controlling the initial Voronoi seed distribution, whereas the structural anisotropy will be produced by an affine scaling of the Voronoi vertices. The struts will be modelled as beams with varying cross section. The cell wall microstructure will be represented through an appropriate constitutive law incorporated at the material point level inside the struts, accounting for power-law strain hardening and damage. We will develop a multiscale finite element model to study how a variation in the properties of the microstructure (the elastoplastic-fracture properties of the strut material) and the architectural parameters (structural anisotropy, randomness and strut profile) carries over to the macroscopic scale in defining the foam's elastoplastic-fracture response.

1.5 Outline of the thesis

The outline of the thesis is as follows. In chapter 2, the different approaches in the literature to model the mechanical behaviour of cellular solids will be briefly reviewed (see section 2.1). Subsequently, two discrete models based on Voronoi tessellations will be presented in sections 2.2 and 2.3, with the struts being represented by Euler-Bernoulli beams in both models. The first model will be formulated within a viscoplastic framework. The governing plastic constitutive laws relating the stress-

resultants to the axial strain and curvature will be derived in closed-form. Possible extensions to include damage within the viscoplastic framework and their computational limitations will be discussed as well. In the second multiscale model, plastic deformation and damage in the strut are captured using a layered beam approach in a co-rotational beam formulation. Following Zhu et al. (2001a), we will discuss the details of the generation of Voronoi structures with controlled randomness in section 2.4. We will also describe a strain mapping procedure similar to the experimental digital image correlation technique. We will develop a cell-level stress mapping procedure. These two mapping tools will be used to analyse the mesostructural deformation mechanisms in the subsequent chapters.

Since plastic deformation precedes damage initiation in ductile metals, the fracture behaviour can be expected to be influenced by the strain hardening behaviour. Hence, we first explore the plastic deformation in regular and irregular foam structures in chapter 3. By closely following the plasticity development inside the struts and at the scale of the cellular structure, we will analyse the microstructural mechanisms leading to macroscopic hardening. We find that strut reorientation causes additional hardening which interacts with the intrinsic strain hardening. We capture the modelling results into an overall hardening exponent, in which the geometric contribution to hardening will be isolated from the intrinsic material hardening.

Chapter 4 addresses uniaxial tensile fracture in ductile metal foams. We will focus on factors influencing damage initiation and the fracture strength. First, we will analyse the damage process in the pre-peak and post-peak regimes in both regular and random structures and identify the mechanisms responsible for overall failure. The results of the parametric study will be presented in two parts. The first part will investigate the influence of the solid material properties and microstructure (such as the strain hardening, critical fracture stress and the presence of brittle precipitates) on damage initiation and fracture strength. In the second part, architectural parameters such as the structural randomness, anisotropy and the size of the specimen relative to the cell size are varied. In both parts, we will analyse how the primary dependence of the macroscopic properties on the relative density will change with a variation in a given material/structural parameter. Simple unit cell simulations will be used to elucidate the microstructural mechanisms. We will also compare analytical relations for yielding in affinely-scaled anisotropic regular hexagonal structures with our simulation results, which are found to very well capture the fracture response of anisotropic irregular structures. We will also simulate the effect of heat treatment, where more than one material property is changed simultaneously. Finally, the results from the two parts will be compiled into scaling relations for the overall fracture stress and fracture strain as a function of the relative density, architectural anisotropy, solid hardening and fracture parameters.

In chapter 5, we will use the model of section 2.3 to study the effect of notches and cracks on the overall fracture response of double edge notch (DEN) and central crack panels (CCP). We will study the effect of finite sample dimensions by independently varying the crack length and the ligament width in DEN and CCP specimens, in order to explore the governing mesoscopic mechanism in notched samples. In this chapter, we will also analyse the interaction of stress-free specimen edges with the central cracks in CCP specimens and its influence on the net section fracture stress.

In chapters 3, 4 and 5, we have studied ductile metal foams, whose constituent material shows extensive strain hardening. In contrast, we will study the mechanical behaviour of trabecular bone in chapter 6, where the trabecular matrix behaviour is quasi-brittle. By replacing the ductile (elastoplastic-fracture) material law by an elastic-fracture behaviour in the layered beam model, we explore the effect of trabecular-level properties, such as the trabecular cross section, fracture strength and specific fracture energy, on the bone mechanical behaviour. Based on these trends, the effectiveness of two osteoporosis medications will be discussed.

Finally, the results will be summarized and their technological implications will be discussed in chapter 7.

Chapter 2

Multiscale models for the elasto-plastic fracture of metallic foams

Nature's grand book, which stands continually open to our gaze, is written in the language of mathematics. Its characters are triangles, circles, and other geometrical figures, without which it is humanly impossible to understand a single word of it.

Galilio Galilei

This chapter presents the two multiscale modelling frameworks developed in this thesis. After a brief review of the various modelling approaches, a model is presented within a viscoplastic framework, which will be used to study strain hardening in chapter 3. Its extension to include damage will be presented in Appendix C. Following a discussion on the limitations of the former model, we present a computationally less expensive model based on a cross-sectional discretization of the beam element. This second model will be used subsequently in chapters 4, 5 and 6 to account for strut damage. Subsequently, the procedure of generating Voronoi tessellations with controllable randomness will be discussed. At the end of this chapter, tools for stress and strain mapping suitable for two-dimensional Voronoi structures will be developed, which will be used to study the mesoscopic deformation in the structures.

2.1 Modelling approaches

The modelling approaches for cellular materials found in the literature mainly belong to two categories: (a) phenomenological models and (b) mechanistic models. Phenomenological models aim at incorporating the macroscopic phenomena through

model parameters. Often, these parameters are introduced for mathematical convenience rather than for physical reasons. Extensive experimental tests are required to effectively determine these parameters. In mechanistic models, microscopic phenomena are modelled by considering the microstructure and physical mechanisms. Hence, mechanistic models offer the advantage of predicting the macroscopic properties from the constituent material and microstructural morphology. For random structures analytical methods are not feasible and numerical (finite element) methods are needed that are generally computationally expensive at large structural dimensions, whereas phenomenological models provide relatively inexpensive and easy to use material models well suitable for large scale continuum finite element analyses.

2.1.1 Phenomenological models

Macroscopic phenomena that have been attempted to be incorporated into various phenomenological models include tension-compression yield asymmetry, pressure sensitivity during plastic deformation (introduced through the so-called "plastic Poisson's ratio" or the shape of the yield surface in the deviatoric-hydrostatic stress space) and anisotropy. Different variants of the isotropic Drucker-Prager (DP) yield criterion have been employed for foams. An early attempt using a simple DP-type yield surface for metallic foams was made by Sugimura et al. (1997), where the shape of the elliptical yield surface is determined by the ratio of the hydrostatic to shear yield stress. Miller (2000) developed a constitutive model based on the extended DP yield surface with an associative flow rule, which accounts for the tension-compression yield asymmetry and allows independent control of the plastic compressibility. This includes the GAZT yield surface (Gibson et al., 1989) as a special case. Deshpande and Fleck (2000) developed a yield surface for foams, which can either evolve in a self-similar fashion or can show differential hardening. A few more attempts in the spirit of the Deshpande and Fleck (2000) constitutive model can also be found in the literature (Chen and Lu, 2001; Wicklein and Thoma, 2005). An anisotropic generalization of the Deshpande and Fleck (2000) model was introduced by Badiche et al. (2000) based on a non-linear hardening rule. Strain softening was also incorporated later and the classical continuum was extended to a micromorphic continuum to include a length scale (Dillard et al., 2006). A more general anisotropic form is also possible (Liu et al., 1997) for which all the above yield surfaces can be regarded as special cases.

2.1.2 Mechanistic models

The first (to the knowledge of the author) and most frequently cited theory for the mechanical response of a cellular solid is due to Gent and Thomas (1959), who devel-

oped an irregular open-cell model based on a single strut (envisioned as a ball-fiber connection) unit cell with an assumed affine deformation. Assuming small strains, they derived a strain energy function for the bulk foam and the effective moduli are deduced from the constitutive relation obtained from the strain energy function. A similar single strut model has also been developed by Christensen (1986). An inherent drawback of the above single strut models is that the strut connectivity is not considered and no force equilibrium among the connected members is accounted for. Only the stretching of the struts is assumed and the bending deformation is completely absent in these models. This inevitably leads to the result that the effective moduli vary linearly with the relative density, which clearly is inconsistent with the experimental observations. Grenestedt (1998) has developed another theory deducing the elastic moduli from a single strut model of a three-dimensional open-cell foam with wavy imperfections. Warren and Kraynik (1987) developed a micromechanical model of a regular hexagonal structure represented by a unit cell of three connected struts. Unlike the single strut models, non-affine bending deformation of the struts is accounted for. They have also analysed the effect of a nonuniform strut geometry. Later, a four strut unit cell model was developed along similar lines for three-dimensional foams (Warren and Kraynik, 1988). At large deformations, they neglect bending and assume stretching to be the dominant deformation mode and developed a nonlinear elastic constitutive theory from the total strain energy function of a pin-jointed three strut unit cell (Warren et al., 1989). Later, Wang and Cuitiño (2000) included bending as well to obtain a constitutive model for nonlinear elastic deformation by minimizing the strain energy.

Gibson et al. (1982) have ascertained the importance of bending as the dominant deformation mechanism in low relative density cellular structures at small deformations. Based on these arguments they have developed a microstructural model for a regular hexagonal honeycomb with uniform strut thickness using beam mechanics. The effective moduli have been obtained as functions of the relative density. Using limit analysis, the plastic collapse stress has also been related to the relative density for elastic-perfectly plastic constituent behaviour. For three-dimensional cellular structures, dimensional arguments have been used to obtain similar relations (Gibson and Ashby, 1982). Although they have considered a cubic representative cell, as they also note, their findings of the dimensional analysis are not limited by the cell shape. The contribution of the cell geometry to the mechanical properties is collected in a dimensionless pre-factor, which is constant for a given type of foam. This makes these scaling laws readily applicable and convenient to compare experimental data for a wide range of foam geometries. Based on this approach, they have also studied nonlinear elastic properties, multiaxial loading and fracture properties of two- and three-dimensional cellular materials. A comprehensive collection of their work with

references to extensive supporting experimental data can be found in Gibson and Ashby (1997).

Extensions to the Gibson et al. (1982) analysis can be found in the literature. For example, Harders et al. (2005) extended it to parabolic strut profile while studying elastic properties. Extensions to columnar structures with non-uniform strut profiles can be found in Kim and Al-Hasani (2001) and Kim and Al-Hasani (2002). Marchi and Mortensen (2001) have derived a uniaxial stress-strain relation (at small deformations) for a foam with power-law hardening material. The effect of plateau borders and curved cell walls has been included by Chuang and Huang (2002) and Huang and Chang (2005), respectively. Size effects on the elastic and plastic properties have been studied by Onck et al. (2001).

Nevertheless, idealization of the foam microstructure to be periodic cannot capture the natural variations in the foam morphology and an increasing complexity can be noticed in the extensions of the Gibson and Ashby (1997) models and it is even impossible to obtain closed form solutions for fully random microstructures. To this end, finite element models have been proven to be insightful (to mention a few, Chen et al. (1999); Zhu et al. (2001a); Schmidt et al. (2003); Tekoğlu and Onck (2005)). The random structure models, usually based on Voronoi tessellations, possess the inherent capability of capturing both size effects and the natural variation of the microstructural morphology, which is also the approach taken in this thesis.

2.2 Elastoplastic model within a viscoplastic framework

A discrete model of the two-dimensional open-cell foam will be presented in this section. We use two-dimensional Voronoi tessellations to describe the structure of the foam network. Since most of the deforming struts in an open-cell foam are slender, we neglect any shear deformation in the struts and treat them as Euler-Bernoulli (EB) beams. In the following, elasto-plastic Euler-Bernoulli beam equations will be developed. The plastic constitutive relations for the axial force and moment as functions of the axial and bending strains are derived under both uncoupled and coupled strain assumptions.

The deformation of the beam is described in terms of the axial and transverse displacements of its axis $\mathbf{u} = \{u, v\}$ in the local co-ordinate system. The characteristic strains, given by the axial strain $\bar{\epsilon}$ and the curvature κ, contribute to the strain ε at

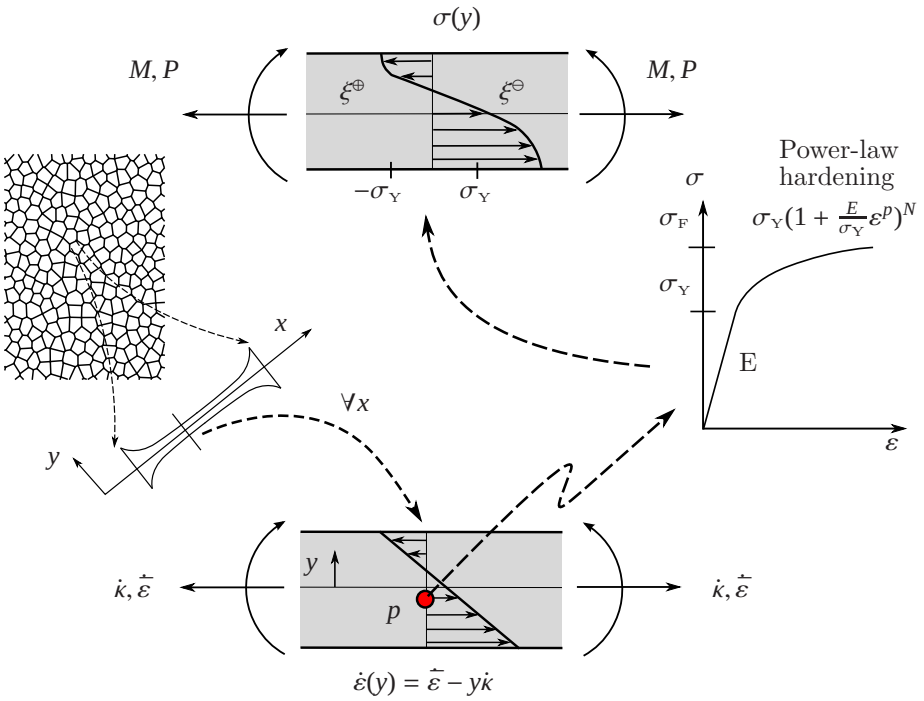

Figure 2.1: Schematic diagram of the model. From the updated strain distribution across the thickness of the strut (bottom), the elastic-plastic boundary ($\xi^{\oplus}$ and $\xi^{\ominus}$) is known. The stress resultants, P and M, are obtained by integrating the stress state over the beam cross section for a given elastic-plastic constitutive behaviour (right) at any material point $p(x,y)$.

any material point $p(x,y)$ (which was at $p(X,Y)$ in the reference configuration $\overline{V}$) as

$$\varepsilon = \frac{du}{dX} + \frac{1}{2}\left(\frac{dv}{dX}\right)^2 - y\frac{d^2v}{dX^2} = \bar{\varepsilon} - y\kappa. \tag{2.1}$$

The internal virtual work can be written as

$$\delta W_i = \int_{\overline{V}} \delta\varepsilon\, \sigma\, d\overline{V} \tag{2.2}$$

where σ is the stress at the point $p(x,y)$ (see Fig. 2.1). It may be noted here that the Cauchy stress σ can be taken to be equal to the Piola-Kirchhoff II stress τ due to the assumption of constant cross sectional area. From Eq. 2.1 and Eq. 2.2 and for a beam of rectangular cross section with thickness t and out-of-plane thickness b, we

can write

$$\delta W_i = \int_X (\delta\bar{\varepsilon} P + \delta\kappa M) dX, \tag{2.3}$$

where

$$P = b\int_y \sigma\, dy \quad \text{and} \quad M = -b\int_y y\,\sigma\, dy. \tag{2.4}$$

Again, use is made of the fact that $dA = b\,dY = b\,dy$. If the strains are elastic, assuming a linear elastic material behaviour ($\sigma = E\varepsilon$) Eq. 2.4 becomes

$$P = EA\bar{\varepsilon} \quad \text{and} \quad M = EI\kappa, \tag{2.5}$$

where E is the Young's modulus, $A = bt$ is the cross sectional area and I is the moment of inertia.

One approach to obtain plastic constitutive relations is (a) to assume that during the plastic deformation the assumptions of the EB beam deformation continue to be valid, (b) to assume uncoupled characteristic strains and (c) to neglect the gradual elastic-plastic transition. In that case, the moment M is defined to be a function of curvature κ alone, while the normal force P is defined to be dependent on only the axial strain $\bar{\varepsilon}$. Then assumption 'c' leads to instantaneous yielding of the entire cross section either when the moment M reaches the plastic section moment $M_P = \frac{1}{4}bt^2\sigma_Y$ or when the normal force P equals the yield force $A\sigma_Y$ with σ_Y being the yield stress. Instantaneous yielding means that the linear stress profile across the thickness suddenly switches to a profile such that $|\sigma(y)| = \sigma_Y$. With these assumptions, hardening laws for the normal force and the moment can be obtained (Mangipudi and Onck, 2006). An improvement to this approach is made by accounting for the gradual plastification of the cross section (i.e. dropping the assumption 'c'). This will be presented in the following section 2.2.1, while in section 2.2.2 we will drop assumption 'b' as well and account for coupled characteristic strains.

2.2.1 Uncoupled normal and bending strains

For the uncoupled strain assumption, the onset of yielding is defined by either $|\bar{\varepsilon}| = \varepsilon_Y$ or $|t\kappa/2| = \varepsilon_Y$, with $\varepsilon_Y = \sigma_Y/E$ and correspondingly we require plastic constitutive laws for either the normal force or the moment.

When the yielding occurs due to bending, we require a relation for the moment in the plastic range. The strain at a material point due to curvature can be written as

$$\varepsilon = -y\kappa \tag{2.6}$$

and the stress corresponding to the strain due to curvature is σ. Note that this

stress profile is symmetric. The stress σ will be given by the material's elasto-plastic behaviour. First we consider linear strain hardening for the material given by

$$\sigma = \begin{cases} E\varepsilon & \forall \quad 0 \le |\varepsilon| \le \varepsilon_Y, \\ \dfrac{\varepsilon}{|\varepsilon|}(\sigma_Y + H|\varepsilon^p|) & \forall \quad |\varepsilon| > \varepsilon_Y. \end{cases} \tag{2.7}$$

Here H is the plastic tangent modulus and $|\varepsilon^p| = |\varepsilon| - \varepsilon_Y$ is the accumulated strain after yielding. The curvature of the beam at the onset of yielding is $\kappa_0 = \frac{\kappa}{|\kappa|}(2\varepsilon_Y/t)$. Note that by definition κ_0 has the same sign as the curvature. With plastic deformation, the elastic-plastic boundary, where $|\varepsilon| = \varepsilon_Y$, moves inwards (see Fig. 2.1). The point of yielding on the positive side of y is $\xi = \frac{t}{2}\frac{\kappa_0}{\kappa}$. The moment can be obtained by integrating the stress σ through the thickness of the beam. From Eqs. 2.6 and 2.7 and exploiting the symmetry in the stress profile, the moment M can be written as

$$M = -2b\int_0^{\frac{t}{2}} \sigma\, y\, dy = -2b\left[-\int_0^{\xi} E\kappa y^2\, dy + \int_{\xi}^{\frac{t}{2}} \frac{\kappa}{|\kappa|}\left(\sigma_Y(1-\eta) + H|\kappa y|\right) y\, dy\right] \tag{2.8}$$

where $\eta = H/E$. Therefore for the entire range of κ, the moment-curvature relation is

$$M(\kappa) = \begin{cases} EI\kappa & \forall \quad 0 \le |\kappa| \le |\kappa_0|, \\ EI\kappa\left[(1-\eta)\left(\dfrac{\kappa_0}{\kappa}\right)^3 + \eta\right] + \dfrac{\kappa}{|\kappa|}M_P(1-\eta)\left[1 - \left(\dfrac{\kappa_0}{\kappa}\right)^2\right] & \forall \quad |\kappa| > |\kappa_0|. \end{cases} \tag{2.9}$$

For the special case of elastic-perfectly plastic behaviour, the moment-curvature relationship can be found by setting $\eta = 0$. For $\eta = 0$ and in the limit $\kappa \to \infty$, the moment $M \to M_P$.

Similarly, the hardening relation for the axial force can be obtained by integrating the stress due to the axial strain $\varepsilon = \bar{\varepsilon}$. For linear hardening given by Eq. 2.7, we have

$$P(\bar{\varepsilon}) = \begin{cases} EA\bar{\varepsilon} & \forall \quad 0 \le |\bar{\varepsilon}| \le \varepsilon_Y, \\ \dfrac{\bar{\varepsilon}}{|\bar{\varepsilon}|}A\left(\sigma_Y + H|\bar{\varepsilon}^p|\right) & \forall \quad |\bar{\varepsilon}| > \varepsilon_Y. \end{cases} \tag{2.10}$$

Similarly, for power-law strain hardening described by

$$\sigma = \frac{\varepsilon}{|\varepsilon|}\sigma_Y\left(1 + \frac{E}{\sigma_Y}|\varepsilon^p|\right)^N \quad \forall \quad |\varepsilon| > \varepsilon_Y, \tag{2.11}$$

the plastic moment and the normal force relationships take the following form:

$$M(\kappa) = EI\kappa\left(\frac{\kappa_0}{\kappa}\right)^3 + \frac{\kappa}{|\kappa|}\frac{2}{2+N}M_P\left(\frac{\kappa}{\kappa_0}\right)^N\left[1 - \left(\frac{\kappa_0}{\kappa}\right)^{2+N}\right] \quad \forall \quad |\kappa| > |\kappa_0|, \tag{2.12}$$

and

$$P(\bar{\varepsilon}) = \frac{\bar{\varepsilon}}{|\bar{\varepsilon}|} A\sigma_Y \left(1 + \frac{E}{\sigma_Y}|\bar{\varepsilon}^p|\right)^N \quad \forall \quad |\bar{\varepsilon}| > \varepsilon_Y. \tag{2.13}$$

2.2.2 Coupled normal and bending strains

In this approach, the stress resultants are dependent on both $\bar{\varepsilon}$ and κ. The strain at a material point $p(x, y)$ is now given by

$$\varepsilon(y) = \bar{\varepsilon} - \kappa y. \tag{2.14}$$

The stress profile $\sigma(y)$ is therefore asymmetric. The quantities $\xi^{\oplus}$ and $\xi^{\ominus}$ in Fig. 2.1 represent the position of the boundaries between the elastic and plastic regions of the beam and are given by

$$\xi^{\oplus} = \frac{\sigma_Y}{E|\kappa|} + \text{Sign}(\kappa\bar{\varepsilon})\left|\frac{\bar{\varepsilon}}{\kappa}\right| \quad \text{and} \quad \xi^{\ominus} = -\frac{\sigma_Y}{E|\kappa|} + \text{Sign}(\kappa\bar{\varepsilon})\left|\frac{\bar{\varepsilon}}{\kappa}\right|. \tag{2.15}$$

Plastic flow in the beam is initiated as soon as the first fiber (i.e. either the top or the bottom fiber) has yielded. The non-linear stress state across the beam thickness is integrated to obtain closed-form expressions for the normal force and the moment as functions of the axial strain $\bar{\varepsilon}$ and the curvature κ:

$$\begin{aligned} M(\bar{\varepsilon}, \kappa) \quad = \quad & -b\left\{\int_{-\frac{t}{2}}^{\xi^{\ominus}} \frac{\varepsilon}{|\varepsilon|}\sigma_Y \left(1 + \frac{E}{\sigma_Y}|\varepsilon^p|\right)^N y \, dy \right. \\ & \left. + \int_{\xi^{\ominus}}^{\xi^{\oplus}} E\varepsilon y \, dy + \int_{\xi^{\oplus}}^{\frac{t}{2}} \frac{\varepsilon}{|\varepsilon|}\sigma_Y \left(1 + \frac{E}{\sigma_Y}|\varepsilon^p|\right)^N y \, dy\right\} \end{aligned} \tag{2.16}$$

and

$$\begin{aligned} P(\bar{\varepsilon}, \kappa) \quad = \quad & b\left\{\int_{-\frac{t}{2}}^{\xi^{\ominus}} \frac{\varepsilon}{|\varepsilon|}\sigma_Y \left(1 + \frac{E}{\sigma_Y}|\varepsilon^p|\right)^N dy \right. \\ & \left. + \int_{\xi^{\ominus}}^{\xi^{\oplus}} E\varepsilon \, dy + \int_{\xi^{\oplus}}^{\frac{t}{2}} \frac{\varepsilon}{|\varepsilon|}\sigma_Y \left(1 + \frac{E}{\sigma_Y}|\varepsilon^p|\right)^N dy\right\}. \end{aligned} \tag{2.17}$$

Evaluation of the above integrals is straightforward and the closed-form expressions are presented in Appendix A. As noted in the Appendix A, the relations for the linear strain hardening can be obtained as a special case by replacing E/σ_Y with H/σ_Y and $N = 1$. Using these expressions is computationally convenient and enables us to track the development of the elastic-plastic front across the beam thickness without the necessity of numerical integration using cross sectional fibers. Note that after the

initiation of yielding, plastic constraint effects at the elastic-plastic boundary may cause out-of-plane stresses to develop, violating the plane stress conditions locally in the plastic zones/hinges. We neglect this effect and assume no out-of-plane stresses to be present after yielding and proceed with two-dimensional beam theory for the struts.

2.2.3 Finite element implementation

In this section, we present an extensible Euler-Bernoulli beam formulation in an updated-Lagrange framework. In a structure consisting of many curved struts at different orientations, the strut axis is discretized into linear beam elements with appropriately defined local co-ordinate systems. Let the nodal displacement and force vectors in the local co-ordinate system be denoted by

$$\mathbf{p} = [\ u_1 \quad v_1 \quad \phi_1 l_r \quad u_2 \quad v_2 \quad \phi_2 l_r\ ]^T \tag{2.18a}$$

and

$$\mathbf{f} = [\ f_{x_1} \quad f_{y_1} \quad m_1/l_r \quad f_{x_2} \quad f_{y_2} \quad m_2/l_r\ ]^T, \tag{2.18b}$$

where u_i, v_i and ϕ_i are the local axial displacement, transverse displacement and rotation in the node i ($i = 1, 2$), respectively, and f_{x_i}, f_{y_i} and m_i are the associated nodal forces and moments (see Fig. 2.2); l_r is used to enforce that all entries of $\mathbf{p}$

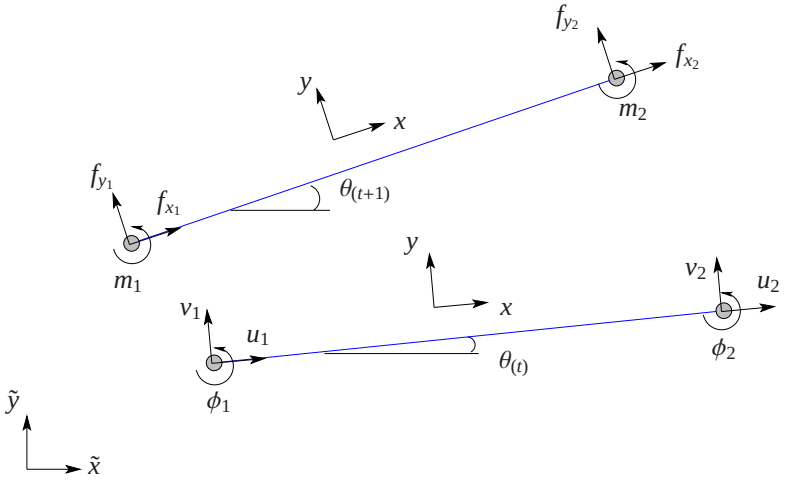

Figure 2.2: Beam element and the local and global co-ordinate systems.

and $\mathbf{f}$ have the same dimensions and it is taken to be the average strut length. The axial and transverse displacements of the neutral axis along the beam element are expressed in terms of the nodal quantities as

$$\{ \; u \quad v \; \}^T = [\; \mathbf{N}_u \quad \mathbf{N}_v \;]^T \mathbf{p} \tag{2.19}$$

where $\mathbf{N}_u$ and $\mathbf{N}_v$ are the vectors containing the standard shape functions of the EB beam element expressed in the isoparametric coordinate $\xi = 2X/L - 1$ and $\xi \in [-1, 1]$ (Wriggers, 2008). Here, L is the length of the beam element in the reference configuration. Now, for convenience, we introduce a shorthand notation for the characteristic strain measures and the stress resultants as

$$\boldsymbol{\epsilon} = \{\bar{\varepsilon}, \kappa\} \quad \text{and} \quad \boldsymbol{\sigma} = \{P, M\}, \tag{2.20}$$

respectively, so that the internal virtual work expression Eq. 2.3 can be written as

$$\delta W_i = \frac{L}{2} \int_\xi (\delta\boldsymbol{\epsilon})^T \boldsymbol{\sigma} \, d\xi. \tag{2.21}$$

Using the displacement interpolations from Eq. 2.19, the strain measure becomes

$$\boldsymbol{\epsilon} = \left\{ (\mathbf{b}_u + \frac{1}{2}\mathbf{p}^T \mathbf{b}_v^T \mathbf{b}_v)\mathbf{p}, \quad \mathbf{c}_v \mathbf{p} \right\} \tag{2.22a}$$

$$\text{and} \quad \delta\boldsymbol{\epsilon} = \left\{ (\mathbf{b}_u + \mathbf{p}^T \mathbf{b}_v^T \mathbf{b}_v)\delta\mathbf{p}, \quad \mathbf{c}_v \delta\mathbf{p} \right\}. \tag{2.22b}$$

where

$$\frac{du}{dX} = \frac{d\mathbf{N}_u}{dX}\mathbf{p} = \mathbf{b}_u\mathbf{p}, \quad \frac{dv}{dX} = \frac{d\mathbf{N}_v}{dX}\mathbf{p} = \mathbf{b}_v\mathbf{p} \quad \text{and} \quad \frac{d^2v}{dX^2} = \frac{d^2\mathbf{N}_v}{dX^2}\mathbf{p} = \mathbf{c}_v\mathbf{p}.$$

We assume the axial force P to be uniform over the element. Then it is useful to define an effective axial strain uniform over the element length (see the discussion in Section 7.1.3 in Crisfield (1991b)) according to

$$\bar{\epsilon}_1 = \frac{1}{L} \int_X \bar{\varepsilon} \, dX = \frac{1}{L} \int_\xi (\mathbf{b}_u + \frac{1}{2}\mathbf{p}^T \mathbf{b}_v^T \mathbf{b}_v)\mathbf{p} \frac{L}{2} \, d\xi \tag{2.23}$$

and its variation is

$$\delta\bar{\epsilon}_1 = \frac{1}{L} \int_X \delta\bar{\varepsilon} \, dX = \left[\frac{1}{L} \int_\xi (\mathbf{b}_u + \mathbf{p}^T \mathbf{b}_v^T \mathbf{b}_v) \frac{L}{2} \, d\xi \right] \delta\mathbf{p}. \tag{2.24}$$

For a beam in equilibrium (i.e. $f_{x_2} = -f_{x_1} = P$, $f_{y_1} = -f_{y_2} = V$ and $m_2 = -m_1 - f_{y_2} l =$

M_2), the internal moment M (defined clockwise positive) varies linearly along the length of the beam and can be written as

$$M = V\frac{L}{2}(\xi - 1) + M_2. \tag{2.25}$$

For small strains, we introduce the approximation that $L \approx l$, where l is the current length of the beam element. Substituting this and Eq. 2.22b in Eq. 2.21 yields

$$\begin{aligned} \delta W_i &= \delta\mathbf{p}^T \int_\xi \left((\mathbf{b}_u^T + \mathbf{b}_v^T \mathbf{b}_v \mathbf{p})P + \mathbf{c}_v^T M\right)\frac{L}{2} d\xi, \\ &= \begin{bmatrix} L\,\delta\bar{\epsilon}_1 \\ \delta v_1 - \delta v_2 + L\,\delta\phi_1 \\ (\delta\phi_2 - \delta\phi_1)L \end{bmatrix}^T \begin{Bmatrix} f_{x_2} \\ f_{y_1} \\ m_2/L \end{Bmatrix}, \\ &= \delta\mathbf{e}^T\mathbf{s}. \end{aligned} \tag{2.26}$$

One can now choose

$$\mathbf{s} = \begin{bmatrix} f_{x_2} & f_{y_1} & m_2/L \end{bmatrix}^T, \tag{2.27}$$

as the generalized stresses and the corresponding work conjugates

$$\mathbf{e} = \begin{bmatrix} L\,\bar{\epsilon}_1 & (v_1 - v_2 + \phi_1 L) & (\phi_2 - \phi_1)\,L \end{bmatrix}^T, \tag{2.28}$$

as the generalized strains. It should be noted that the generalized strain vector $\mathbf{e}$ is non-linear in $\mathbf{p}$ due to e_1 and its variation due to the variation in $\mathbf{p}$ is

$$\delta\mathbf{e} = \frac{\partial\mathbf{e}}{\partial\mathbf{p}}\delta\mathbf{p} = \mathbf{D}(\mathbf{p})\delta\mathbf{p}, \tag{2.29}$$

where

$$\mathrm{D}_{ij} = \frac{\partial e_i}{\partial p_j} = \begin{bmatrix} -1 & 0 & 0 \\ \dfrac{6(v_1 - v_2)}{5\,L} + \dfrac{(\phi_1 + \phi_2)}{10} & 1 & 0 \\ \dfrac{(v_1 - v_2)}{10\,l_r} + \dfrac{L\,(4\phi_1 - \phi_2)}{30\,l_r} & \dfrac{L}{l_r} & -\dfrac{L}{l_r} \\ 1 & 0 & 0 \\ \dfrac{6(v_2 - v_1)}{5L} - \dfrac{(\phi_1 + \phi_2)}{10} & -1 & 0 \\ \dfrac{(v_1 - v_2)}{10\,l_r} - \dfrac{L\,(\phi_1 + 4\phi_2)}{30\,l_r} & 0 & \dfrac{L}{l_r} \end{bmatrix}^T. \tag{2.30}$$

Next we derive the relation between the generalized stresses and generalized

strains. For numerical convenience, we incorporate plastic deformation through a viscoplastic relation between strain rates and stresses. We assume an additive decomposition of the elastic and viscoplastic strain rates:

$$\dot{\mathbf{e}} = \dot{\mathbf{e}}^{el} + \dot{\mathbf{e}}^{vp}. \tag{2.31}$$

The elastic constitutive relations for the EB beam are given by

$$P = EA\bar{\epsilon}_1, \quad M = EI\frac{d^2v}{dX^2} \quad \text{and} \quad V = EI\frac{d^3v}{dX^3}. \tag{2.32}$$

Substituting Eq. 2.19 in the constitutive relations, one readily obtains the generalized stress-generalized strain relation in rate form as

$$\dot{\mathbf{s}} = \mathbf{S}\dot{\mathbf{e}}^{el}, \tag{2.33}$$

with

$$\mathbf{S} = \begin{bmatrix} \frac{EA}{L} & 0 & 0 \\ 0 & \frac{12EI}{L^3} & \frac{6EI}{L^3} \\ 0 & \frac{6EI}{L^3} & \frac{4EI}{L^3} \end{bmatrix}. \tag{2.34}$$

The viscoplastic strain rate of a beam under uniaxial tension can be written as a power law dependence on the force P according to

$$\dot{\bar{\varepsilon}}^{vp} = \dot{\bar{\varepsilon}}_0 \left(\frac{P}{P_0}\right)^n, \tag{2.35}$$

where $\dot{\bar{\varepsilon}}_0$ and n are the viscoplastic material parameters, $P_0 = \sigma_0 A$, σ_0 is the reference stress and A is the cross sectional area. By adopting this power law relation (Eq. 2.35) and setting the exponent $n \to \infty$, rate-independent plasticity can be recovered with $\sigma_0 = \sigma_Y$. In this limit, the material parameters ($\dot{\bar{\varepsilon}}_0$ and n) loose their physical significance and become parameters of the numerical method.

For perfect plasticity, the viscoplastic curvature rate can be expressed in a similar form as Eq. 2.35:

$$\dot{\kappa}^{vp} = \dot{\kappa}_0 \left(\frac{M}{M_0}\right)^n, \tag{2.36}$$

where M is the bending moment and $M_0 = (1/4)bt^2\sigma_Y$ is the fully plastic moment (Mangipudi and Onck, 2006). Taking Eqs. 2.35 and 2.36 with a large n ensures that the normal force P and moment M in the beam follow the reference force (P_0)

and reference moment (M_0) when the material is inelastically strained. To incorporate strain hardening, the form of these two equations is preserved and the reference quantities P_0 and M_0 are taken to be dependent on the accumulated strain ($\boldsymbol{\epsilon} = \{\bar{\varepsilon}, \kappa\}$) through the constitutive laws derived in the sections 2.2.1 and 2.2.2.

To obtain the generalized viscoplastic strain rates as a function of the generalized stresses, we integrate Eq. 2.35 and 2.36 along the beam length, giving the following closed form expressions

$$\begin{aligned} \dot{e}_1^{vp} &= g_1(s_1, l, \bar{\varepsilon}_0, P_0, n), \\ \dot{e}_2^{vp} &= g_2(s_2, s_3, l, \dot{\kappa}_0, M_0, n), \\ \dot{e}_3^{vp} &= g_3(s_3, s_3, l, \dot{\kappa}_0, M_0, n). \end{aligned} \tag{2.37}$$

Details of the derivation and the resulting expressions for g_1, g_2 and g_3 are given in Appendix B.

The final system of equations for one element now follows from the rate form of the principle of virtual work

$$\begin{aligned} \overline{\delta \mathbf{e}^T \mathbf{s}} &= \overline{\delta \mathbf{p}^T \mathbf{f}}_{\text{ext}}, \\ \delta \mathbf{p}^T s_1 \frac{\partial \mathbf{D}_1^T}{\partial \mathbf{p}} \dot{\mathbf{p}} + \delta \mathbf{p}^T \mathbf{D}^T \dot{\mathbf{s}} &= \delta \mathbf{p}^T \dot{\mathbf{f}}_{\text{ext}} \end{aligned} \tag{2.38}$$

where $\mathbf{f}_{ext}$ is the external load vector. By substituting Eq. 2.33 and $\dot{\mathbf{e}} = \mathbf{D}\dot{\mathbf{p}}$ in the above equation, we obtain

$$(\mathbf{k}_{\text{M}} + \mathbf{k}_{\text{G}})\dot{\mathbf{p}} = \dot{\mathbf{f}}_{\text{ext}} + \dot{\mathbf{f}}^{vp} \tag{2.39}$$

with $\mathbf{k}_{\text{M}} = \mathbf{D}^T \mathbf{S} \mathbf{D}$, $\mathbf{k}_{\text{G}} = s_1(\partial \mathbf{D}_1^T / \partial \mathbf{p})$ and $\dot{\mathbf{f}}^{vp} = \mathbf{D}^T \mathbf{S} \dot{\mathbf{e}}^{vp}(\mathbf{s})$. Here, $\mathbf{D}_1$ is the first row of the matrix $\mathbf{D}$, while $\mathbf{k}_{\text{M}}$ and $\mathbf{k}_{\text{G}}$ are the element material and geometric stiffness matrices, respectively. It should be noted that the second and third rows in $\mathbf{D}$ are independent of $\mathbf{p}$ (refer to Eq. 2.30) and thus their variation w.r.t. $\mathbf{p}$ is zero. The only non-zero contribution to $\mathbf{k}_{\text{G}}$ is from the variation in the first row of $\mathbf{D}$. We adopt an updated Lagrange scheme with explicit time integration so that at the beginning of every step $\mathbf{p} = \mathbf{0}$ and the strain-displacement matrix $\mathbf{D}$ becomes independent of $\mathbf{p}$. To speed up the solution procedure, we use a forward gradient method for the time integration of the viscoplastic strain rates. The transformation of the vectors and matrices to the global co-ordinate system following the standard transformation and assembly rules gives the final global finite element equation.

This model will be used in chapter 3 to study stain hardening.

2.2.4 Extension to include damage

Incorporation of a softening relation for the reference stress resultants (P_0 and M_0) based on an appropriate failure criterion appears to be straight-forward. Attempts have been made to define softening laws for the reference normal force and moments coupled through a damage variable. The damage variable can be defined based on the sum of dissipated stretching and bending energies during failure, in a similar fashion as the damage variable of Schmidt et al. (2003). However, despite of the choice of various forms of the softening relations, this damage formulation within the above viscoplastic framework produced unphysical excessive axial elongation in the damaging element. The reason for this unexpected behaviour is speculated to be a violation of the normality condition during loading in damage (but not for plastic deformation) due to an uncoupled variation in the generalized fracture strains (c.f. Eqs. 2.35 and 2.36 with softening relation for P_0 and M_0). A solution would be to formulate damage using a Perzyna-type viscoplastic formulation using a yield/fracture surface in the stress resultant space. However, we also note that the above small strain shallow arch beam formulation poses difficulties to equilibrate the structure when some struts are removed after an arbitrarily chosen damage threshold (say greater than 95%). In this respect, a large deformation formulation with consistent tangent is necessary. We chose a co-rotational beam element formulation for this purpose. A Perzyna-type viscoplastic framework including damage is presented in Appendix C. During damage, even with a forward gradient approximation for the viscoplastic strain, this formulation required stringent time step control to meet convergence for all the model parameters, making it computationally prohibitive. On the other hand, a layered beam approach, as presented in the following section, proved to be comparatively fast. Hence, we will use the layered beam model to account for damage in this thesis.

2.3 Elasto-plastic-damage model using effective beam stiffness

2.3.1 Discrete model of a two-dimensional open-cell foam

Our micromechanical model of a two-dimensional open-cell foam is based on a Voronoi representation of the cellular architecture (see Fig. 2.3(a)). The edges of the Voronoi represent the struts as shown in Fig. 2.3(b). During macroscopic loading, each strut cross section Q experiences stretching and bending strain increments, $\Delta\bar{\varepsilon}$ and $\Delta\kappa$, respectively. From these axial strain and curvature increments, the strain increment at any material point is given by $\Delta\varepsilon(y) = \Delta\bar{\varepsilon} - y\,\Delta\kappa$ which, integrated in time, deter-

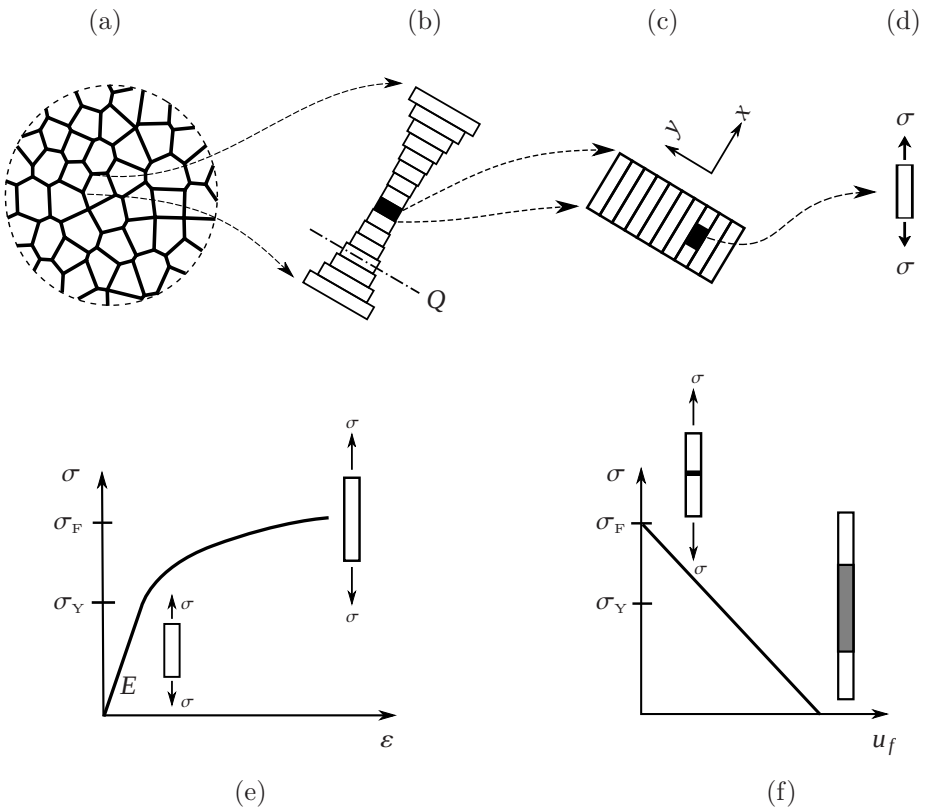

Figure 2.3: Multiscale model: (a) Voronoi description of the two-dimensional cellular solid, (b) an arbitrarily oriented strut discretized into beam elements of different thickness, (c) a beam element with fibers in its local co-ordinate system, (d) an element of the fiber under simple tension. Deformation and failure of the fiber element due to an elastic-power law hardening stress-strain relation followed by a traction-separation relation during softening, shown in (e) and (f), respectively.

mines the cross sectional strain state, see Fig. 2.4(a). At every material point within the strut, material constitutive laws for the elasto-plastic deformation and damage are incorporated. Based on the deformation state (elastic, plastic or damaging) and the stress $\sigma(y)$ at the material point, the tangent modulus E_t is obtained from the material constitutive laws. Once the strain increments are known, the stress state across the thickness $\sigma(y)$ can be updated from $\Delta\sigma(y) = E_t\,\Delta\varepsilon(y)$ (see Fig. 2.4(b)). The axial force P and the bending moment M per unit out-of-plane thickness are given

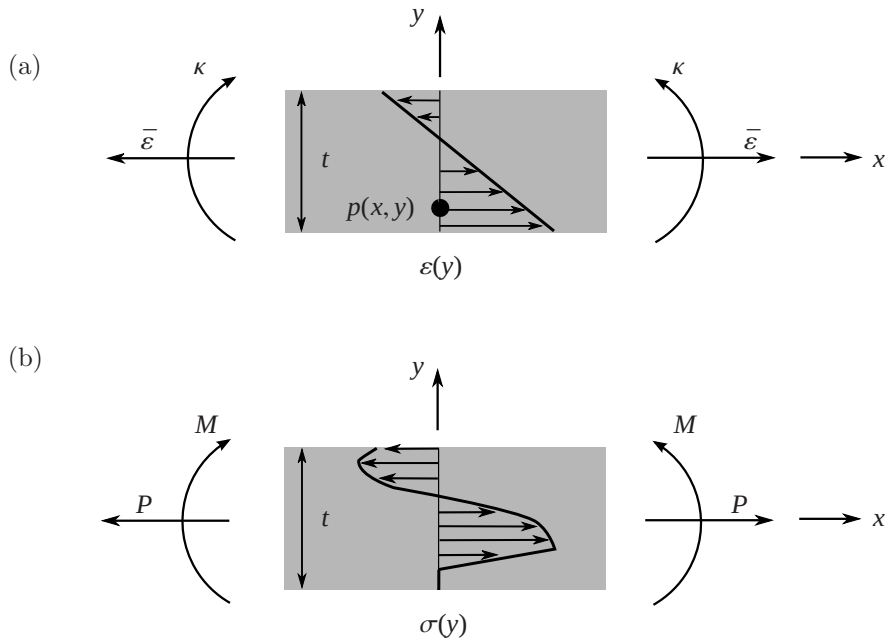

Figure 2.4: (a) Strain and (b) stress profiles across the cross section Q in Fig. 2.3(b).

by

$$P = \int_y \sigma(y)\, dy \quad \text{and} \quad M = -\int_y y\, \sigma(y)\, dy. \tag{2.40}$$

Thus, the general beam constitutive laws, relating the incremental element strains $\{\Delta\bar{\varepsilon}, \Delta\kappa\}$ and the stress resultants $\{\Delta P, \Delta M\}$ can be written as

$$\begin{pmatrix} \Delta P \\ \Delta M \end{pmatrix} = \begin{bmatrix} \widehat{EA} & -\widehat{EX} \\ -\widehat{EX} & \widehat{EI} \end{bmatrix} \begin{pmatrix} \Delta\bar{\varepsilon} \\ \Delta\kappa \end{pmatrix}, \tag{2.41}$$

with

$$\widehat{EA} = \int_y E_t(y)\, dy, \quad \widehat{EX} = \int_y y\, E_t(y)\, dy \quad \text{and} \quad \widehat{EI} = \int_y y^2\, E_t(y)\, dy. \tag{2.42}$$

Note that since the stress state changes from one cross section to another, the stiffness also changes along the length of the strut.

In the finite element implementation, the struts are discretized using two-noded Euler-Bernoulli beam elements (Fig. 2.3(b)). Each beam element is represented by a finite number of "fibers" across the thickness as shown in Fig. 2.3(c) and each fiber

is in a state of uniaxial tension (Fig. 2.3(d)). Up to the critical fracture stress, the material along a fiber deforms according to the elasto-plastic stress-strain law (see Fig. 2.3(e)). We assume a power-law hardening given by

$$\sigma = \sigma_{\mathrm{Y}} \left(1 + \frac{E}{\sigma_{\mathrm{Y}}} \varepsilon^{p}\right)^{N}, \tag{2.43}$$

where σ_{Y}, ε^{p} and N are the material yield stress, the plastic strain and the hardening exponent, respectively. When the critical fracture stress σ_{F} is reached, deformation concentrates in a zone where damage forms, leading to a relation between stress and displacement (Fig. 2.3(f)). A linear stress-displacement (or traction-separation) relationship is defined according to

$$\sigma = \sigma_{\mathrm{F}} \left(1 - u_f \frac{\sigma_{\mathrm{F}}}{2\Gamma_0}\right), \tag{2.44}$$

which ensures that always a fixed amount of fracture energy per unit area of the cross section of the beam, Γ_0, is dissipated.

Given the stress state of a fiber at y, the tangent modulus $E(y)$ is given by

$$E_t(y) = \begin{cases} E & \text{if } |\sigma(y)| < \sigma_{\mathrm{Y}}, \\ \left(\dfrac{d\sigma}{d\varepsilon}\right)_{\varepsilon(y)} & \text{if } \sigma_{\mathrm{Y}} \le |\sigma(y)| < \sigma_{\mathrm{F}}, \\ -\dfrac{\sigma_{\mathrm{F}}^2}{2\Gamma_0} l_c & \text{during damage,} \end{cases} \tag{2.45}$$

in which an instantaneous softening modulus containing the current element length l_c is defined for convenience in accordance with the stress-displacement law. With the help of Eq. (2.45), the stiffness matrix in Eqs.(2.42) and (2.41) will be evaluated at the mid point along the element length. The details of the finite element implementation are presented below.

2.3.2 Finite element framework

We will use the co-rotational elastic beam formulation as presented by Crisfield (1991b) and incorporate inelastic deformation through fibers. The kinematics of the co-rotational beam element in two-dimensions is shown in Fig. 2.5. A local co-ordinate system $x - y$ is attached with the element and rotates with respect to the global co-ordinate system $\tilde{x} - \tilde{y}$. Let the global nodal displacement and force vectors

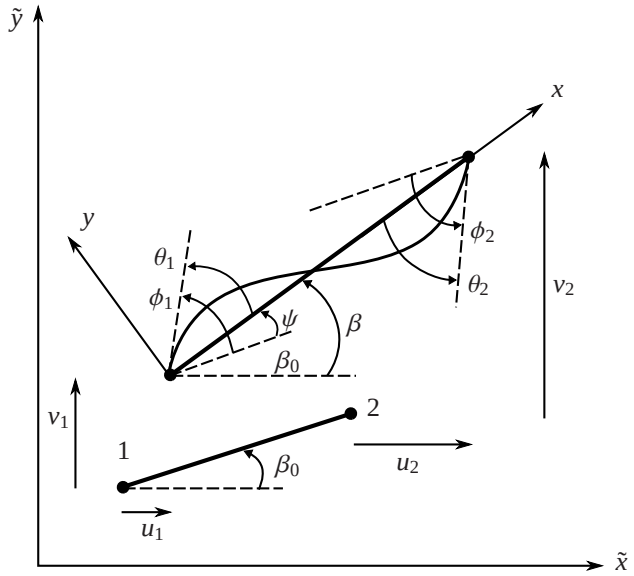

Figure 2.5: Kinematics of the co-rotational beam element in two-dimensions.

be denoted by

$$\mathbf{p} = \begin{bmatrix} u_1 & v_1 & \phi_1 & u_2 & v_2 & \phi_2 \end{bmatrix} \quad \text{and} \quad \mathbf{f} = \begin{bmatrix} f_{x_1} & f_{y_1} & m_1 & f_{x_2} & f_{y_2} & m_2 \end{bmatrix}, \tag{2.46}$$

where u_i, v_i and $\phi_i\,(i = 1, 2)$ are the axial and transverse displacements and rotations in node i, while f_{x_i}, f_{y_i} and m_i are the corresponding nodal forces and moments. If u and v are the axial and transverse displacements of the beam axis respectively, the Green-Lagrange strain relative to the co-rotating system can be written as

$$\begin{aligned} \varepsilon &= \frac{du}{dX} + \frac{1}{2}\left(\frac{du}{dX}\right)^2 + \frac{1}{2}\left(\frac{dv}{dX}\right)^2 - y\frac{d^2v}{dX^2}, \\ &= \bar{\varepsilon} - y\kappa. \end{aligned} \tag{2.47}$$

To avoid membrane locking, the axial strain $\bar{\varepsilon}$ will be replaced by an average axial strain measure $\bar{\varepsilon}_{\text{av}}$, which is uniform over the beam length and is defined according to

$$\bar{\varepsilon}_{\text{av}} = \frac{1}{l_0}\int_0^{l_0} \bar{\varepsilon}\, dX, \tag{2.48}$$

where l_0 is the beam element length in the reference configuration X with orientation β_0.

For the co-rotational element, the local rotation θ is defined as $\theta = \phi - \psi$, where $\psi = \beta - \beta_0$ is the rigid body rotation and β and β_0 are the current and reference orientations of the co-rotating frame respectively. By choosing the local axial displacement $l_0\bar{\varepsilon}_{\text{av}}$ and the local nodal rotations θ_1 and θ_2 as the generalized strains $\mathbf{e}$, the strain-displacement relation can be written as

$$\delta\mathbf{e} = \mathbf{B}\delta\mathbf{p}, \tag{2.49}$$

where the strain-displacement matrix $\mathbf{B}$ is given in Crisfield (1991b).

For a rectangular prismatic beam of unit out-of-plane thickness, the internal virtual work can be written as

$$\delta W_{\text{int}} = \int_{\bar{V}} \delta\varepsilon\, \sigma\, d\bar{V} = \int_X (\delta\bar{\varepsilon}_{\text{av}}\, P + \delta\kappa\, M)\, dX, \tag{2.50}$$

where $\bar{V}$ refers to the reference configuration and the axial force P and the bending moment M are given by Eq. (2.40).

By noting that the moment varies linearly along the beam length and by using standard interpolation functions for the axial and transverse displacements, it follows that the internal virtual work in the local co-ordinate system can be written as

$$\delta W_{\text{int}} = \begin{bmatrix} l_0\delta\varepsilon_{\text{av}} & \delta\theta_1 & \delta\theta_2 \end{bmatrix} \begin{bmatrix} P \\ M_1 \\ M_2 \end{bmatrix} = \delta\mathbf{e}^T\mathbf{s}, \tag{2.51}$$

where $\mathbf{s}$ is the generalized stress vector. Here, the superscript $(\cdot)^T$ denotes vector or matrix transpose. The internal virtual work can also be written in the global co-ordinate system as

$$\delta W_{\text{int}} = \delta\mathbf{p}^T\mathbf{f}_{\text{int}}, \tag{2.52}$$

where $\mathbf{f}_{\text{int}}$ is the global internal force vector. If the external virtual work is $\delta W_{ext} = \delta\mathbf{p}\,\mathbf{f}_{\text{ext}}$, then by equating the external and internal virtual work and from Eqs. (2.51), (2.52) and (2.49), one obtains

$$\mathbf{f}_{\text{ext}} = \mathbf{B}^T\mathbf{s}. \tag{2.53}$$

The above equation can be solved using Newton-like iterative methods where the residual is given by

$$\mathbf{R(p)} = \mathbf{B}^T\mathbf{s} - \mathbf{f}_{\text{ext}}. \tag{2.54}$$

The stiffness matrix during the iterations is given according to

$$\frac{\partial R_i}{\partial p_j} = B_{ik} C_{kl} B_{lj} + \frac{\partial B_{ik}}{\partial p_j} s_k. \tag{2.55}$$

$$= K_{ij}^M + K_{ij}^G, \tag{2.56}$$

where $\mathbf{K}^M$ and $\mathbf{K}^G$ are the material and geometric stiffness matrices, respectively. Here, we have used the incremental generalized stress-generalized strain relationship defined according to

$$\Delta \mathbf{s} = \mathbf{C}\,\Delta \mathbf{e} = \mathbf{C}\,\mathbf{B}\,\Delta \mathbf{p} \quad \text{with} \quad C_{ij} = \frac{\partial s_i}{\partial e_j}. \tag{2.57}$$

The element stiffness matrix in Eq. (2.56) is already defined in the global reference frame and can thus be straightforwardly assembled in the systems stiffness matrix. The tangent matrix $\mathbf{C}$ can be obtained by through-thickness integration which will be presented below.

The curvature increment is interpolated as

$$\Delta\kappa = \frac{d^2 \Delta v}{dX^2} = \frac{2}{l_0} \begin{bmatrix} 3\xi - 2 & 3\xi - 1 \end{bmatrix} \begin{bmatrix} \Delta\theta_1 \\ \Delta\theta_2 \end{bmatrix}, \tag{2.58}$$

with $\xi = X/l_0\, \xi \in [0, 1]$. For a general material constitutive behaviour given by $\Delta\sigma = E_t\, \Delta\varepsilon$, with E_t being the tangent modulus, the change in the axial force in Eq. (2.40) will become

$$\Delta P = \int_y E_t\, (\Delta\bar{\varepsilon}_{\text{av}} - y\, \Delta\kappa)\, dy = \widehat{EA}\, \Delta\bar{\varepsilon}_{\text{av}} - \widehat{EX}\, \frac{1}{l_0} (\Delta\theta_2 - \Delta\theta_1), \tag{2.59}$$

where we have used midpoint Gauss integration for the curvature term. Similarly, the change in the moment is

$$\Delta M = -\int_y E_t\, \Delta\varepsilon\, y\, dy = -\widehat{EX}\, \Delta\bar{\varepsilon}_{\text{av}} + \widehat{EI}\, \Delta\kappa.$$

The moment varies linearly with the beam length according to

$$\Delta M = \Delta M_1 (\xi - 1) + \xi \Delta M_2. \tag{2.60}$$

Using the curvature interpolation from Eq. (2.58) and by setting $\xi = 0$ and $\xi = 1$, we get

$$\Delta M_1 = \widehat{EX}\, \Delta\bar{\varepsilon}_{\text{av}} + \frac{1}{l_0}\, \widehat{EI}\, (4\, \Delta\theta_1 + 2\, \Delta\theta_2) \tag{2.61}$$

and

$$\Delta M_2 = -\widehat{EX}\,\Delta\bar{\varepsilon}_{\text{av}} + \frac{1}{l_0}\widehat{EI}\,(2\,\Delta\theta_1 + 4\,\Delta\theta_2) \tag{2.62}$$

respectively. Hence, the symmetric tangent stiffness matrix $\mathbf{C}$ is obtained in terms of the midpoint integrals:

$$\mathbf{C} = \frac{1}{l_0}\begin{bmatrix} \widehat{EA} & \widehat{EX} & -\widehat{EX} \\ \cdot & 4\widehat{EI} & 2\widehat{EI} \\ \cdot & \cdot & 4\widehat{EI} \end{bmatrix}. \tag{2.63}$$

For linear elastic materials, $E_t = E$, $\widehat{EA} = EA$, $\widehat{EX} = EI_1$ and $\widehat{EI} = EI_2$, where E is the Young's modulus, $A = bt$ is the area of the cross section (b is the out-of-plane thickness), I_1 and I_2 are the first and second moments of the area, respectively. For a symmetric beam cross section with linear elastic material, $\widehat{EX}$ vanishes provided the beam axis coincides with the centroidal axis. For any other choice of the reference plane, neglecting the cross-coupling term $\widehat{EX}$ can lead to significant errors (Crisfield, 1991a). In the present formulation, it is assumed that the reference plane passes through the centroidal line. However, eccentricity will be introduced into the problem due to the fact that the tangent modulus E_t can be non-symmetric with respect to the mid-plane and hence, the cross-coupling term cannot be neglected.

To evaluate the integrals in Eq. (2.42), numerical integration is generally adopted when material nonlinearity is present. Among various integration schemes, the Gauss quadrature and the Labatto methods are shown to yield the best results (Burgoyne and Crisfield, 1990). Since we will be dealing with damage and unloading of the layers, a centroidal rule offers the advantage of fixing the integration points and therefore avoids the required fiber remeshing upon failure and the associated interpolation of the fiber stresses to the newly remeshed integration points upon fiber failure. When more than 13 integration points are used, the centroidal rule and the Gauss quadrature were found to yield similar results and hence the centroidal technique will be adopted. In the centroidal technique, the thickness of the beam is divided into a number of integrations points (or fibers) of equal thickness Δy. The property is assumed to be constant over each region and is lumped at the centroid of each fiber. With an equal weight to each fiber, the numerical integration of Eq. (2.42) becomes a weighted summation of the lumped integrands:

$$\widehat{EA} = \sum_{i=1}^{n_f} E_t(y_i)\Delta y, \quad \widehat{EX} = \sum_{i=1}^{n_f} E_t(y_i)\, y_i \Delta y \quad \text{and} \quad \widehat{EI} = \sum_{i=1}^{n_f} E_t(y_i)\, y_i^2 \Delta y. \tag{2.64}$$

where $i = 1, 2, .., n_f$ and n_f is the total number of fibers. The tangent modulus E_t is given by Eq. (2.45) based on the stress state at the element midpoint. Unloading

and reloading of fibers stresses at any stage is accounted for using a set of history variables per fiber.

2.3.3 Solution scheme

Equation 2.44 ensures that the damage formulation in itself is mesh independent. However, when damage occurs under mixed loading or pure bending, problems of mesh dependency arise due to the coexisting stress-strain and stress-displacement formulations for the plastic and damaging fibers, respectively. This coupled situation does not occur in pure tension as all the fibers fail at the same time. In order to overcome this problem, fiber failure is allowed under compression as well. As a result, the stress-displacement relation dominates the element softening rate ensuring a mesh independent response. During the damage development, both the work of plastic deformation and the work of fracture contribute to the toughness of the strut. Elastic unloading and reloading of the fibers is accounted for during elasticity, plasticity and damage. Eq. 2.44 indicates that the tangent stiffness of a damaging fiber is negative. Consequently, the effective stiffness of a damaging strut can also become negative, resulting in an indefinite global stiffness matrix. We have used either the direct solver (DSS) from Intel MKL (2007) or the MA57 solver from Harwel Subroutine Library (2007). An updated Lagrange scheme has been used. We use an explicit solution procedure with an equilibrium correction based on the residuals of the previous step to avoid drifting off the equilibrium path and an automatic time-stepping control is implemented. When damage initiates in neighboring elements in a strut, a competition of unloading occurs, resulting in cross-talk of elastic unloading and softening, which can lead to computational instabilities. To overcome these instabilities, three equal-sized regions are identified along the strut length. Inside these regions, failure at multiple locations is not allowed. This choice is found to not affect the single strut response. When a damaging element has dissipated more than 85% of the total fracture energy $\Gamma_0 A$, the element is set for removal. A completely failed element will leave two stress-free parts of the strut still being connected to the strut junctions. To reduce the computational costs, the entire strut will be removed. During the strut removal procedure, the macroscopic loading is stopped. Then we replace the strut with equivalent forces and moments and step down these forces and moments to zero, after which the macroscopic loading is resumed.

The above defined model will be used to account for damage in chapters 4, 5 and 6.

2.4 Representation of the cellular architecture

Metal foams in general exhibit a random cell structure. Perfect hexagonal structures serve as idealised structures to look at the microscopic deformation mechanisms. However, the mesoscopic mechanisms of deformation and fracture differ considerably from the real foams. Due to the symmetry, failure (either yielding or damage) in these perfect structures will happen simultaneously at all the triple points. Another difference is in the multiaxial behaviour (which will not be studied in this thesis). Under an equi-biaxial stress-state, the bending moments in the struts vanish, leaving stretching as the deformation mode. In real foams due to the random structure and imperfections, bending is still the dominant deformation mode in equi-biaxial loading and random bending-dominated failure takes place for any type of loading.

To account for the mesoscopic structure of real foams, mainly two types of randomness measures can be found in the literature. In two-dimensional analyses, perturbed hexagonal structures were used to represent random structures, where the maximum perturbation distance serves as a measure of randomness. In another approach, Voronoi tessellations have been used. Randomness in the Voronoi structures has been controlled by a minimum allowable distance between any two Voronoi nuclei.

In this thesis Voronoi structures will be used to represent the microstructure of random foams. The geometrical characteristics of Voronoi tessellations closely represent the kinetics of the foaming process. The Voronoi tessellation technique assumes that (i) all nuclei appear simultaneously, (ii) all nuclei remain fixed in position during the entire growth process, (iii) the rate of growth is linear and the same for all nuclei and in every direction, and (iv) the growth of a cell ceases at points on its surface where contact is made with a neighbouring cell. However, in practice the physics of foaming is much more complicated, so that several of the above assumptions are violated resulting in a different structure. For example, assuming a fixed location of the nuclei may not be realistic during foaming in either the liquid or solid state. Gravity-driven drainage of the liquid from the cell faces before solidification in closed cell foams leads to cell coalescence and missing cell walls. Curved cell walls in real foams is another example where the Voronoi assumptions have been violated. Despite of these shortcomings, the experimental topological analysis of real foam structures is in good agreement with the Voronoi structures (Gibson and Ashby, 1997) and hence we proceed with describing the structure of the open-cell foam using Voronoi tessellations. We do not include imperfections like missing cells walls, filled faces or cells, cell wall wavyness and cell wall misalignments. The role of these imperfections on the elastic and yield behaviour of foams can be found elsewhere (Silva and Gibson, 1997a; Grenestedt, 1998; Chen et al., 1999, 2001b).

Given a set of nuclei, the Voronoi diagram is the dual graph of the Delaunay

triangulation of the nuclei and is unique for the set of nuclei. For a completely random distribution of the nuclei, the Voronoi diagram features a wide range of cell sizes and is known as a Γ-Voronoi. The cell size distribution can be controlled to match the narrow size range observed in many commercial open-cell foams by appropriately choosing the initial nuclei. The random nuclei are generated such that a constraint is imposed through a minimum allowable distance s between any two nuclei. In a two-dimensional space of area A and for a given number of nuclei n, the minimum allowable distance s determines the type of packing. For a close-packed distribution of n nuclei producing a hexagonal structure, the distance r between any two adjacent nuclei is given by (Tekoğlu, 2007)

$$r = \sqrt{\frac{2A}{\sqrt{3}n}}. \tag{2.65}$$

A randomness parameter can be defined as $\delta = s/r$, $\delta \in [0, 1]$ such that $\delta = 0$ corresponds to a fully random Γ-Voronoi and $\delta = 1$ corresponds to a perfect regular hexagonal structure (Zhu et al., 2001a,b). Fig. 2.6 shows structures for three randomness values. In practice, to generate the nuclei distribution for a given s, a pseudo-random number generator is initialized with a random number seed and we begin by placing the first random nucleus within the area A. Any subsequent random nucleus generated in the sequence of the pseudo-random number generator will be allowed only if it meets the minimum allowable distance criterion; otherwise it is discarded and the next random number in the series is considered. This process is repeated until either n number of nuclei have been generated or a fairly large number (100000) of consecutive dismissals of random numbers occurs. It is worth noting here that the number of dismissals strongly increases when δ gets close to 1. In this thesis,

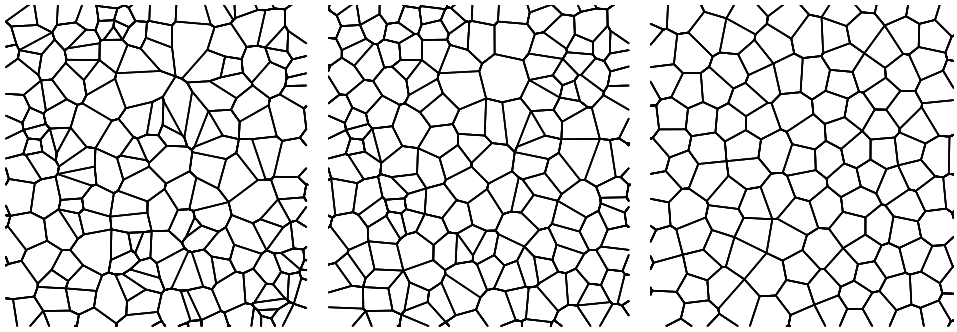

Figure 2.6: Typical Voronoi structures of increasing regularity for $\delta = 0$, 0.4 and 0.9, from left to right, respectively.

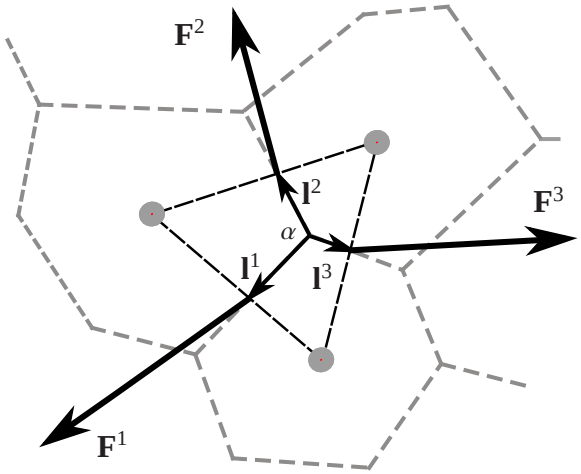

Figure 2.7: The portion of a Voronoi cell that is under the equilibrium of a system of forces $\mathbf{F}^n$ at nodes $n = 1, 2$, and 3, which will also keep the triangle (dark dashed line) in equilibrium. The vector $\mathbf{l}^n$ is the arm of action of the force $\mathbf{F}^n$ about α.

we use the built-in functions from the commercial software MATLAB® to generate the Voronoi structures.

2.5 Continuum representation of stress and strain fields in Voronoi structures

2.5.1 Stress mapping

Voronoi structures are created from a given set of nucleation points such that the edges of a two-dimensional Voronoi are perpendicular bisectors of the lines joining the nucleation points. When a Delaunay triangulation of the nucleation points is carried out, each triangle encompasses one or more Voronoi cell nodes and every side of the triangle is intersected by one or more Voronoi edges as shown in Fig. 2.7.

Let the foam structure be subjected to an arbitrary loading and the structure is in equilibrium. The free body diagram of a part of the Voronoi structure enclosed by triangle α is shown in Fig. 2.7. If we assume that the strut section forces are acting on the sides of the triangle, the triangle will also be under equilibrium of this system of forces. For such a system, a mean Cauchy stress $\boldsymbol{\sigma}^\alpha$, assumed to be uniform over the triangle enclosing α, can be calculated as (Ostoja-Starzewski, 1987; Landau and

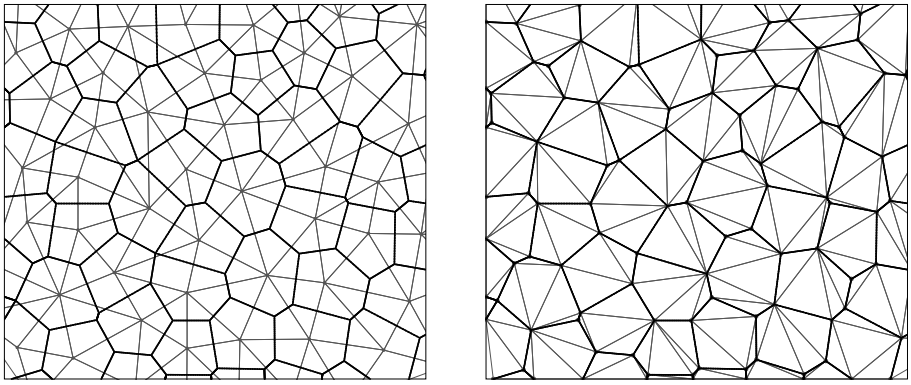

(a) (b)

Figure 2.8: Triangular meshes used in (a) stress mapping and (b) strain mapping procedures, plotted on top of the Voronoi structure (only a part of the structure is shown). Note that the triangular mesh in (a) is the dual structure of the Voronoi tessellation, which differs from the triangular mesh in (b) generated from the Voronoi vertices themselves.

Lifshitz, 1959)

$$\sigma_{ij}^{\alpha} = \frac{1}{2V^{\alpha}} \sum_{n=1}^{N^{\alpha}} (F_i^n l_j^n + F_j^n l_i^n), \tag{2.66}$$

where V^{α} is the volume of the triangle enclosing α, $\mathbf{F}^n$ is the force at the n^{th} section ($N^{\alpha} = 3$ in Fig. 2.7 and $\mathbf{l}^n$ is the arm of action of $\mathbf{F}^n$ about the centroid of the triangle enclosing α. Following the above procedure, the mean stress for every Delaunay triangle of the nucleation point distribution is obtained and a correlated stress map of the Voronoi structure is constructed at every time step.

The triangular mesh generated from the initial distribution of the nucleation points (see Fig. 2.8(a)) is used throughout the deformation history and does not deform with the Voronoi structure. Since the triangular mesh is fixed, with deformation the sides of the triangles may intersect different beam element. Also the centroid and the Voronoi vertex will be different which were initially the same. At large deformations it is also observed that a different set of struts may be enclosed by a given triangle. However, as long as the triangle is intersected by the struts, this method will be able to generate the stress map. The method in its present form will cease to work when a triangle is completely enclosed by one Voronoi cell. It should be noted that at the boundary, where the displacements are prescribed, transferring the reaction forces properly to the triangles near these boundaries is algorithmically involved.

Hence, these triangles are assigned zero mean stress in the present implementation leading to an erroneous representation of the stress field near these boundaries. When the height of the sample is large and when the mechanisms of interest are away from the boundary layer, this error can be neglected.

2.5.2 Strain mapping

Surface strain mapping techniques have been very useful in experiments to study the deformation mechanisms in closed-cell foams (McCullough et al., 1999b; Bart-Smith et al., 1998; Bastawros et al., 2000; Antoniou et al., 2004). This technique relies on correlating two successive digital images of the deforming material. A similar technique has been developed and applied in the finite element studies on two-dimensional Voronoi foams by Onck (2001b); Tekoğlu and Onck (2008), where the displacements of the triple points are utilized in mapping the strain field. In this thesis, we will adopt a modified version of the technique of Tekoğlu and Onck (2008)[1] to study the strain fields in single Voronoi structures (Van Buuren, 2007). In the following, the details of the strain mapping algorithm are presented.

A Delaunay triangulation of the Voronoi vertices is obtained, see Fig. 2.8(b), so that the displacements $\mathbf{u}^\alpha = \{u_1^\alpha,\ u_2^\alpha\}$ (where α is a Voronoi vertex) can be directly transfered to the triangle mesh. Note that this Delaunay mesh is not the same as the dual mesh of the Voronoi structure which is used in the stress mapping procedure, see Fig. 2.8. The strain increments within each triangle with nodes p, r and q, respectively (in counterclockwise direction), are given by the standard strain-displacement relations:

$$\begin{Bmatrix} \Delta\varepsilon_{11} \\ \Delta\varepsilon_{22} \\ \Delta\varepsilon_{12} \\ \Delta\omega_{12} \end{Bmatrix} = \begin{bmatrix} N^p_{,1} & 0 & N^r_{,1} & 0 & N^q_{,1} & 0 \\ 0 & N^p_{,2} & 0 & N^r_{,2} & 0 & N^q_{,2} \\ \frac{N^p_{,2}}{2} & \frac{N^p_{,1}}{2} & \frac{N^r_{,2}}{2} & \frac{N^r_{,1}}{2} & \frac{N^q_{,2}}{2} & \frac{N^q_{,1}}{2} \\ -\frac{N^p_{,2}}{2} & \frac{N^p_{,1}}{2} & -\frac{N^r_{,2}}{2} & \frac{N^r_{,1}}{2} & \frac{N^q_{,2}}{2} & -\frac{N^q_{,1}}{2} \end{bmatrix} \begin{Bmatrix} \Delta u_1^p \\ \Delta u_2^p \\ \Delta u_1^r \\ \Delta u_2^r \\ \Delta u_1^q \\ \Delta u_2^q \end{Bmatrix}, \tag{2.67}$$

where $N^i,\ (i = p, q, r)$ are the shape functions for a constant strain triangle (Zienkiewicz

[1] In order to obtain an average of the elastic strain fields over many Voronoi realizations, Tekoğlu and Onck (2008) used a square grid. The average of the displacements of the Voronoi vertices (from various Voronoi realizations) lying inside a square have been transfered to the vertices of the square properly. Each square is diagonally divided and standard strain-displacement relations have been applied to get the strains in these constant strain triangles. The strains are then later mapped back to the nodes of the square grid.

and Taylor, 2000).

As is evident from Fig. 2.8(b), long and thin triangles are inevitable, irrespective of the fact whether the Delaunay triangulation is carried out cell-wise or structure-wise. The strains of these triangles, if plotted directly, suffer from an artifact of the improper representation of cell strain (with sharp strain discontinuities across some sides of the constant strain triangles). Thus, a "cell averaging" of the strains is carried out and the strain increments are transfered to the nodes and accumulated. The averaging is employed in two steps. In the first step the average strain increment in a cell is computed by the area weighted average of the strain increments from all the triangles belonging to a cell. In the second step, the average strain increment in a node is computed as the area weighted average of the average strain increments of all the cells sharing the node.

One can also consider other averaging schemes. For example, a one step scheme may be envisioned in which the average strains at the Voronoi vertices can be obtained by weighted averaging over all the triangles that share a node. This scheme can more efficiently represent small variations in the local strains around a node, whereas in the two-step averaging these strains would be more "smeared out" (Van Buuren, 2007). However, the one-step scheme does not yield a unique strain map, due to the possibility of multiple ways of triangulating the cells. Note that Delaunay triangulations of the Voronoi vertices obtained per cell or structure basis are different. Hence, the cell averaging scheme will be used in this thesis as it is independent of the triangulation method.

Based on: Mangipudi, K.R., Van Buuren, S.W. and Onck, P.R. – *"The microstructural origin of strain hardening in two-dimensional open-cell metal foams,"* Int. J. Solids Struct., Vol. 47, No. 16, pp. 2081-2096, 2010.

Chapter 3
Microstructural origin of strain hardening

The question is not what you look at, but what you see.

Henry David Thoreau

This chapter aims at elucidating the microstructural origin of strain hardening in open-cell metal foams. We have developed a multiscale model that allows to study the development of plasticity at two length scales: (i) the development of plastic zones inside individual struts (microscopic scale) and (ii) the formation of plastic localization bands at the scale of the cellular architecture (mesoscopic scale). We address how plasticity at both scales contribute to the macroscopic yielding and strain hardening of cellular metals. One of the important results is that, in contrast to strain hardening in dense metals, strain hardening in cellular metals consist of a synergistic contribution of two sources: (i) strain hardening of the solid material (microscopic scale) and (ii) geometric hardening due to strut reorientation (mesoscopic scale). We show that the synergy of the two leads to an enhanced macroscopic hardening capacity. Our results are in good agreement with experimental studies and elucidate the microstructural origin of plastic hardening in this class of materials.

3.1 Introduction

The mechanical properties of foams, in particular the elastic properties, have been extensively studied (Gibson and Ashby, 1997; Gibson, 2000). Relations between the elastic properties of the foam and its relative density are obtained using dimensional arguments based on their deformation mode (Gibson and Ashby, 1997). Experiments have shown that yielding not only depends on the deviatoric stress, but also has

a strong hydrostatic stress dependence (Triantafilliou et al., 1989; Deshpande and Fleck, 2000; Gioux et al., 2000; Sridhar and Fleck, 2005). Assuming elastic-perfectly plastic behaviour for the bulk material, the yield surface of the foam can be obtained in the hydrostatic and deviatoric stress space (known as the GAZT model, Gibson et al. (1989)), which captures the change in the yield surface with relative density. Phenomenological constitutive models are also proposed, e.g., Deshpande and Fleck (2000), based on the experimental observations. They have also observed that the hydrostatic and shear yield strengths evolve independently at different rates and introduced a differential hardening model to capture the evolution of the yield surface.

From a microstructural perspective, plastic collapse of the foam occurs by the formation of plastic hinges near the strut junctions and the progressive formation of deformation bands (Bastawros et al., 2000). Theoretical models have shown that the randomness in cell shape (Silva and Gibson, 1997a; Silva et al., 1995; Zhu et al., 2001a), imperfections (Chen et al., 1999) and the cell wall shape (Harders et al., 2005; Gong et al., 2005) influence the overall properties, in particular the plastic collapse stress. The imperfections such as cell wall misalignment or waviness cause the foam to yield at much lower applied hydrostatic stresses compared to the foam with a regular, perfect microstructure (Chen et al., 1999). The presence of non-uniform strut cross sections slightly increases the uniaxial yield strength (Chen et al., 1999; Kim and Al-Hasani, 2001, 2002) and slightly decreases the hydrostatic yield strength (Chen et al., 1999).

After the initiation of yielding, the deformation of the foams is controlled by the strain hardening of the solid material. The effect of linear strain hardening in hexagonal honeycombs under compression was reported by Papka and Kyriakides (1994). They found that the plastic response of the honeycomb is related to the bulk material hardening. A few more attempts, both experimentally as well as theoretically, have addressed the strain hardening in foams (Despois et al., 2004; Marchi and Mortensen, 2001; Marchi et al., 2004; Amsterdam et al., 2008a). Marchi and Mortensen (2001) showed that (at small strains) the hardening exponent of the foam is identical to that of the solid material and proposed a stress-strain law for the foam accounting for the relative density. In a number of experiments reported in Amsterdam et al. (2008a) this has been verified with the scaling of the peak stress. However, at large strains, the analysis of Despois et al. (2004) is not valid due to the geometric non-linearities involved. Thus, the strain hardening in foams at arbitrary deformations remains to be understood and forms the subject of this chapter.

Strain hardening is not only important for the structural integrity of components that are limited by extreme plastic deformation, but also plays an important role in controlling the onset of damage. Fracture behaviour of metal foams has generated much interest recently (Motz and Pippan, 2002; Schmidt and Fleck, 2001; Onck et al.,

2004; Amsterdam et al., 2008a,b,c). Amsterdam et al. (2008b) have shown that the onset and evolution of damage in the foam depends sensitively on the yield stress and hardening exponent of the solid material. Insight of the relation between strain hardening and damage is not only of fundamental interest, but also has a strong industrial importance in improving the production technologies and post-fabrication heat treatments.

The goal of this chapter is to provide a full understanding of the relation between the plastic properties of the strut material and the overall hardening behaviour of the foam. We will use the model from 2.2 to investigate the effect of solid material strain hardening on the spread of plastic deformation inside the struts as well as at the cellular microstructure level. In addition, the consequences for damage initiation for a range of heat treatments will be analysed.

The chapter is organized as follows. In section 2.2, the plastic constitutive laws for the stress resultants at the strut level will be derived and implemented in a finite element discretization of the foam. In sections 3.2.1 and 3.2.2, simulations with regular hexagonal and Voronoi honeycomb structures are presented showing the development of plasticity at the strut and microstructural level. The underlying mechanism of hardening will be summarized in section 3.2.3. Scaling relations for hardening will be investigated in section 3.2.4. Finally, in a case study, two heat treatments will be compared in section 3.2.5.

3.2 Results and discussion

Uniaxial loading simulations were performed on two different kinds of structures: a regular hexagonal honeycomb structure (Section 3.2.1) and a two-dimensional random Voronoi structure (Section 3.2.2). Fig. 3.1(a) shows the unit cell (solid lines) chosen to study the regular hexagonal honeycomb (dashed lines). Because of the symmetry, we only need to analyze one quarter of the unit cell (indicated by thick solid lines). Following a convergence study on the unit cell, a discretization of 100 equal-sized elements per strut has been used. Two sets of boundary conditions are employed in this study: uniaxial tension and uniaxial straining. For the former the boundary conditions are $u = v = \phi = 0$ at A, $u = f_y = \phi = 0$ at B and $f_x = m = 0,\ v = U$ at C. With this set of boundary conditions, the deformation of the honeycomb is essentially bending dominated. For the uniaxial straining case, we additionally constrain the horizontal displacements at C, which will result in zero lateral strain and a much greater axial deformation in the inclined strut. For Voronois, a network of 16×20 (width × height) cells with a mesh of 60 elements per strut has been found to converge. A typical network is shown in Fig. 3.1(b) along with the boundary conditions. The Voronoi structures are generated using a regularity parameter of 0.9

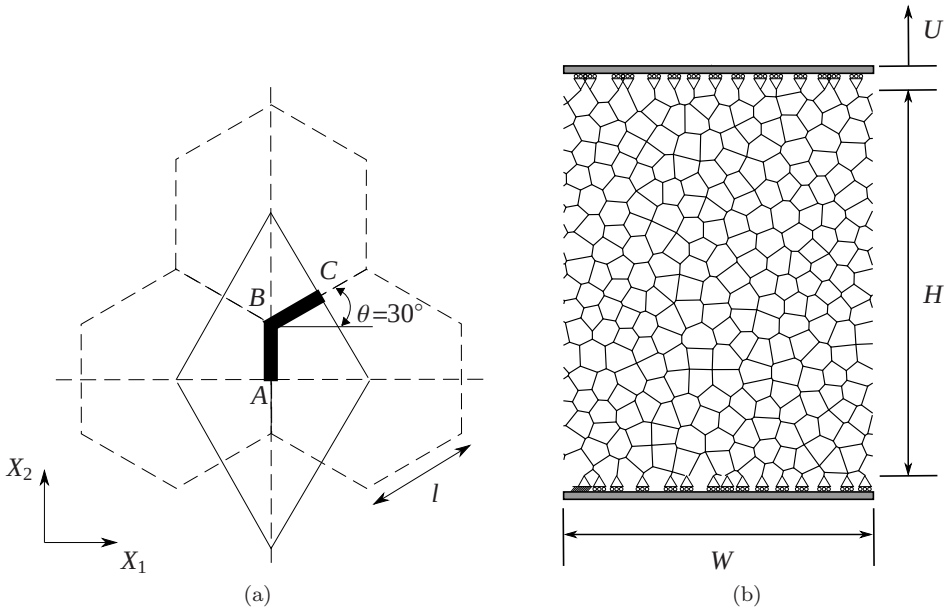

Figure 3.1: (a) Unit cell of a regular hexagonal honeycomb structure. (b) Random Voronoi structure.

(Zhu et al., 2001b). Unless otherwise stated, all the simulations are performed with the coupled strain model of section 2.2.2.

The input parameters for the material model are the yield stress (σ_{Y}), Young's Modulus (E_{s}) and strain hardening exponent (N_{s}) of the solid material. The Young's Modulus is 70 GPa in all the calculations presented here. During the parametric study, N_{s} and σ_{Y} are systematically varied such that $N_{\mathrm{s}} = 0.1$, 0.2 and 0.3, while σ_{Y} = 50 MPa, 100 MPa, 150 MPa, 200 MPa, 250 MPa and 300 MPa. In case of linear strain hardening, the plastic tangent modulus H_{s} is chosen to be 5 GPa to give a comparable hardening slope as the power law relation with $N_{\mathrm{s}} = 0.2$.

For a regular hexagonal structure, the relative density ρ^*/ρ_{s} depends on the strut's thickness over length ratio t/l according to $\rho^*/\rho_{\mathrm{s}} = (2/\sqrt{3})(t/l)$ (Gibson and Ashby, 1997). For Voronoi honeycombs, an average thickness t_{avg} is assigned to every strut such that $t_{avg} = (WH/L)(\rho^*/\rho_{\mathrm{s}})$ where W and H are the width and height of the Voronoi and L is the total strut length. Hence, in both cases the strut thickness is uniform over the structure. Unless it is specifically stated, we take the following default values: for the unit cell $t/l = 0.1$ ($\rho^*/\rho_{\mathrm{s}} = 0.115$) and $\rho^*/\rho_{\mathrm{s}} = 0.12$ for the Voronoi structures and $\sigma_{\mathrm{Y}} = 150$ MPa.

It should be noted, however, that the relative density, calculated by the above

mentioned procedure, is overestimated. This is due to the fact that the material from the overlapping/intersecting portions of the struts at the nodes is counted more than once. The resulting error in relative density increases with increasing strut thickness t and will be larger for a non-uniform strut profile as the strut thickness increases towards the nodes (Gong et al., 2005). In foam models represented by structural elements, this problem can be avoided by connecting the struts to the surface of rigid nodes instead of connecting to their centre (Warren and Kraynik, 1987; Chuang and Huang, 2002). Gong et al. (2005) have used three-dimensional geometric models (where the intersecting strut material is removed and the nodes are trimmed with smooth surfaces) to obtain a relationship between the corrected relative density and the strut dimensions. It should also be noted that for large relative densities the ratio t/l increases, so that shear deformations increasingly contribute to the overall compliance (see Gong et al. (2005)). In this study we do not account for this, but restrict ourselves to densities smaller than 20% for which the errors remain limited.

In all the simulations the out-of-plane thickness b is taken to be unity, so that the forces and the moments are per unit out-of-plane thickness. The overall stresses σ^* and strains ϵ^* are calculated as follows. If F is the force in the vertical direction at point C of the unit cell in Fig. 3.1(a), the stress σ^* on the regular hexagonal honeycomb is calculated as $2F/(\sqrt{3}l)$ and the strain ϵ^* is $4U/(3l)$. For the Voronoi structures, summation of all the vertical forces at the top boundary nodes divided by the width of the structure gives the overall stress σ^*. The strain ϵ^* follows from U/H (see Fig. 3.1(b)). Both the regular hexagons and Voronoi stresses σ^* are normalized by the plastic collapse stress σ^*_{pl} of a regular hexagonal honeycomb of corresponding relative density given by Eq.3.3.

3.2.1 Evolution of plasticity in regular hexagonal honeycomb structures

Strut deformation and triple point behaviour

In the unit cell shown in Fig. 3.1(a), only the inclined strut (strut BC) is subjected to bending while the vertical strut (strut AB) only experiences uniaxial tension for both sets of boundary conditions. In the constrained case of uniaxial straining, the axial forces in the inclined strut will be large and will show a mixed type of loading. To understand the role of plastic hardening at the triple points, the stress-strain response of the unit cell is studied and is related to the evolution of the stress profile in strut BC near the triple point (the point $x = 0$ along the length of BC).

Figure 3.2(a) shows the overall stress-strain curve of a regular hexagonal structure subjected to uniaxial tension. The stress profiles near the triple point ($x = 0$ of strut BC in Fig. 3.1(a)) and the elastic-plastic boundaries along the inclined strut are

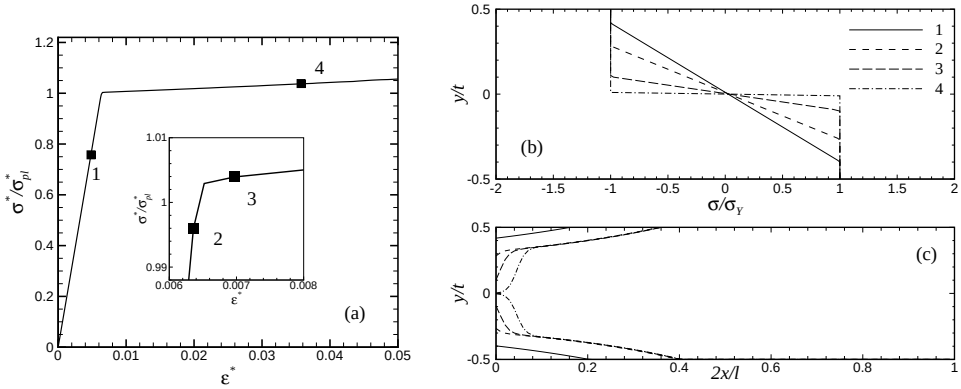

Figure 3.2: Regular hexagonal honeycomb of perfectly-plastic solid material subjected to uniaxial tension: (a) stress-strain curve, (b) evolution of stress profiles at $x = 0$ in the inclined strut and (c) evolution of elastic plastic boundary along the length of the inclined strut. In the inset of (a), the stress-strain curve is magnified near the sharp "knee" of the curve. The profiles in (b) and (c) are plotted at overall strains corresponding to the labeled points in (a). The line styles in (b) and (c) are related.

shown in Fig. 3.2(b) and 3.2(c), respectively, for different overall strains. For these boundary conditions, the deformation of the inclined strut is entirely dominated by bending. This can be seen from the nearly symmetric stress and elastic-plastic boundary profiles in Figs. 3.2(b) and 3.2(c). While the stress profile at the triple point in Fig. 3.2(b) reflects the perfectly-plastic material behaviour, the overall behaviour of the unit cell is not perfectly plastic and shows a slight hardening. The increase in the stress during macroscopic plastic straining is attributed to the reorientation of the inclined struts. This mechanism will be discussed in detail in section 3.2.3. The evolution of the elastic-plastic boundary in Fig. 3.2(c) can be explained as follows. Initially, yielding of the top and bottom surface fibers occurs in the inclined member of the unit cell near the triple point. Due to the presence of a large elastic core, the tangent stiffness of the strut is close to the elastic stiffness and leads to the yielding of the surface and subsurface fibers in the adjacent regions, see the solid contour lines in Fig. 3.2(c). This elastic-plastic front initially spreads laterally along the length of the strut. Since the solid material is an elastic-perfectly-plastic material, soon the lateral spreading ceases and a localized plastic hinge develops near the triple point (see Fig. 3.2(c)) by the progressive yielding of all the fibers of the cross section (approximately at the instant 3 in Fig. 3.2(a)).

In case of a strain hardening solid material, such as the one shown in Fig. 3.3, localized hinge formation is hindered and a more diffuse plastic zone forms with

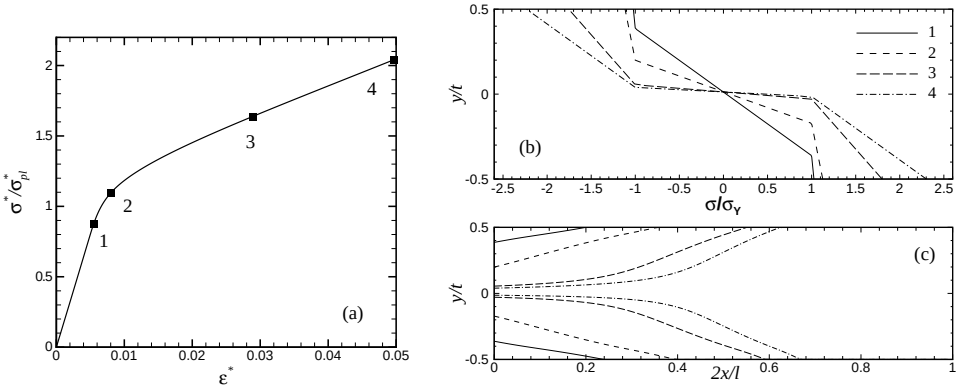

Figure 3.3: Regular hexagonal honeycomb of linear strain hardening solid material subjected to uniaxial tension. The relation between the labels and line styles is analogous to that in Fig. 3.2.

increasing strain (Fig. 3.3(c)). The transition from the elastic to plastic slope in the stress-strain curve occurs gradually due to the progressive yielding in the strut thickness and length directions. By comparing Fig. 3.2(c) with Fig. 3.3(c) one can notice that the strain hardening is related to spreading of plasticity along the strut length. With a linear strain hardening solid material (Fig. 3.3(a)), the hardening in the structure is also linear after a small non-linear transition period. The stress profile at the triple point, Fig. 3.3(b), is bi-linear since the fiber strain varies linearly with the thickness. In Fig. 3.4, the results for a regular hexagonal honeycomb under the same type of loading but with a power law material behaviour are shown. The solid material behaviour is reflected in the overall stress-strain behaviour and the elastic-plastic boundary evolution is similar to the linear hardening case.

The hexagonal structure is much stronger under uniaxial straining (Fig. 3.5(a)) compared to uniaxial tension (Fig. 3.4(a)). This is due to the fact that now the structure is under biaxial tension and the net bending moment near the triple point is reduced (Gibson and Ashby, 1997). The small elastic-plastic transition region after initial yielding, shown in the inset of Fig. 3.5(a) can be related to the presence of a minor bending strain in addition to a major axial strain. Since under these conditions the strut deformation is dominated by axial force, we only observe one elastic-plastic boundary which started from the bottom of the strut (solid line) and swept the entire strut length, finally disappearing on the top left side of the strut when the entire strut has become plastic. The reason for the large difference in overall strength can be related to the different deformation mechanism in the inclined strut (stretching vs. bending). A regular hexagonal structure with linear material hardening behaviour

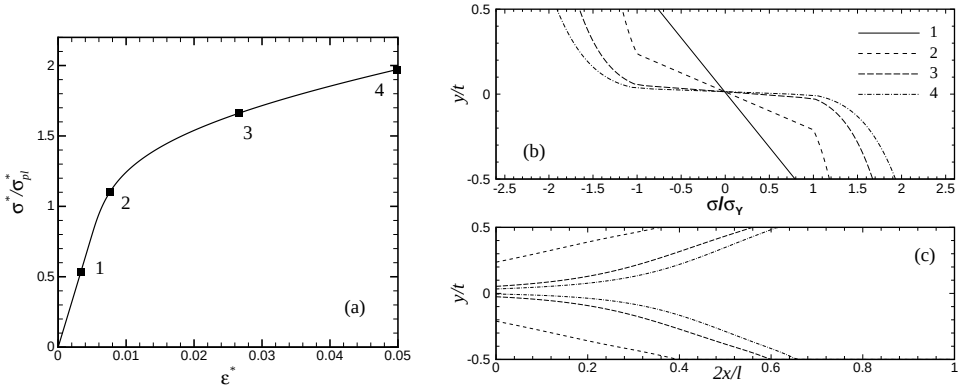

Figure 3.4: Regular hexagonal honeycomb of power law hardening solid material (N_s = 0.2) subjected to uniaxial tension. The relation between the labels and line styles is analogous to that in the Fig. 3.2.

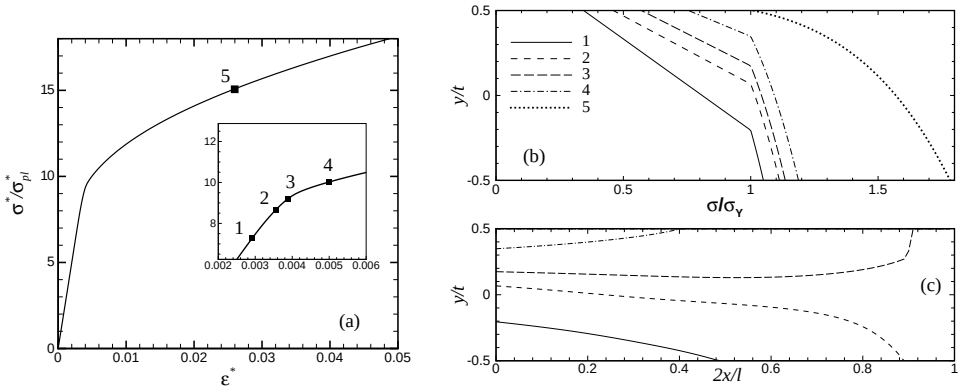

Figure 3.5: Regular hexagonal honeycomb of power law hardening solid material (N_s = 0.2) subjected to uniaxial straining. In the inset a magnified view of the "knee" in the stress-strain curve is shown. The relation between the labels and line styles is analogous to that in the Fig. 3.2.

also shows a similar trend and is not reported here to avoid repetition.

The stress-strain behaviour for different N_s is compared in Fig. 3.6(b) for uniaxial tensile loading. For comparison, the solid material behaviour is also shown in Fig. 3.6(a). As the strain hardening exponent of the material is increased, the hardening exponent of the structure also increases, but is not equal to that of the solid material as will be shown later. The effect of strain hardening on the stress state at the triple point and the plastic zone size and shape in the inclined strut of the unit cell is

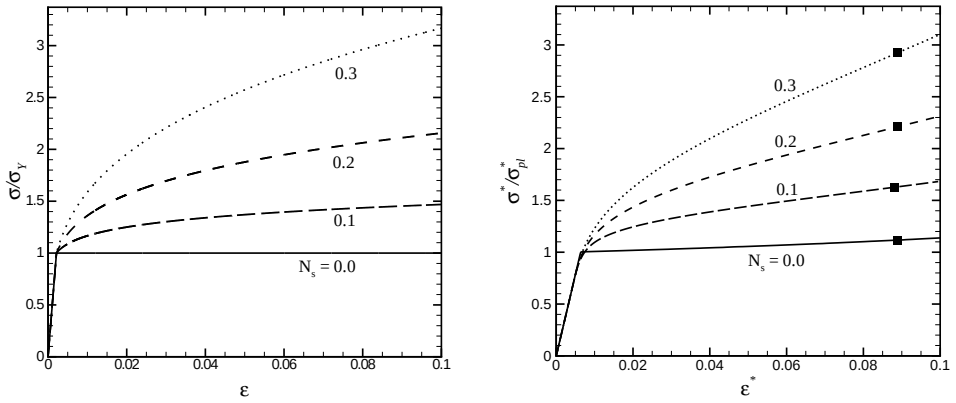

(a) (b)

Figure 3.6: Stress-strain behaviour of a regular hexagonal honeycomb subjected to uniaxial tension (figure b) for the solid material behaviour shown in figure (a). The yield stress of the solid material is kept constant and N_s is varied.

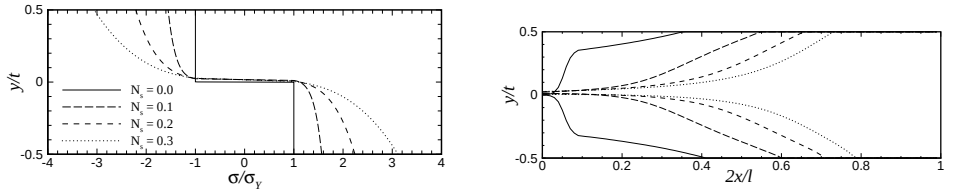

(a) (b)

Figure 3.7: Comparison of stress profiles and elastic-plastic boundaries. The stress profiles are at $x = 0$ in the inclined strut. The elastic-plastic boundaries are plotted at the same macroscopic strain $\epsilon^* = 0.9$ corresponding to the symbols in Fig. 3.6(b). The line styles in (a) and (b) are related.

presented in Figs. 3.7(a) and 3.7(b), respectively. For an elastic-perfectly-plastic solid material, a localized plastic hinge forms. When the material's hardening is increased, the plastic zone size increases and spreads out over a large region. It can be observed that at an overall strain of 9%, at least 75% of the strut length has started to yield for $N_s = 0.3$.

Effect of non-uniform cross section

The strut profile is usually concave in shape. In various studies, this shape is mimicked using linear (Chen et al., 1999) and nonlinear profiles (Harders et al., 2005;

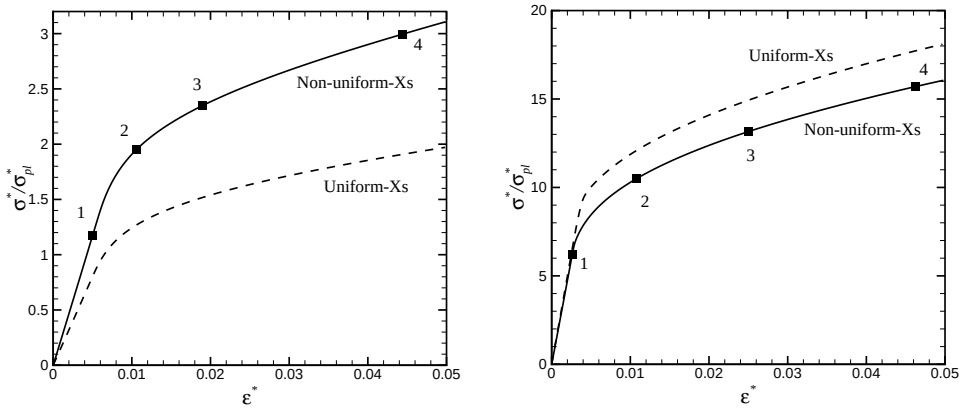

Figure 3.8: Comparison between regular hexagonal honeycombs with uniform and non-uniform cell wall thicknesses and for a power law hardening material with $N_s = 0.2$. Figure (a) is for uniaxial tension and figure (b) is for uniaxial straining.

Gong et al., 2005; Onck et al., 2004). Here we consider a parabolic strut profile (Harders et al., 2005) given by

$$t(\bar{x}) = t_0 \left[3(1 - t_{\text{rel}}) \left(\frac{2(\bar{x} - 1)}{l_0} \right)^2 + t_{\text{rel}} \right]. \tag{3.1}$$

The long axis of the strut is parametrized by $\bar{x} = 2x/l \in [0, 2]$. The surface area of the strut (i.e. the strut volume per unit out-of-plane thickness) is determined by t_0 and the profile variation is given by the parameter $t_{\text{rel}} = t(\bar{x} = 1)/t_0$, $0 < t_{\text{rel}} \leq 1$. This relation ensures a constant surface area per strut for different t_{rel}, allowing comparison of different strut profiles for the same relative density. In the following simulations with non-uniform strut thickness, we take $t_{\text{rel}} = 0.7$ for which the corresponding strut shape can be seen, for example, in Fig. 3.9(a). For bending structures it is known that a non-uniform strut, which is thicker at its ends, has a higher elastic stiffness compared to a uniform strut with the same strut volume. The reason for this is that at the location of high bending moment the strut is thicker and thus more resistant to bending deformation owing to the cubic thickness dependence of the bending stiffness. Figure 3.8(a) also shows a higher yield strength for the unit cell with non-uniform struts under uniaxial tension. Since the strut is thicker near the triple point, for a given bending moment the maximum stress developed at the outer fibers will be lower in case of a non-uniform strut. In this scenario, the initiation of

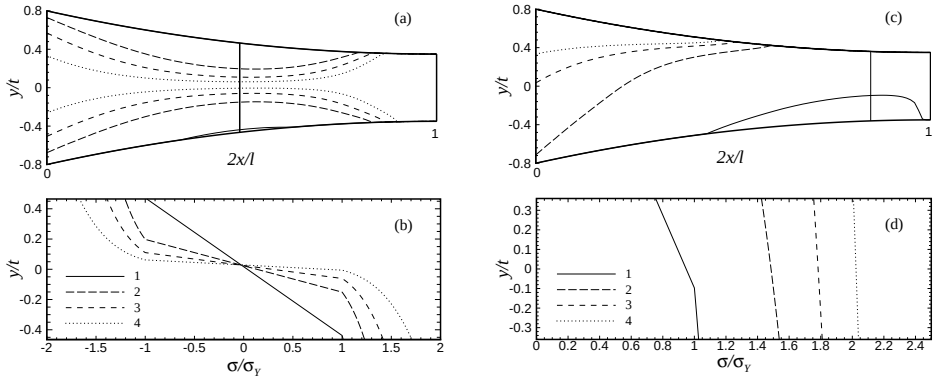

Figure 3.9: Evolution of the elastic-plastic boundaries for non-uniform struts under uniaxial tension (a) and for uniaxial straining (c). The corresponding stress profiles at the location indicated by the vertical line in (a) and (c) are plotted in (b) and (d), respectively, for a power law hardening material with $N_s = 0.3$. The stress profiles and the elastic-plastic boundaries with similar line styles correspond to the labeled points on the stress-strain curves in Fig. 3.8.

yielding and the formation of the plastic hinge occurs at a location away from the triple point depending on the thickness variation as can be seen from Fig. 3.9(a). A diffused hinge formation can also be observed. A non-uniform strut also has a higher hardening slope due to geometric hardening induced by greater reorientation of the inclined strut (see Fig. 3.8(a)).

Under uniaxial straining, since the inclined member undergoes larger axial deformation (Fig. 3.9(d)), the elastic modulus of the structure depends to a greater extent on the axial stiffness compared to the bending stiffness. For the combination of strut shape and t_{rel} used in Fig. 3.8(b), the axial stiffness of a non-uniform strut is close to the axial stiffness of a uniform strut (refer Fig. 5 of Harders et al. (2005)). Hence, the regular hexagonal structure with non-uniform struts exhibits an elastic modulus close to the one with uniform struts (see Fig. 3.8(b)). On the other hand, the yield strength is lower for the non-uniform strut, since yielding occurs under predominant tension at a cross section which is thinner compared to the uniform strut of the same relative density (compare Figs. 3.5(c) and 3.9(c)). However, the overall elastic-plastic stress-strain response of the structure with non-uniform struts approaches that of the structure with uniform struts as $t_{rel} \to 1$. Similar behaviour has also been observed for linear hardening under both types of boundary conditions which is not presented in this chapter.

It has been shown in the literature that a structure with non-uniform strut cross sections is stiffer and stronger in comparison with uniform strut cross sections (Gong

et al., 2005; Kim and Al-Hasani, 2002, 2001; Chuang and Huang, 2002; Li et al., 2006). This is true when the loading is bending dominated as is the case under uniaxial tension. However, as the axial deformation mode becomes more prominent, as is the case under uniaxial straining, the opposite is true, at least for the plastic response.

3.2.2 Evolution of plasticity in random Voronoi structures

In this section, simulations on random Voronoi structures with uniform strut cross section are presented. The stress-stain curves for tension and compression are shown in Fig. 3.10 for $N_s = 0$, 0.1 and 0.2. When loaded either in tension or in compression, the struts start to yield near the triple points following the initial elastic deformation. These yielding events occur at random locations in the structure. Quickly (within 1% overall strain) a considerably large fraction of the strut length (see Fig. 3.11(a)), mainly constituting the triple points (see Fig. 3.11(b)), becomes plastic. Further yielding of the struts depends on the solid material hardening. An increased hardening capacity of the solid material leads to higher stresses in the plastic zone which will induce yielding in its neighbouring elastic regions. This effect is evident in Fig. 3.11 showing that the structure with elastic-perfectly plastic material ($N_s = 0$) shows a lower plastic strut length (l_{pl}) compared to the one with power law hardening material. In Fig. 3.11(a), l_{tot} is the sum of all strut lengths and l_{pl}/l_{tot} is its fraction that has plastically yielded. Irrespective of the hardening of the solid material, structures under tension always show a larger plastic strut length compared to the structures in compression. This is due to the reorientation of the struts towards the loading direction in tension. It should be noted here that in calculating l_{pl} in Fig. 3.11, the entire length of a beam finite element is counted if at least one of its outer fibers has yielded. Hence, in order to get a complete picture of plasticity in these networks one has to relate Fig. 3.11 with Fig. 3.7(b).

Typical strain maps of a Voronoi structure under tension for the three values of N_s considered here are shown in Fig. 3.12. The strain distribution can be found to be uniform for all N_s values. The stress-strain response of a Voronoi is similar in trend to that of a hexagonal structure. For a Voronoi structure with an elastic-perfectly plastic cell wall material subjected to uniaxial compression, following the random yielding of the triple points, a localized strain band is formed due to the plastic collapse of the cells within a weak path. This localization occurs in a very narrow band of cells and is characterized by its very high local strains as can be observed in Fig. 3.13(a). This collapse band produces a peak in the overall stress-strain curve shown in Fig. 3.10(b). However, this strain localization is hampered when the solid material can harden. As has been observed with the hexagonal structure, hardening

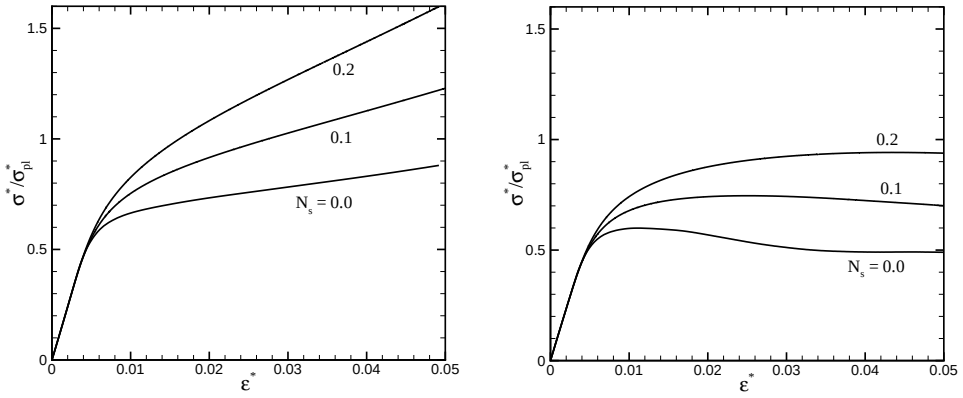

Figure 3.10: Stress strain curves of a Voronoi network for different hardening exponents. Figure (a) is for tensile loading and figure (b) is for compressive loading.

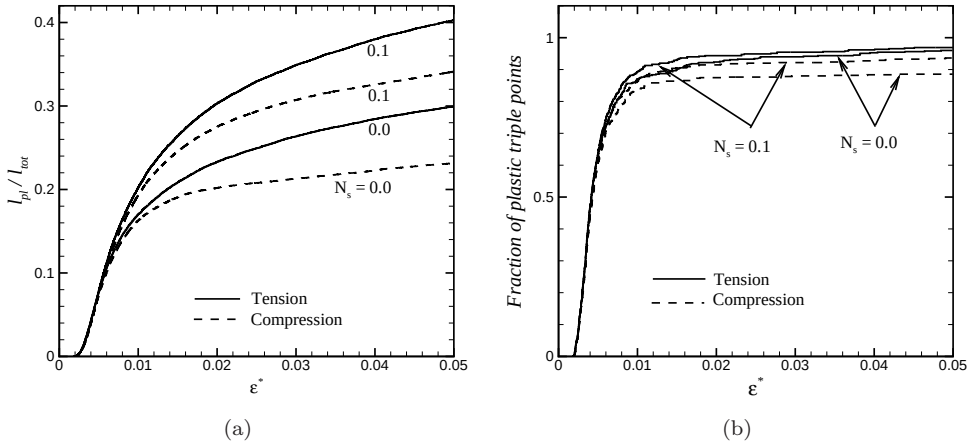

Figure 3.11: Plasticity in Voronoi structures: (a) Fraction of plastic strut length and (b) fraction of yielded triple points. In figure (b), a triple point is said to have yielded if at least one of the struts meeting at this triple point forms a hinge.

of solid material leads to diffused plasticity along the struts that increases the local stresses, thus leading to a more uniform strain distribution, which even tends to become uniform at higher N_s (refer to Fig. 3.13). Due to the absence of localized deformation for $N_s > 0$, no clear peak can be observed in the stress-strain curve in Fig. 3.10(b). Similar to tension, an increased N_s leads to increased plastic strut length

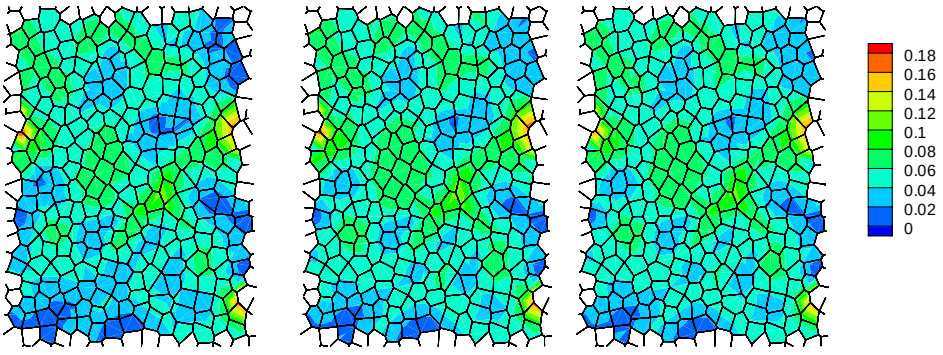

(a) Perfect plasticity (b) $N_s = 0.1$ (c) $N_s = 0.2$

Figure 3.12: Strain maps in tension plotted at an overall strain $\epsilon^* = 0.05$ in Fig.3.10(a).

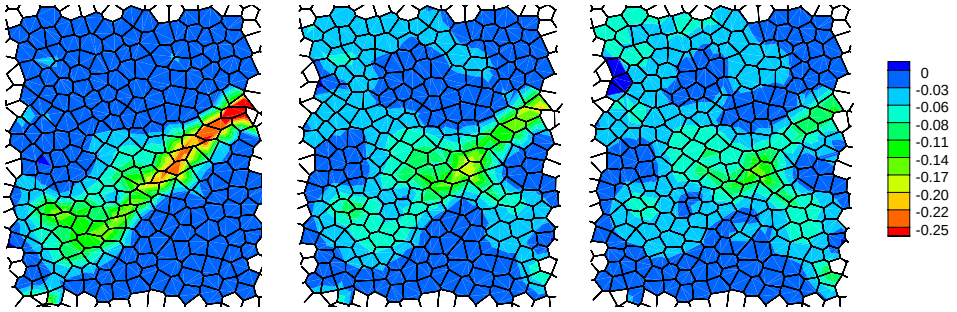

(a) Perfect plasticity (b) $N_s = 0.1$ (c) $N_s = 0.2$

Figure 3.13: Strain maps in compression plotted at an overall strain $\epsilon^* = 0.048$ in Fig.3.10(b).

(see Fig. 3.11(a)). For both perfectly plastic and power law hardening behaviour, the rate of plasticity development, related to the slope of the curves in Fig. 3.11, is lower in compression due to strain localization.

3.2.3 Mechanism of hardening

It has been mentioned previously that the tensile stress-strain response of the hexagonal structure with elastic-perfectly-plastic material behaviour exhibits some hardening (see Fig. 3.6(b)). Since the structure under tension tends to align its inclined strut along the loading axis, the axial force along the strut increases with loading. When the axial deformation is increased significantly, it has been shown previously in this study that the cellular material tends to become stronger (cf. uniaxial ten-

sion and uniaxial straining conditions). The net effect is an increasing load bearing capacity with straining. We refer to this mechanism of hardening due to geometry changes as '*geometric hardening*'.

This mechanism of hardening is found to interact with the material's intrinsic strain hardening, leading to an overall hardening that is more than the sum of the two. To investigate the effect of geometric hardening, we also perform simulations that do not account for finite geometry effects. In other words, the geometry of the unit cell has been frozen without updating the nodal co-ordinates in the finite element calculations. We call this setup as *fixed* geometry, to distinguish it from the from the usual procedure that we will refer to as *updated* geometry. For simplicity, linear material hardening is discussed here.

Fig. 3.14(a) shows a curve for the elastic-perfectly plastic material behaviour in a fixed geometry scenario, which will be referred to as the base curve hereafter. In this case, after a small elastic-plastic transition region, a constant stress plateau is reached showing no signs of hardening. The small transition region is a result of the progressive formation of the plastic hinge (see Fig. 3.2). In addition, two more combinations were considered: (a) including geometric hardening but no material hardening (perfectly-plastic behaviour, updated geometry) and (b) including only material hardening but no geometric hardening (material hardening, fixed geometry). The dashed line in Fig. 3.14(a) is constructed by adding the pure geometric hardening (the difference between the perfectly plastic, updated geometry curve and the base curve) and pure material hardening (the difference between material hardening, fixed geometry curve and the base curve) to the base curve. If the overall hardening were a linear combination of geometric and material hardening, the reconstructed curve (dashed line) would have coincided with the curve for updated geometry and material hardening (where the geometric and material effects are both present at the same time). Apparently this is not the case. Moreover, the difference between the derived curve and the regular curve increases non-linearly with increasing plastic strain indicating that these two kinds of hardening interact continuously. Under compression the effect of the geometry is to produce some softening. Thus, the perfectly-plastic material with updated geometry lies below the base curve in Fig. 3.14(b). The same synergy can be seen in compression but now as a combination of material hardening and geometric softening. Similar curves for Voronois are shown in Fig. 3.15 and the effect is similar on the overall behaviour. The slopes of the curves in Fig. 3.15(a) indicate that depending on the strain hardening capacity and relative density, the geometric hardening may possibly dominate the material hardening at larger strains in the absence of damage.

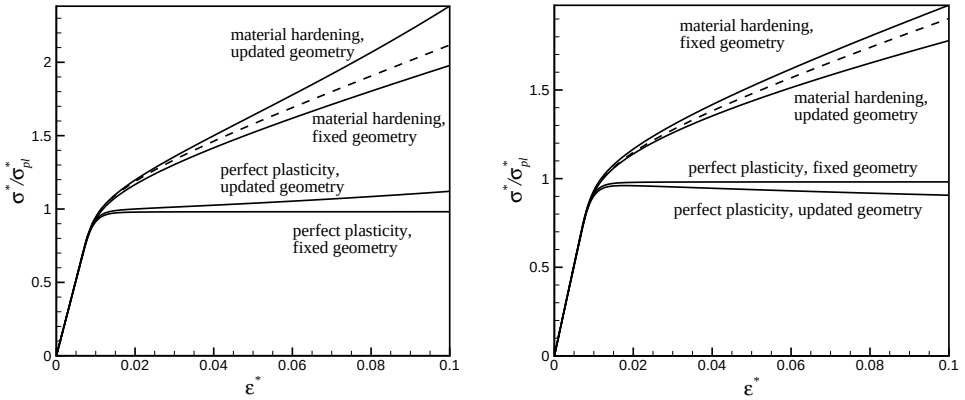

(a) (b)

Figure 3.14: Synergy of material and geometric hardening in regular hexagonal honeycombs ($\rho^*/\rho_s = 0.08$). The dashed line is a reconstruction (refer to the text for explanation), while the solid lines are obtained from simulations. Figure (a) is for tension while (b) is for compression.

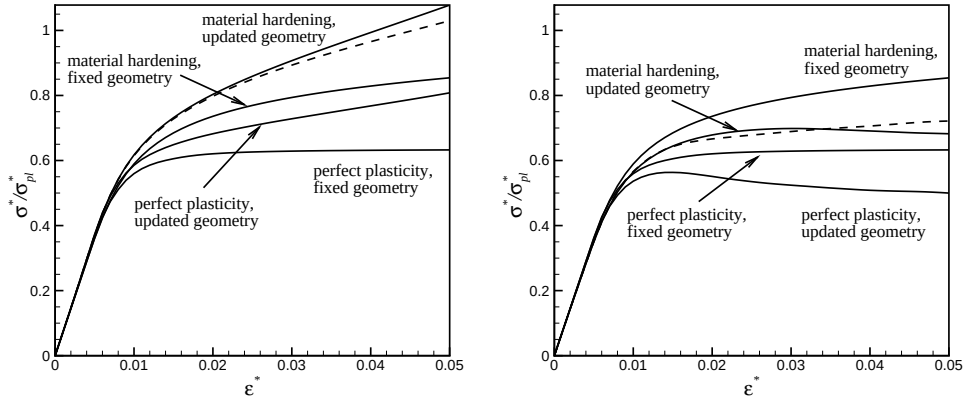

(a) (b)

Figure 3.15: Synergy of material and geometric hardening in a Voronoi honeycomb ($\rho^*/\rho_s = 0.08$). The dashed line is a reconstruction (refer to the text for explanation), while the solid lines are obtained from simulations. Figure (a) is for tension while (b) is for compression.

3.2.4 The effect of density on hardening

In this section, we will study how density will affect the hardening behaviour. In subsection 3.2.4, we will focus on linear hardening for which closed-form expressions for the overall hardening as a function of relative density will be obtained. In subsection 3.2.4, we study the effect of density on power law hardening cellular solids. Numerical simulations will be fitted to obtain expressions that describe the overall hardening exponent as a function of the solid's hardening exponent, relative density and the solid's yield stress.

Linear hardening

By considering a regular hexagonal honeycomb (see Fig. 3.1(a)), with uniform cell wall thickness t and strut length l, scaling of the elastic modulus and the plastic collapse strength of the regular hexagonal honeycomb with perfectly plastic cell wall material is given by Gibson and Ashby (1997) as

$$\frac{E_1^*}{E_s} = \frac{E_2^*}{E_s} = \frac{4}{\sqrt{3}}\left(\frac{t}{l}\right)^3, \tag{3.2}$$

and

$$\frac{(\sigma_{pl}^*)_1}{\sigma_Y} = \frac{(\sigma_{pl}^*)_2}{\sigma_Y} = \frac{2}{3}\left(\frac{t}{l}\right)^2 \tag{3.3}$$

respectively. Here E_s is the elastic modulus of the solid material, E^* is that of the structure and σ_{pl}^* is the plastic collapse strength. These relations are obtained with the assumptions of (i) small deformation, (ii) small strain, (iii) perfectly plastic cell wall material, (iv) sudden yielding of the entire cross section forming a localized hinge and (v) neglecting the effect of axial stress. For a linear strain hardening cell wall material, such as the one in Fig. 3.3, a non-linear transition regime occurs due to the spreading of the plastic zone in the strut thickness and length directions. After this non-linear response, a linear regime prevails until the geometric effects become significant. When the strain hardening is sufficiently high, the plastic zone covers most of the strut volume beyond the non-linear transition regime. In this section, to derive scaling relation for the plastic tangent modulus H^*, we (a) neglect the non-linear transition, (b) assume small deformations and (c) assume yielding of the entire strut volume.

Let the solid material hardening be given by Eq. 2.7 where the plastic tangent modulus H of the solid material will be referred to here as H_s. Now let us consider an increase in the stress $\Delta\sigma_2^*$ in the plastic regime (see Fig. 3.16). The corresponding increase in the transverse force on the inclined strut ΔF will raise the cross section stress σ by an amount $\Delta\sigma = H_s\Delta\varepsilon$. The increase in the moment at a distance x from

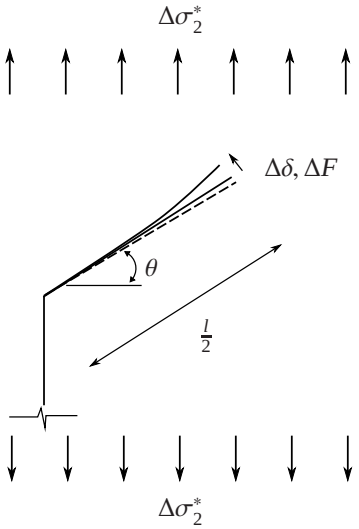

Figure 3.16: Loading in regular hexagonal honeycomb.

the triple point can be related to the increase in force through

$$\Delta M = \Delta F \left(\frac{l}{2} - x \right). \tag{3.4}$$

Assuming that plane sections remain plane during plastic deformation, we use Eqs. 2.4 and 2.6 to obtain the incremental moment-curvature relation as

$$\Delta M = H_s I \Delta\kappa = H_s I \frac{d^2 \Delta v}{dx^2} \tag{3.5}$$

where I is the moment of inertia. Substituting Eq. 3.4 in Eq. 3.5 and solving for the transverse deflection Δv along with the boundary conditions $\Delta v(x = 0) = 0$ and $(\frac{d\Delta v}{dx})(x = 0) = 0$, we obtain the deflection of the inclined strut $\Delta\delta = \Delta v(x = l)$ as

$$\Delta\delta = \frac{\Delta F}{b H_s} \left(\frac{l}{t} \right)^3. \tag{3.6}$$

The increment in the macroscopic strain is

$$\Delta\epsilon_2^* = \frac{\Delta\delta \cos\theta}{l(1 + \sin\theta)}. \tag{3.7}$$

Noting that $\Delta F = \Delta\sigma_2^* bl \cos^2\theta$ and combining Eqs. 3.6 and 3.7, the plastic tangent

modulus H^* of the structure is obtained as

$$H_2^* = \frac{\Delta\sigma_2^*}{\Delta\epsilon_2^*} = H_s \frac{1+\sin\theta}{\cos^3\theta}\left(\frac{t}{l}\right)^3. \tag{3.8}$$

Using similar arguments the tangent modulus for loading in the 1-direction can be shown to be

$$H_1^* = \frac{\Delta\sigma_1^*}{\Delta\epsilon_1^*} = H_s \frac{\cos\theta}{(1+\sin\theta)\sin^2\theta}\left(\frac{t}{l}\right)^3. \tag{3.9}$$

Hence, the scaling of the in-plane plastic tangent moduli (H_1^* and H_2^*) for a regular hexagonal honeycomb at small deformations reduces to

$$\frac{H_1^*}{H_s} = \frac{H_2^*}{H_s} = \frac{4}{\sqrt{3}}\left(\frac{t}{l}\right)^3. \tag{3.10}$$

Note that by setting $H_s = E_s$, one recovers Eq. 3.2, showing that the scaling of the plastic modulus is the same as that of the elastic modulus (Eq. 3.2) for hexagonal honeycombs. When cellular structures are arranged into groups based on their spatial dimension and deformation mechanism, then, irrespective of the spatial architecture of the cell structure, the properties of all cellular structures of one group scale with the same power of relative density (Gibson and Ashby, 1997). The architectural information is collected into the coefficient outside the relative density term in these scaling relations. It is only this coefficient that differs from one structure to the other. For regular structures these are obtained analytically; whereas in the case of irregular structures these have to be obtained by fitting the scaling relation to the experimental or numerical data.

Next we compare our numerical results to the analytical scaling relation derived above. The uncoupled strain model (section 2.2.1) is used. In order to identify the influence of large deformations in the structure which leads to strut reorientation, we use two approaches: small deformations (i.e. fixed geometry) and finite deformations (i.e. updated geometry), refer to section 3.2.3. The plastic tangent modulus H^* of the structure is obtained from the slope of the overall stress-strain curves in the plastic regime, $H^* = d\sigma^*/d\epsilon^*$. Under either tension or compression, the plastic tangent modulus after the elastic-plastic transition in the small deformation regime first decreases with overall strain. When the relative volume of struts that yield increases (see Fig. 3.11), eventually this will saturate and the modulus converges to a unique value. This holds for compression at finite deformations as well. However, for tension at finite deformations, the simulations result in a slope that first decreases (due to increased yielding) and then slowly increases (due to orientational hardening). For the scaling studies, the minimum slope is taken for the tension calculations and the

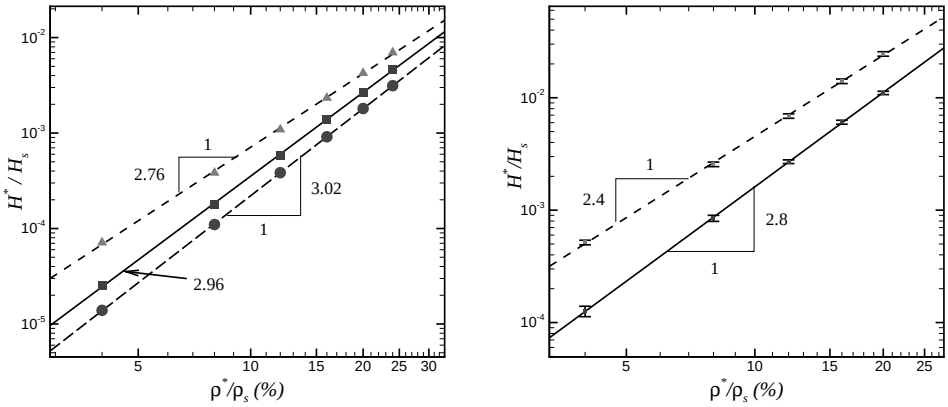

Figure 3.17: Scaling of the plastic tangent modulus (a) for regular hexagonal honeycombs (b) for random Voronoi honeycombs. The solid line is for small deformations (identical in tension and compression). The dashed line is for finite deformations in tension and the long-dashed line is for finite deformations in compression (shown only for hexagonal honeycombs). The error bars in (b) show the standard deviation of four random realizations.

slope at $\epsilon^* = 0.1$ is selected for all other cases.

The results for regular hexagonal structures are presented in Fig. 3.17(a). The slope of the hardening-density relation is indicated next to each curve. The solid line is for the regular hexagonal structure in tension for small deformations. The slope for small deformations is 2.96 which is close to the analytical value of 3. Obviously, at small deformations the results are the same for tension and compression. The curve in tension with finite deformations results in a slightly lower slope of 2.76, while in compression (with finite deformations) the slope is 3.02, which is very close to the theoretical value. Clearly, the reduced slope in tension is due to geometric hardening which enhances the hardening capacity predominantly at the lower relative densities.

For Voronois with linear strain hardening, the scaling in tension deviates considerably from the theoretical scaling of honeycomb structures (see Fig. 3.17(b)). A slope of 2.78 is obtained under small deformation conditions while under finite deformation conditions the slope is 2.4. In regular hexagons yielding of all the triple points occurs simultaneously due to the symmetry of the structure. In random Voronois, however, progressive and random yielding of triple points leads to a gradual decrease in tangent stiffness (see Figs. 3.10 and 3.11) resulting in extra non-linearity during the elastic-plastic transition. This is believed to be the reason for the departure of the slope in Fig. 3.17(b) for small deformations. The effect of finite geometry re-

duces the slope even further to 2.4. Under compression the stress-strain curve forms a peak followed by a valley due to the formation of a deformation band. Hence, an appropriate definition of the plastic modulus is not possible in compression.

Power law hardening

Scaling of the elastic modulus and the plastic collapse strength (yield strength) for *perfect plasticity* is well established both in theory and through experiments. In this section, an attempt is made to find the scaling of the overall strain hardening exponent for *power law hardening* materials to completely characterize the elastic-plastic cellular material. The strain hardening behaviour of the solid material is given by Eq. 2.11. If the same form of the relationship is assumed for the cellular material under tension, we have

$$\sigma^* = \sigma^*_{\mathrm{pl}} \left(1 + \frac{E^*}{\sigma^*_{\mathrm{pl}}} \epsilon^*_p \right)^{N^*}, \quad \epsilon^* > \epsilon^*_{\mathrm{pl}}, \tag{3.11}$$

where σ^*_{pl} is the yield stress (in tension), E^* is the elastic modulus and $\epsilon^*_{\mathrm{pl}} = \sigma^*_{\mathrm{pl}}/E^*$ of the cellular structure. If the accumulated strain after yielding is $\epsilon^*_{\mathrm{p}} = \epsilon^* - \epsilon^*_{\mathrm{pl}}$, we can write

$$\frac{\sigma^*}{\sigma^*_{\mathrm{pl}}} = \left(\frac{\epsilon^*}{\epsilon^*_{\mathrm{pl}}} \right)^{N^*}, \quad \epsilon^* > \epsilon^*_{\mathrm{pl}}. \tag{3.12}$$

First σ^*_{pl} and ϵ^*_{pl} are obtained from the numerical results by identifying the point at which the stress-strain curve starts to deviate from linearity. Then, the above relation is fitted to the simulation data to get N^*. It should be noted that Eq. 3.11 describes a discontinuity in the slope at σ^*_{pl}, whereas the stress-strain curves numerically obtained always have a smooth transition in slope from the elastic to the plastic regime. The early transition zone in the stress-strain curve with a high degree of non-linearity is difficult to fit to the above equation. This leads to a certain degree of loss in accuracy during the fitting procedure. Another source of inaccuracy arises due to the geometric hardening for low relative density structures, due to which it is hard to choose a single representative strain range common to all relative densities. Hence, the strain range over which the fits are obtained is manually chosen for different relative densities which varies from 0.02 (low ρ^*/ρ_{s}) to 0.08 (high ρ^*/ρ_{s}).

Fig. 3.6(b) shows the stress-strain curves of regular hexagonal honeycombs. In this figure, the yield stress of the solid material is kept constant at 150 MPa, but the hardening exponent N_{s} is varied. Fig. 3.18(a) shows the overall hardening exponent N^* as a function of relative density for different N_{s}. For small deformation conditions, the material's hardening exponent has been recovered for the unit cell and is independent of the relative density as expected (Fig. 3.18(a)). Some error in the

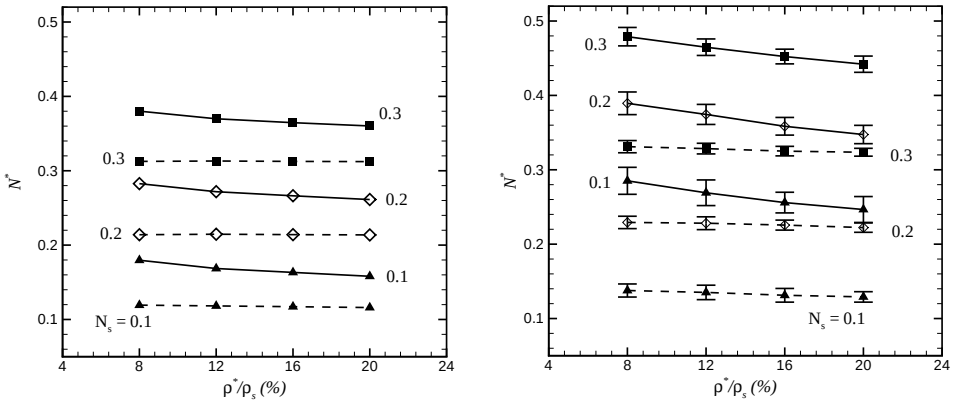

Figure 3.18: N^* versus relative density for regular hexagonal and Voronoi honeycombs plotted in figure (a) and (b) respectively. Error bars in (b) show the standard deviation over four random realizations. The dashed lines represent the fixed geometry while the solid lines are for updated geometry.

fitted N^* values occurs due to the non-linearity introduced because of the spreading of plasticity across the strut thickness and along the strut length, leading to minor inaccuracies in the fitting procedure as mentioned above. Similar curves for fixed geometry conditions were also produced for σ_Y = 50, 100, 200, 250 and 300 MPa showing that the hardening exponent is identical to that of the solid material and is independent of the yield stress and relative density for small deformations. However, when the finite deformation effects are included, the regular hexagon's hardening exponent increases and is found to depend on N_s, $\varepsilon_Y = \sigma_Y/E$ and relative density (ρ^*/ρ_s). The effect of the density on N^* for both regular hexagons and Voronois can be clearly seen in Fig. 3.18. As the relative density decreases, N^* increases.

For Voronoi structures, the difference between N^* and N_s under small deformation conditions is larger compared to hexagonal structure (see Fig. 3.18(b)). The progressive random yielding of the strut volume in the Voronoi structure (see Fig. 3.11) is believed to contribute to this extra hardening. For the finite deformation conditions, shown by the dotted line in Fig. 3.18(b), the Voronoi structures display an increased overall hardening exponent compared to the solid material. For low relative densities it can be a factor 1.6 to 3 larger. In addition, the geometric hardening contribution in the random structures can be clearly seen to be much larger than in the regular hexagonal structures.

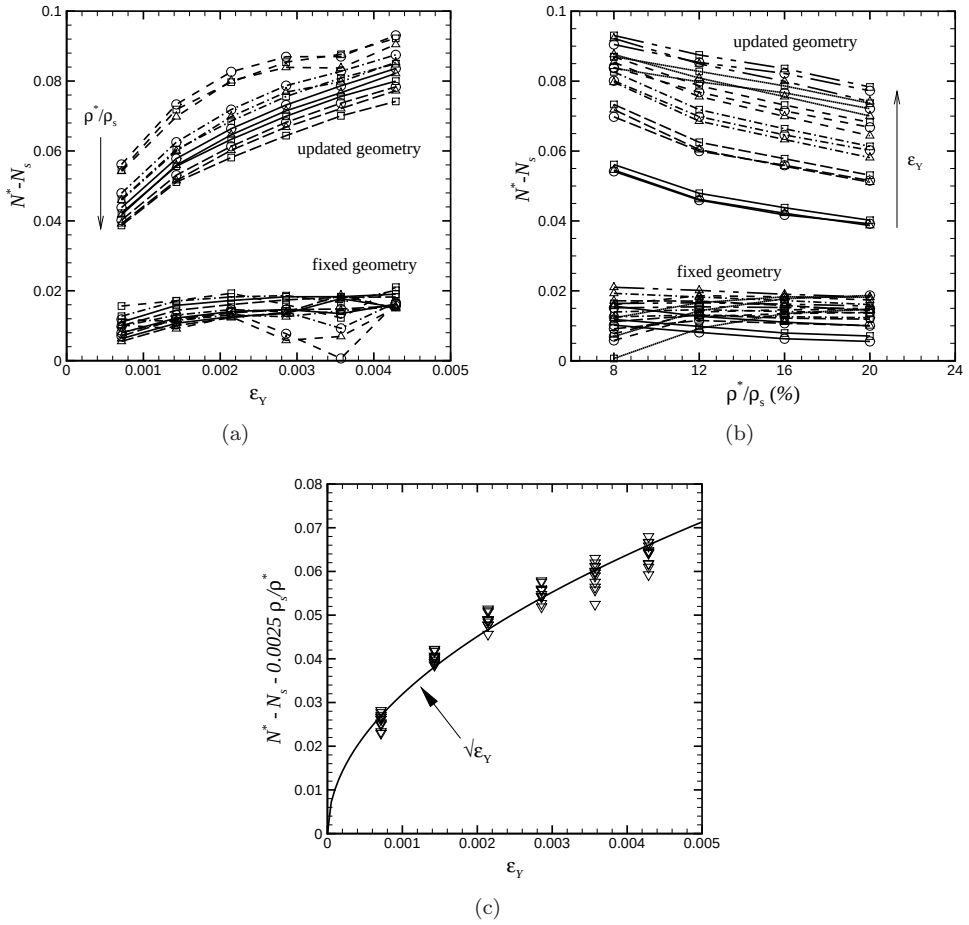

Figure 3.19: Effect of the yield strain on the strain hardening exponent of regular hexagonal honeycombs. In figures (a) and (b) the symbols △, ▫ and ○ represent N_s = 0.1, 0.2 and 0.3 respectively.

Relation between N^* and N_s

Using small deformation theory, Marchi and Mortensen (2001) have shown that the strain hardening exponent of the open-cell foam N^* is equal to that of the solid material N_s and is independent of density. Since this model is intended for small deformations or small overall strains ϵ^*, the geometric hardening discussed in section 3.2.3 is neglected. We find that due to strut orientation and gradual plastification, the hardening exponent of the foam is much larger than that of the solid material

for both the regular hexagons as well as for the random Voronois (Fig. 3.18). After a careful examination of the various dependencies observed so far, a general relationship of the form

$$N^* \propto N_s + N_g\,(N_s,\ \rho^*/\rho_s,\ \varepsilon_Y) \tag{3.13}$$

can be expected, where the function N_g accounts for the additional contribution of geometric hardening to the overall hardening. Figs. 3.19(a) and 3.19(b) show the influence of yield strain and relative density on N_g respectively. Clearly, there is no dependence of N_g on either the yield strain or the relative density at small deformation conditions. In contrast, clear stratification of the curves for different ε_Y and relative density can be observed at finite deformations. We have observed in our simulations that the geometric hardening has a pronounced effect at low relative densities compared to the higher ones, suggesting an inverse relationship on relative density. For a low solid yield stress/strain, plastic deformation spreads more along the strut length by the yielding of outer fibers. As the yield strain is increased, plastic yielding will be delayed. The further the fibers are placed from the triple point, the greater the difficulty in attaining the yield strain since the curvature decreases with the distance from the triple point. The effect is to restrict the plastic zone size and with a smaller plastic zone behaving more like a hinge, reorientation of the strut leads to enhanced geometric hardening N_g. There is also a trend to increase the geometric hardening N_g with N_s (see Figs. 3.19(a) and 3.19(b)). However, this contribution is very small compared to the contribution from either the relative density or the yield strain. Finally, the simulation data is found to be well described by

$$N^* = N_s + a_1 \frac{1}{(\rho^*/\rho_s)} + a_2 \sqrt{\varepsilon_Y}, \tag{3.14}$$

with $a_1 = 0.0025$ and $a_2 = 1.0$ (see Fig. 3.19(c)). Although the coefficient a_1 appears to be small, the contribution of the relative density term is about 10% to 32% of the N_s for the range of densities covered here. Since the contribution of N_s to N_g is very small compared to the other contributions, it is neglected.

3.2.5 The effect of heat treatment

The mechanical properties of many engineering materials can be altered by a heat treatment which produces a change in the microstructure of the solid. The yield stress, the hardening exponent and the fracture stress are among those properties which are usually affected by the heat treatment. The cellular microstructure (architecture) remains unaffected, but any change in the solid material properties will be reflected in the foam properties (Lehmhus and Banhart, 2003; Krishna et al., 2007; Amsterdam et al., 2008b). In this section we study the effect of heat treatment

on the hardening behaviour of the two-dimensional honeycombs and a qualitative comparison of the trends is made with the experiments. Note that care should be taken in relating the results of two-dimensional calculations to experimental data on real three-dimensional foams. Real foams have cells of different morphology and feature an additional out-of-plane constraint on the deformation of individual cells. A comparison can therefore be qualitative at most.

Here we take typical properties for an annealed aluminium alloy ($\sigma_{\mathrm{Y}} = 41$ MPa, $N_{\mathrm{s}} = 0.17$ and $\sigma_{\mathrm{F}} = 105$ MPa, referred to as AN) and a tempered aluminium allow ($\sigma_{\mathrm{Y}} = 191$ MPa, $N_{\mathrm{s}} = 0.05$ and $\sigma_{\mathrm{F}} = 220$ MPa, referred to as T6), see also Amsterdam et al. (2008b). The relative density is taken to be 12% for both the regular hexagons and random Voronoi structures.

In Fig. 3.21(a) it can be seen that the tempered hexagonal honeycomb is stronger compared to the annealed structure. Since the hardening exponent of T6 is low ($N_{\mathrm{s}} = 0.05$), the stress profile near the triple point, shown in Fig. 3.21(b), closely resembles the elastic-perfectly-plastic results of Fig. 3.2(b). However, the elastic-plastic boundary development, shown in Fig. 3.21(c), is considerably different from the zero hardening case (Fig. 3.2(c)). It can be seen that the plastic hinge formed in a T6 hexagonal structure is more diffused compared to the situation when there is no hardening. At the same overall strain level, the annealed hexagons shows a highly diffused and larger plastic zone compared to T6 which is due to the fact that the $\sigma_{\mathrm{Y,AN}}$ is lower and the $N_{\mathrm{s,AN}}$ is higher. A lower yield stress results in early yielding and the increased strain hardening accelerates the stress increase in adjacent regions along the strut.

Next we study how the overall hardening capacity N^* is affected by the heat treatment for a range of relative densities (Fig. 3.22). One of the striking observations in Fig. 3.22 is that the effect of geometric hardening is much higher in the random structures compared to the regular ones. For the random Voronoi structures at low relative densities, the overall hardening N^* increases by a factor of 4 compared to N_{s} in the T6 hardened material, while it increases by a factor of 1.5 to 2 in the annealed material. Here, the large yield stress of the tempered material plays an important role (see Fig. 3.19). As a consequence, the overall hardening exponents are of comparable magnitude while the base material hardening exponents differ by a factor of 3. A similar trend has been observed in the experimental investigation by Amsterdam et al. (2008b).

A view on damage initiation After the initiation of yielding, the strain hardening of the material increases the stresses in the fibers. When the stress at the outer fibers of a strut reaches the fracture stress, then usually the fracture process in the strut is initiated. Although, the scope of this chapter is not to study the explicit

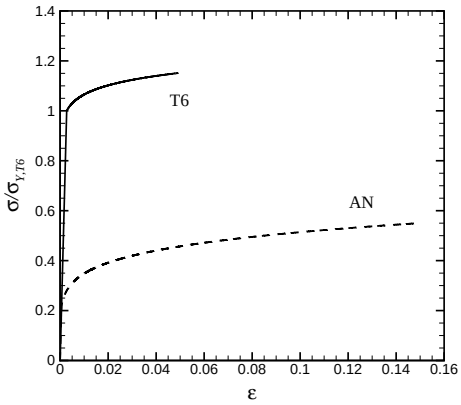

Figure 3.20: Typical stress-strain curves of bulk Aluminum alloy 6101 in T6 tempered (solid lines) and annealed (dashed lines) shown up to fracture stress.

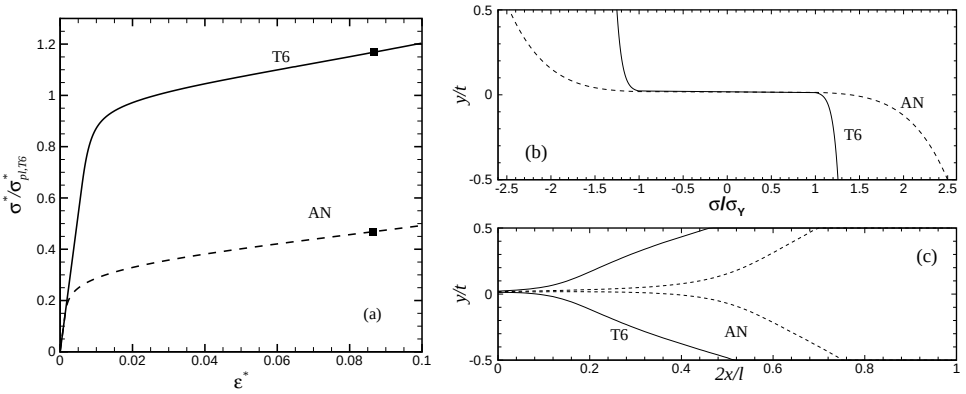

Figure 3.21: Behaviour of unit cells with solid material in annealed (dashed line) and T6-tempered (solid lines) conditions. The stress profile in (b) is plotted for the triple point and the elastic-plastic boundaries in (c) are plotted along the inclined strut of the unit cell. These profiles are plotted at an overall strain indicated by the labeled point in (a).

evolution of damage, the peak stress for small samples can be estimated from the early initiation of damage in random struts (see Amsterdam et al. (2008b)). Then, the total number of struts that have exceeded the fracture limit can provide an indirect estimate of the damage accumulation in the structure. A damage indicator D is defined as the number of the critical struts (struts in which at least one of the outer fibers has exceeded the fracture stress) divided by the total number of the struts. It

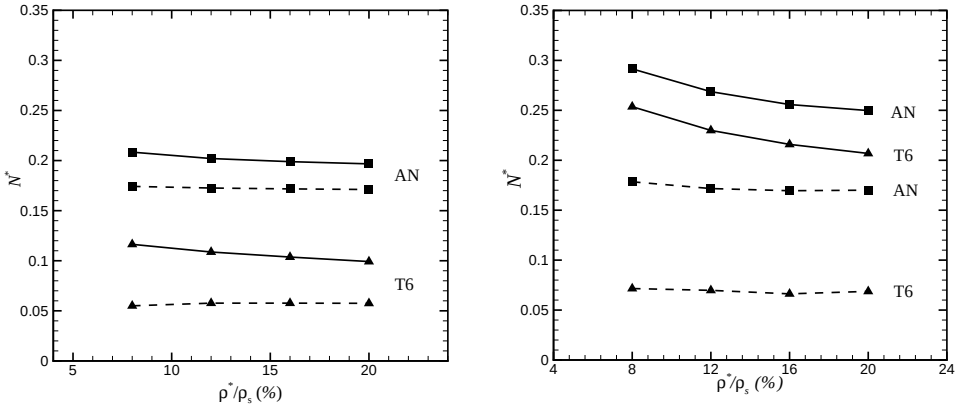

Figure 3.22: Scaling of hardening exponent with relative density for (a) a regular hexagonal structure and (b) a Voronoi structure. The solid line is for updated geometry and the dashed line is for fixed geometry conditions.

should be noted that at large overall strains and for a rapidly hardening material, this damage indicator can only be seen as a rough estimate since no unloading of damaging struts is accounted for.

Fig. 3.23(a) presents the stress-strain curves for different relative densities. Note that the stress in this figure is normalized with $\sigma_{Y,T6}$. These curves clearly show that the T6-tempered foams are much stronger than the annealed samples. Figure 3.23(b) shows the damage curves for the cases shown in Fig. 3.23(a). Nearly at $D = 0.25$, all the curves in Fig. 3.23(b) exhibit a saddle point, which indicates that the fracture stress has been reached in many struts and that for additional strain the damage rate will decrease. This D value has been chosen as the critical damage level at which the peak fracture stress (σ_f^*) and the peak fracture strain (ϵ_f^*) has been reached. It can be observed that the initiation of damage occurs sooner (i.e. at small strains) for the T6 structures compared to the annealed specimens for all the relative densities studied. Also the damage accumulation rate, given by the slope of the curve in Fig 3.23(b), is higher in T6 than in AN. These observations are in close agreement with the experimental damage curves based on resistance measurements carried out by Amsterdam et al. (2008b).

In Fig. 3.24, we plot the peak stresses and strains (indicated by the symbols in Fig. 3.23(a)) against the relative density for Voronois under the tempered (T6) and annealed (AN) conditions. The peak fracture stress σ_f^* scales with a power of 1.85 for T6 and 1.55 for annealed Voronois. The scaling of the peak strain exhibits

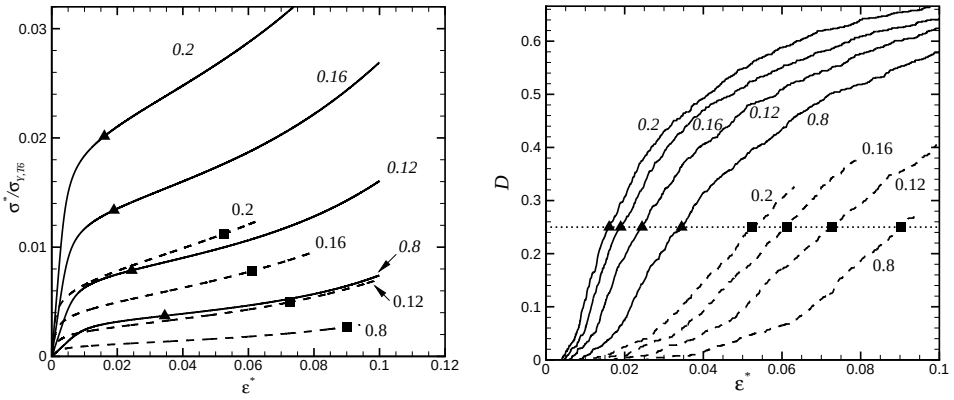

Figure 3.23: (a) Stress-strain curves of Voronois under T6 (solid) and AN (dashed) conditions. (b) Damage indicator D (see the text) versus strain for different relative densities corresponding to the curves shown in figure (a). The labels in the curves indicate the relative density. The failure point defined by $D = 0.25$ is indicated on each of the curves of (a) by triangles and squares for T6 and AN conditions respectively.

exponents of -0.59 and -0.83 for the T6 and annealed Voronois, respectively. A similar strong power law dependence of the peak stress has been reported in the experiments performed by Amsterdam et al. (2008b). On the other hand, the experiments show only a decreasing peak strain with increasing density for low densities. At large densities the peak strain is found more-or-less independent of densities suggesting a different mechanism that cannot be picked up by the current two-dimensional model.

3.3 Summary and conclusions

Plastic deformation in regular and random honeycombs has been studied using a finite element model. Accounting for the gradual plastification of the cross section, the development of plastic zones near the triple points in regular hexagonal structures has been analysed in detail. The strain hardening of the solid material determines the plastic zone size, shape and the overall stress-strain response. In bending-dominated structures, the plastic hinge size increases with increasing hardening capacity (either linear or power law hardening), covering most of the strut length for high strain hardening solid materials. For structures under uniaxial straining, axial deformation

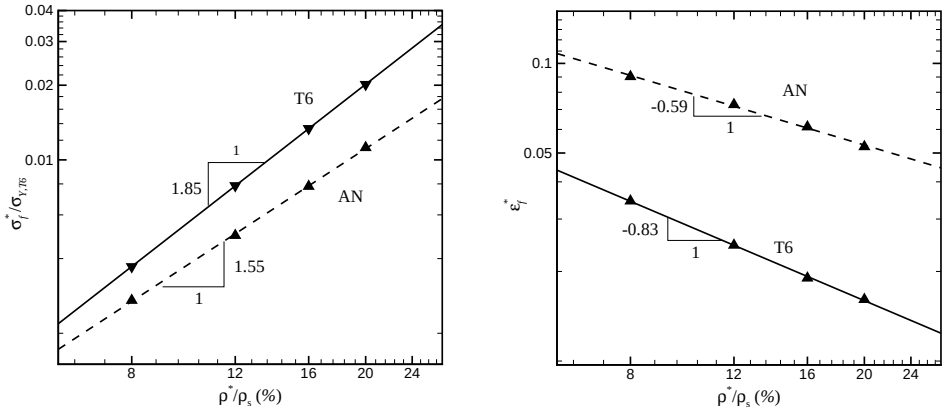

Figure 3.24: Scaling of the fracture stress (figure a) and fracture strain (figure b).

of the strut is the dominant deformation mode. Cellular materials are much stronger under uniaxial straining compared to uniaxial tension. On the other hand, hexagonal structures with non-uniform cross section are stronger and stiffer in uniaxial tension but are weaker in uniaxial straining. In random Voronoi structures subjected to tension or compression, although the random triple point yielding is only slightly influenced by strain hardening, the volume of the material that becomes plastic is greatly affected. In compression, strain localization is hindered when the hardening capacity of the solid is increased.

In cellular structures, a second mechanism of hardening exists due to the internal geometry changes and is profound at low relative densities. The material hardening and geometric hardening combinedly produce a synergistic effect at large strains. At small strains, the scaling of the in-plane plastic tangent modulus is close to the analytical scaling for hexagonal honeycombs. At finite strains, the it deviates from the analytical predictions due to the geometric hardening. This departure is much higher in random Voronois.

For power law hardening, the overall hardening is found to be a sum of the solid's intrinsic material hardening and geometric hardening. The geometric hardening is a strong function of the relative density and the yield strain, but is a weak function of the solid material hardening. A closed-form expression has been proposed that captures these dependencies.

Simulations with the annealed and tempered material parameters clearly show how the combination of the different material properties affect the mechanical be-

haviour of the cellular structure. The microstructural origin of the different hardening and damage mechanisms have been identified and related to the plasticity development inside the struts. A strong scaling for the uncoupled peak stress and peak strain has been found for both the heat treatment conditions and the trends observed are found to be in close agreement with the experiments.

Based on: Mangipudi, K.R. and Onck P.R. – *"Multiscale modelling of damage and failure in two-dimensional metallic foams",* J. Mech. Phys. Solids, Vol. 59, No. 7, pp. 1437-1461, 2011.

Chapter 4

Damage and failure in metal foams: material and architectural aspects

There are forces in life working for you and against you. One must distinguish the beneficial forces from the malevolent ones and choose correctly between them.

President Dr. A.P.J. Abdul Kalam

The fracture strength of metal foams depends sensitively on the properties of the constituent material as well as the cellular architecture. A change in microscopic properties carries over to the macroscopic scale through an alteration of the mesoscopic damage and fracture mechanisms. In this chapter, we study these dependencies using a modelling framework that takes all these ingredients into account. We have developed a micromechanical model based on a discrete Voronoi representation of cellular metals that incorporates power-law strain hardening and damage development of the cell wall material. The influence of the relative density and material strain hardening on the cell wall damage behaviour and overall fracture response is analysed in detail. The effect of the cellular architecture is studied by varying the cell shape anisotropy and structural randomness. We also simulate the effect of post-processing heat treatments on the solid material plastic and fracture properties and how this affects the overall fracture profile and damage development. Finally, all material and architectural effects are summarized in a strength versus ductility graph, identifying trends for improved design of metallic foams.

4.1 Introduction

Metal foams require a good combination of strength and ductility for their use in engineering applications. However, despite being very ductile under compression, most commercially available foams are very brittle under tension with damage onset strains of less than a percent. Indeed, in the core shear failure of sandwich panels, Harte et al. (1999) have identified that the failure of sandwich panels occurs due to damage development from tensile microcracks in the core. However, in contrast to the compressive failure modes, the mechanisms that lead to tensile failure are less well understood.

The primary goal of this chapter is to conduct a detailed investigation of the process of uniaxial tensile deformation, damage initiation and accumulation in ductile cellular solids, ultimately leading to failure. The effect of material properties, cellular architecture and sample size on the mesoscopic and macroscopic tensile behaviour will be studied systematically. For this purpose, we will use the model presented in section 2.3.

The chapter is organized into two parts. In the first part, we study the role of the constituent material, while in the second part we will explore the architectural aspects. The general mechanisms of the tensile deformation and damage processes in Voronoi structures will be analysed in section 4.2. The effect of the material parameters, cellular architecture and sample size on the tensile fracture will be presented, followed by a discussion in section 4.5 and conclusions in section 4.6.

4.2 Method

Finite-sized Voronoi structures of width W/d and height H/d (while d being the average cell size) have been used in this study; a typical network is shown in Fig. 4.1. Unless otherwise stated, all the Voronoi structures are generated with an overall regularity parameter $\delta = 0.9$ (Zhu et al., 2001b). Anisotropic structures are generated by applying an affine scaling transformation on the co-ordinates of the triple points of an isotropic Voronoi structure. A converged mesh size of 40 equal-sized beam elements per strut is used. The struts have a uniform cross section and all struts have the same thickness $t = S\bar{\rho}/l_{\mathrm{tst}}$, where S is the strut volume per unit out-of-plane thickness, $\bar{\rho} = \rho^*/\rho_{\mathrm{s}}$ is the relative density (ρ^* is the density of the foam and ρ_{s} is the density of the strut material) and l_{tst} is the sum of all strut lengths. Twenty integration points (fibers) across the thickness are used for each beam element to integrate the element stiffness matrix when it is inelastic.

Fig. 4.1 shows the applied displacement boundary conditions, consistent with loading through perfectly bonded rigid face-sheets. The macroscopic strain ϵ^* is

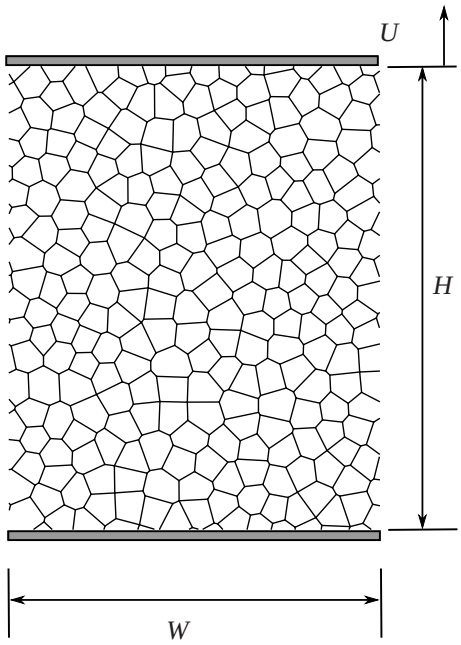

Figure 4.1: Voronoi structure ($\delta = 0.9$) with the applied boundary conditions.

U/H, where U is the applied vertical displacement and H is the initial height of the sample. The macroscopic stress denoted by σ^* is given by the total force F at the top boundary divided by the cross sectional area of the sample Wb, with the out-of-plane thickness b taken to be unity. In most cases, we normalize the macroscopic stress with the plastic collapse stress of a regular hexagonal honeycomb with strut thickness t and strut length l (Gibson and Ashby, 1997)

$$\sigma^*_{\rm pl} = \frac{2}{3}\,\sigma_{\rm Y}\left(\frac{t}{l}\right)^2 = \frac{1}{2}\,\sigma_{\rm Y}\left(\frac{\rho^*}{\rho_{\rm s}}\right)^2. \tag{4.1}$$

Averaging of the macroscopic properties is carried out over four random realizations and the standard deviation is shown with error bars in the relevant figures in the following sections. For convenience, we define a damage variable D as the ratio of the total fracture energy dissipated in the damaging fibers in a strut to the input fracture energy $\Gamma_0 A$.

In all the following calculations, Young's modulus E of the solid material is taken to be 70 GPa, yield stress $\sigma_{\rm Y} = 41$ MPa, the critical fracture strain $\varepsilon_{\rm F} = 0.08$ and $2\Gamma_0/(\sigma_{\rm Y}^2\, l_0) = 5$, unless specified otherwise. The reference length l_0 for the random

structures is given by the cell wall length of a regular hexagonal cell having the same average Voronoi cell volume per unit out-of-plane-thickness.

4.3 Part I: Constituent material aspects

4.3.1 Damage mechanisms

Damage development in a regular hexagonal structure

We consider a unit cell of a perfectly regular hexagonal honeycomb shown in the inset of Fig. 4.2(a) with the indicated symmetry boundary conditions. Power-law strain hardening is used with $N_s = 0.05$ and the relative density is 0.058 ($t/l = 0.05$). The macroscopic stress and macroscopic strain are calculated as $\sigma^* = 2F/(\sqrt{3}l)$ and $\epsilon^* = 4U/(3l)$, respectively, where U is the applied vertical displacement (see the inset of Fig. 4.2(a)) and F is the corresponding reaction force. The macroscopic

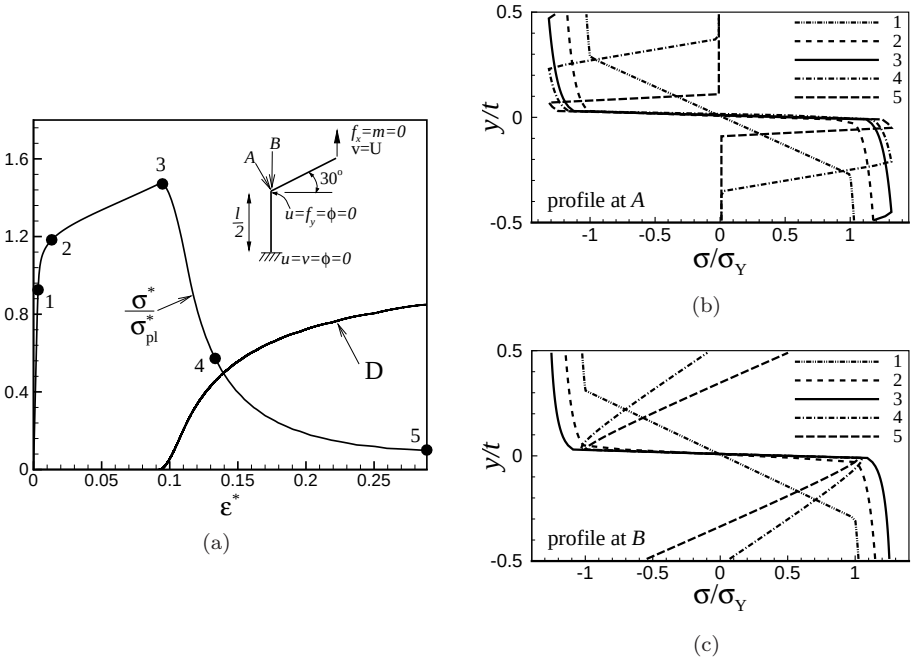

Figure 4.2: Regular hexagonal structure: (a) stress-strain curve and the damage variable D in the inclined strut, (b) and (c) are the stress profiles at A and B in the inclined member of the regular hexagonal unit cell shown in the inset of (a). The stress profiles in (b) and (c) correspond to the loading instances 1 to 5 in (a).

stress-strain curve is presented in Fig. 4.2(a), while Fig. 4.2(b) and 4.2(c) show the evolution of the stress profile inside the strut at points A and B, respectively, in the inclined member near the triple junction. Due to the symmetry exhibited by perfect regular hexagonal structures with a uniform strut cross section, all the triple points yield (and fail) simultaneously, in contrast to the triple points in random structures, which yield over a range of macroscopic strain (Mangipudi et al., 2010). The stress profiles at A and B at instant '1' (see Fig. 4.2(a)) show yielding of the top and the bottom fibers, reaching (almost) full-section yielding at '2'. With continued straining, the critical fracture stress σ_{F} is reached in the inclined member at a position next to the triple point (point A in the inset of Fig. 4.2(a) slightly before the instant '3'). The outer fibers, which have reached the critical stress, will begin to damage and the stress in these fibers will reduce. During this early phase of damage, the effective stiffness of the element decreases but can still remain positive due to the large number of intact fibers. Thus, the overall stress-strain curve need not show a negative slope immediately after the damage initiation. When more fibers reach the critical fracture stress and begin to soften, a negative stiffness at the damage location (point A) develops and softening will be noticed in the macroscopic stress-strain behaviour. Softening due to damage near the triple junction at point A (see Fig. 4.2(b)) leads to elastic unloading from a plastic state in the adjacent locations, for example, at point B as shown in Fig. 4.2(c). This can be clearly seen by comparing Figs. 4.2(b) and 4.2(c) for instances 3, 4 and 5.

Damage initiation and accumulation in random structures

In this section, we study Voronoi structures of 12×16 cells ($W \times H$), see Fig. 4.1. A typical overall stress-strain curve for a relative density of 0.24 and hardening exponent of 0.05 is shown in Fig. 4.3. Figs. 4.4 and 4.5 show the associated strain and stress maps and incremental strain maps, respectively. Four distinct regimes can be identified: (I) a linear regime, (II) a nonlinear hardening regime, (III) a regime of competition and, (IV) a softening regime (after the peak). The linear elastic regime (I) is mainly due to homogeneous elastic deformation with some microscopic plasticity in the struts near the triple junctions. The forces and moments in the struts increase monotonically with little gross deformation. The local stresses and strains are close to their respective macroscopic values (see strain and stress maps in Fig. 4.4, corresponding to point A in the stress-strain curve of Fig. 4.3). After the initial elastic deformation, yielding of struts near the strut junctions (triple points) occurs in which the outer fibers reach the yield stress; this instant is denoted by point A on the stress-strain curve with the first yielding location being identified by the red dot in Fig. 4.4(A). Since most of the structure (strut volume) is still elastic, the overall modulus of the structure remains close to the elastic modulus. With increasing ap-

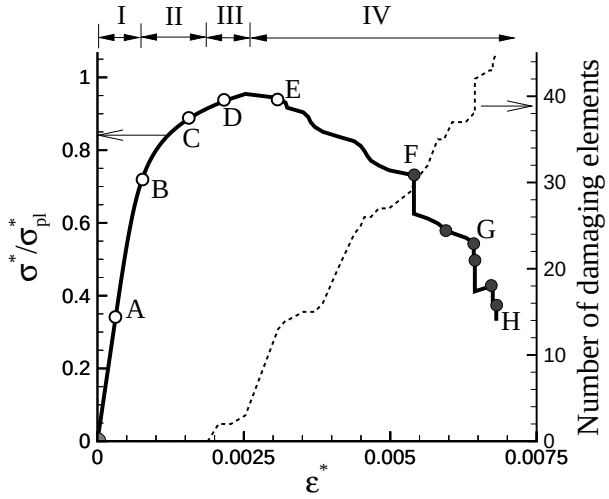

Figure 4.3: Typical stress-strain curve obtained for a Voronoi structure under uniaxial tension. Removal of damaged struts occurred at strains corresponding to the black filled symbols in the softening branch.

plied strain, more struts yield at triple points and yielding inside the struts spreads across the strut thickness. As the cell wall material can strain harden, stresses in the neighborhood of the triple points increase and develop an extended plastic zone in the strut (see Fig. 4.4(D) where the plastic portions of the struts are shown in white). For high strain hardening materials, this plastic zone may cover the entire length of some struts depending on the relative density and the local loading of the strut (Mangipudi et al., 2010).

With most of the triple points yielding and hardening, the stress-strain curve enters the second regime (II) with a nonlinear stress-strain response. This phase of deformation is associated with mechanisms that determine the damage initiation and thus the foam strength. The strains still remain distributed through a large volume of the structure (see the strain map D in Fig. 4.4), showing no strong strain localization as usually observed in compression. However, the incremental strain map in Fig. 4.5(b) clearly shows that there is a preferential growth of plastic strains in certain locations and bands of the structure. At any instant, the strains in these regions are much larger than the current applied macroscopic strain. These regions will become the prospective sites for the damage initiation. While the strains show a preferential growth, the apparently small inhomogeneities in the local stress distribution tend to decrease and the stress state becomes slightly more uniform as can be seen from the figures (A) and (D) in Fig 4.4.

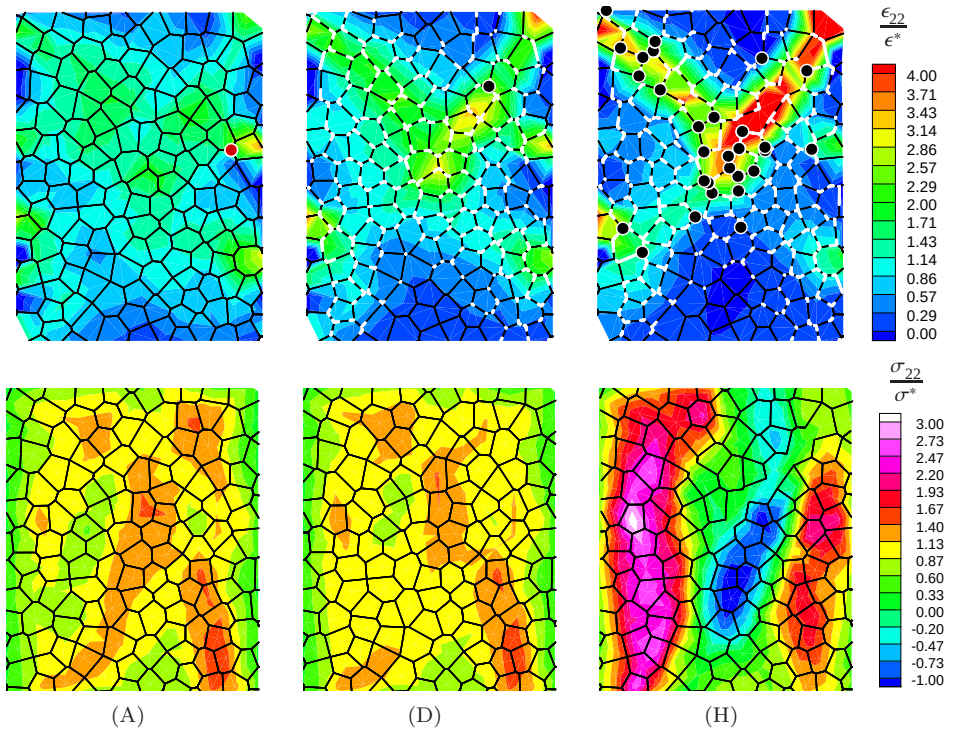

Figure 4.4: Normalized strain and stress maps (top and bottom rows, respectively) associated with Fig. 4.3. The plastic portions of the struts are marked in white. The first yield (red dot in A) and damage locations (black dots in D and H) are indicated on the strain maps. White thick lines on H are the removed struts.

When the fiber stress in a strut reaches the critical fracture stress of the cell wall material, damage is initiated in one of the high-strain regions (see the black dot in Fig. 4.4(D) and the damage curve in Fig. 4.3). This marks the beginning of the third regime (III) which is crucial in determining the ultimate strength of the cellular material and involves various mutually competing mechanisms. Despite the initiation of damage, the structure continues to load with further straining as other parts of the structure can still carry the redistributed load due to strain hardening. Soon a few more struts reach the failure stress in these high-strain regions, enhancing the overall softening rate. When the overall softening rate equals the overall hardening rate, a peak in the stress-strain curve is attained (before points D and E in Fig. 4.3).

The fourth regime (IV), counted from the peak until complete failure, is associated with the coalescence of small "cracks" (i.e. the fractured struts) leading to the ultimate failure of the structure. Beyond point E, the number of damaging struts

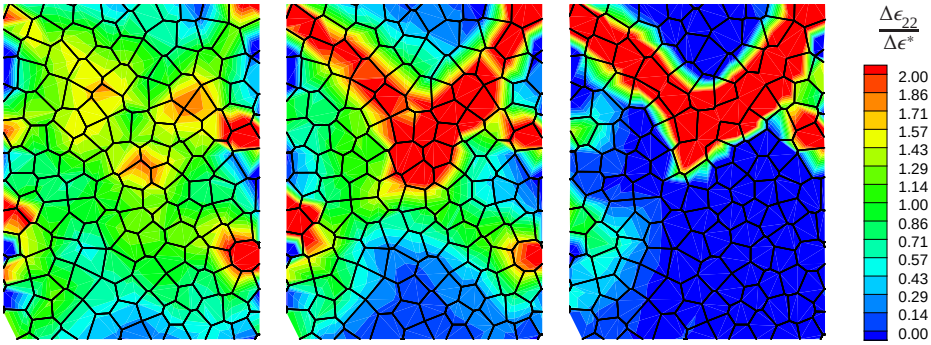

(a) up to A (b) B to C (c) G to H

Figure 4.5: Normalized incremental strain maps. The local increments in strain $\Delta\epsilon_{22}$ are normalized with the applied macroscopic strain $\Delta\epsilon^*$ in each interval.

increases gradually during softening (see Fig. 4.3), and they appear in the regions of large prior plastic deformation (see the black dots in Fig. 4.4(H)). Once the element has reached its critical damage level (i.e. 85% of the total available fracture energy has been dissipated), the strut will be removed. These removed struts are indicated by dots on the softening branch in Fig. 4.3 and by thick white lines in Fig. 4.4(H). Strain localization due to damage is clearly manifested in Fig. 4.5(c). The incremental strains are highly localized at the active damage locations, while other regions experience either relatively low strain increments or may undergo strain unloading. Meanwhile, the damage process is completed in some struts forming small cracks of two or three cells, which later coalesce into a larger crack as shown in strain map (H) of Fig. 4.4 and in Fig. 4.5(c). During the progressive damage, stresses in the structure strongly redistribute to the undamaged parts of the structure (see the stress maps in Fig. 4.4) and will lead to damage initiation in these regions as well.

4.3.2 The effect of relative density and material strain hardening

The increase in elastic modulus and yield strength with relative density is well known (Gibson and Ashby, 1997). The relationship between the relative density and the overall hardening of the structure has been studied by Mangipudi et al. (2010). In this chapter, we focus on the role of relative density and strain hardening on the macroscopic fracture properties and mechanisms. This is explored by keeping the Young's modulus E, the yield strength σ_{Y}, the fracture strain ε_{F} and the specific fracture energy Γ_0 constant and only the solid material's hardening exponent N_{s} and relative density ρ^*/ρ_{s} will be varied. It is worth noting that a constant critical fracture

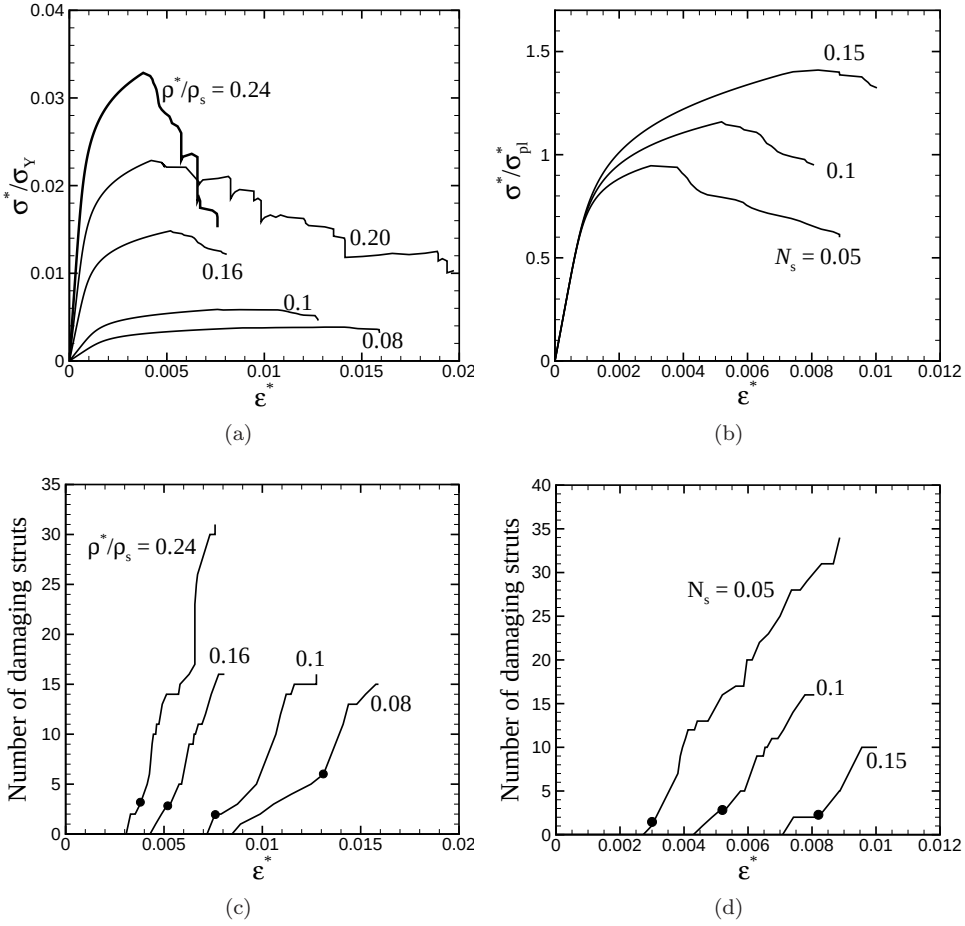

Figure 4.6: Effect of relative density and strain hardening. Macroscopic stress-strain behaviour is shown for fixed $N_s = 0.1$ in (a) and for a fixed $\overline{\rho} = 0.16$ in (b). The corresponding damage accumulation plots are shown in (c) and (d), respectively. The symbols on the damage plots indicate the peak strain.

strain ε_F will lead to different critical fracture stresses σ_F for different values of N_s. Fig. 4.6(a) shows the effect of relative density on the failure behaviour for $N_s = 0.1$. It can be clearly observed that the peak stress increases with relative density, whereas the peak strain (i.e. the strain at the peak stress) decreases. Fig. 4.6(c) shows the accumulation of damage in the structures as a function of the relative density. Clearly, the damage initiation occurs at smaller strains with increasing relative density and the rate of internal damage, i.e. the slope of the curves in Fig. 4.6(c), is also enhanced.

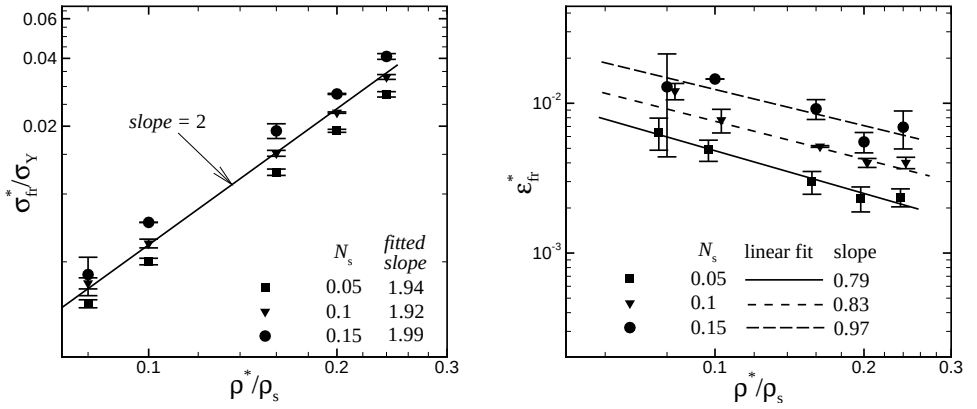

Figure 4.7: Effect of strain hardening on the scaling of (a) peak stress and (b) peak strain. For clarity, the data for $N_s = 0.05$ and 0.1 in figure (b) are shifted to the left and right, respectively, by a horizontal offset of 0.003.

The effect of strain hardening on the overall response is shown in Fig. 4.6(b). If one defines the yield stress of the structure as the proportionality limit (stress at which the response of the structure starts to deviate from linearity), it follows that the structural yield strength is invariant to the strain hardening. On the other hand, when the yield stress is taken as an offset stress (as often used), the yield strength increases with increasing strain hardening of the strut material. It can also be observed from the stress-strain curves that an increasing material hardening naturally increases the overall hardening, similar to the findings of Amsterdam et al. (2008c) and Mangipudi et al. (2010). For a given relative density and architecture, increasing the strain hardening capacity of the strut material enhances both the peak stress and peak strain (see Fig. 4.6(b)), when all other material parameters, including the critical fracture strain ε_F, are unaltered. This enhancement in peak stress and peak strain is related to the fact that the onset of damage is postponed with increasing N_s (see Fig. 4.6(d)). The rate of accumulation of damage is also slightly retarded by increasing N_s.

Fig. 4.7 shows the scaling of the peak stress and peak strain with relative density for different values of the strain hardening exponent N_s. Similar to the plastic collapse stress, the peak stress also shows a strong power law scaling with the relative density. The power law exponent is found to lie between 1.92 and 1.99, (see the legend of Fig. 4.7(a)) comparable to the exponent of 2 for the plastic collapse stress (straight line plotted in Fig. 4.7(a) for comparison). The peak strain is enhanced by the

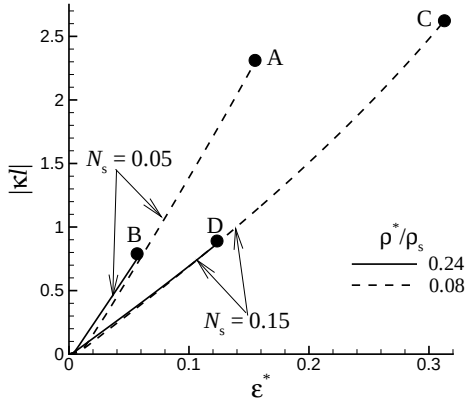

Figure 4.8: Development of curvature κ at the triple point (normalized with the strut length l) in a regular hexagonal structure as a function of the applied macroscopic strain ϵ^* plotted until failure initiation.

strain hardening for all densities as shown in Fig. 4.7(b). However, it decreases with increasing relative density. The scaling exponent has been found to increase (from -0.99 to -0.79, see Fig. 4.7(b)) with increasing N_s .

The damage behaviour in Fig. 4.7(b) is closely related to the development of plastic curvature near the strut junctions, which dictates the macroscopic strain at the initiation of failure. The triple point behaviour in a regular hexagonal structure, shown in Fig. 4.8, can provide valuable insight on this. Fig. 4.8 shows that the curvature at the triple point κ is proportional to the macroscopic strain ϵ^*, taking into account the effects of finite geometry changes, material hardening and their interactions (Mangipudi et al., 2010). The fiber strain $\varepsilon(y)$ is related to the curvature κ through $\varepsilon(y)$ (neglecting the axial strain). A critical curvature for fracture initiation is given by $\kappa_F = 2\varepsilon_F/t$, where t is the strut thickness. Increasing the relative density increases the strut thickness t and, hence, decreases the critical curvature κ_F (from A to B and C to D in Fig. 4.8) which leads to early damage initiation at low applied strains ϵ^*. This explains the negative slope of the curves in Fig. 4.7(b), the early onset of damage initiation and the enhanced rate of damage accumulation in Fig. 4.6(c).

Failure initiation in structures with different material hardening is related to the size and shape of the plastic zone near the strut junctions. For low strain hardening materials, the plastic zone is small, effectively forming a plastic hinge. Local curvatures in these hinges can quickly develop as a function of strain ϵ^* (see the curve for $N_s = 0.05$ in Fig. 4.8). On the other hand, for a high strain hardening solid material, the plastic zone spreads along the strut length which effectively distributes the cur-

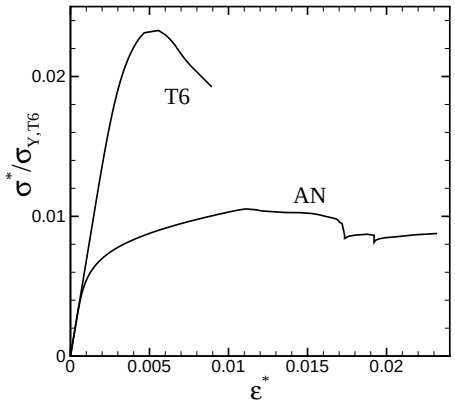

Figure 4.9: Typical stress-strain curves for different heat treatment conditions for $\overline{\rho} = 0.24$.

vature and retards the localization of curvature near the triple point. The curvature can only increase by increasing the plastic zone size and the fiber stresses along the strut. Consequently, attaining the critical curvature near the triple point requires larger overall strains and occurs at larger stresses (e.g., compare B and D or A and C in Fig. 4.8). As a result, both the peak stress and peak strain increase with N_s for a given relative density, explaining the observed response in Figs. 4.6(b), 4.6(d) and 4.7.

4.3.3 The effect of heat treatment

The effect of post-solidification heat treatment on the overall strain hardening of the structure has been studied by Mangipudi et al. (2010). Here, we study the variation in the fracture properties with heat treatment using the following material parameters: $\sigma_Y = 41$ MPa, $N_s = 0.17$, $\sigma_F = 105$ MPa (or $\varepsilon_F = 0.148$) and $2\Gamma_0 E/(\sigma_Y^2 l_0) = 5$ for an annealed material (AN) and $\sigma_Y = 191$ MPa, $N_s = 0.05$, $\sigma_F = 220$ MPa (or $\varepsilon_F = 0.046$) and $2\Gamma_0 E/(\sigma_Y^2 l_0) = 3$ for a tempered material (T6).

Fig. 4.9 shows the overall stress-strain curves of a Voronoi structure ($\rho^*/\rho_s = 0.24$) with annealed (AN) and T6 tempered (T6) strut material. A strengthening treatment like T6 hardening produces a solid material with a higher yield stress, but with a lower strain hardening exponent, compared to annealing. Annealing also usually results in an enhanced ductility. This change in the solid material properties also carries over to the overall properties of the foam structure (see Fig. 4.9). Since the difference between the yield stress and the fracture stress for the annealed case is large, the stress strain curve shows large plastic deformation. In contrast, the

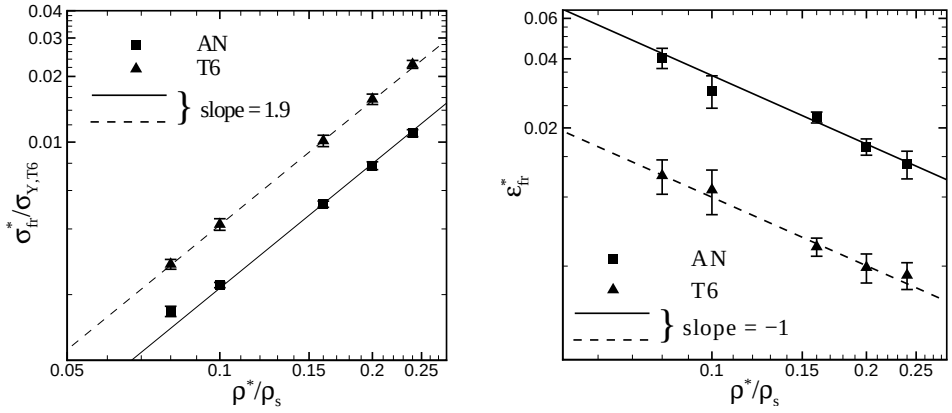

Figure 4.10: Effect of heat treatment on the fracture stress and fracture strain.

yield and fracture stresses are close for the tempered case, so that only a small non-linear plastic regime in the stress-strain curve can be found. The peak stress for the tempered structure is larger compared to the annealed one, but unloads much faster after the peak due to the lower fracture energy $\Gamma_0 A$.

Fig. 4.10(a) shows the fracture stress variation with relative density. The fracture stress of the annealed case is lower than that of the tempered condition for all the relative densities. The data for both the annealed and temper hardening conditions in Fig. 4.10(a) scale with the relative density power 1.9, a similar scaling as the yield strength. The fracture strain for the annealed case is larger than for the temper condition; both decrease with relative density with a slope equal to -1 (see Fig. 4.10(b)).

4.3.4 Influence of brittle precipitates

To model the influence of precipitates, the mechanical response of a precipitate-containing matrix is distinguished from a matrix free of precipitates. Fractography revealed that the failure of cell walls in commercial aluminium foams takes place by cleavage of brittle precipitates producing microcracks and by the subsequent ductile rupture of the matrix between microcracks (Marchi et al., 2004; Paul et al., 1999; Amsterdam et al., 2006b,c). Since the precipitates were observed to fail before the matrix, the fracture strength and toughness of a precipitate-containing matrix will be lower than a precipitate-free matrix. In our model, the above fact is accounted for through an appropriate definition of the constitutive law governing the precipitate-

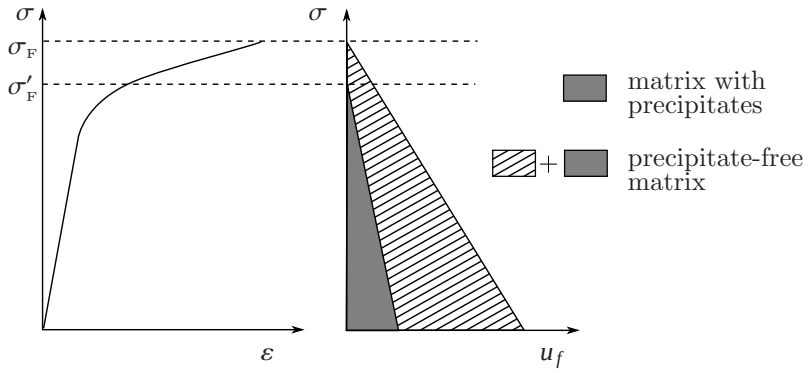

Figure 4.11: Schematic stress-strain curve of a precipitate-free matrix and the assumed stress-strain response of a matrix containing a precipitate. The shaded or hatched area on the stress-displacement relation defines the specific fracture energy.

containing beam element. The fracture stress σ'_{F} and the specific fracture energy Γ'_0 in the presence of a precipitate are chosen to be lower than the regular matrix. This is schematically illustrated in Fig. 4.11. Depending on the segregation, type and morphology of the precipitates, the local mechanical response may differ from one point to the other within the cell wall. However, for simplicity, we do not consider this variation in the following computations.

After generating structures as stated in section 4.2, beam elements have been randomly assigned to contain precipitates. These elements follow the constitutive behaviour of the matrix until the flow stress reaches σ'_{F} and then a linear stress-displacement softening law is followed with a specific fracture energy given by Γ'_0. The rest of the elements follow the precipitate-free matrix behaviour as shown schematically in Fig. 4.11. We take $\sigma'_{\mathrm{F}} = 45$ MPa and $2E\Gamma'_0/\sigma^2_{\mathrm{Y}} = 3$ for the precipitate-containing elements compared to $\sigma_{\mathrm{F}} = 67.04$ MPa and $2E\Gamma_0/\sigma^2_{\mathrm{Y}} = 15$ for the precipitate free matrix. The strain hardening exponent N_{s} is 0.1 and the relative density is 0.16. Since the influence of a precipitate is approximated as an averaged constitutive response of a matrix-precipitate combination in an element, a precipitate volume fraction cannot be appropriately defined in this approach. However, in this section, we distinguish different precipitate densities based on the percentage of precipitate-containing elements for similar-sized structures with the same mesh discretization parameters.

The existence of only about 0.5% precipitate-containing elements considerably reduces both the peak stress and peak strain in Fig. 4.12. Clearly, damage has initiated much earlier compared to a precipitate-free structure. As more and more struts contain precipitates, the peak stress and peak strain are severely knocked-

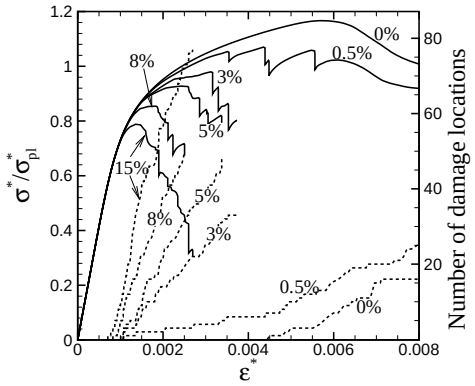

Figure 4.12: Stress-strain curves (solid lines) and internal damage accumulation (broken lines) in the presence of brittle precipitates. The labels represent the percentage of brittle struts that contain precipitates anywhere along their length.

down, almost reducing to the yield stress at 15%. The peak is reduced quickly at low percentages of brittle struts and becomes gradual at large percentages. Among the precipitate-containing structures, the damage onset strain is not very different, although a systematic reduction may be observed with an increasing percentage of brittle struts. Obviously, the increased damage accumulation rate plays an important role in the reduction of the peak stress and peak strain values. Microstructurally, we have observed different failure paths in different structures (not shown here), indicating the spatial distribution of randomly placed precipitates controls the specific fracture morphology.

4.4 Part II: Architectural aspects

4.4.1 Structural randomness

In this section, we discuss the effect of structural randomness on the fracture behaviour for different relative densities and for fixed solid material properties (E, σ_{Y}, ε_{F}, N_{s} and Γ_0), as given in the beginning of section 4.2. The hardening exponent is taken to be $N_{\mathrm{s}} = 0.05$. The regularity parameter δ is defined such that $\delta = 1$ corresponds to a regular hexagonal structure, while $\delta = 0$ corresponds to a fully random Γ-Voronoi structure (Zhu et al., 2001b). We will compare structures with $\delta = 0$, 0.4 and 0.9. Zhu et al. (2001a) have analysed the structure of random Voronoi structures and have found that with decreasing δ, the cell size distribution as well as the cell wall lengths distribution become wider and the percentage of non-hexagonal cells

increases. In Fig. 2.6, it can be observed that some of the cells are elongated with large aspect ratios and that near triangular and other skewed cell shapes are present for low δ values. Clearly, this change in the cellular architecture influences the cell level deformation. With decreasing structural regularity (from $\delta = 0.9$ to $\delta = 0$), the strain distribution becomes less homogeneous even at low macroscopic strains. To quantify this, the cell level strain distribution is shown in Fig. 4.13, where the normalized mean cell strains are plotted against the normalized cell area. The details of the calculation of the mean cell strains have been discussed in section 2.5.2. It is clear that the cell size distribution in the structure with $\delta = 0.9$ is very narrow with the mean close to the average cell size. With decreasing δ, the distribution shifts to the small cell sizes while more large cells appear. The tensile strain is more or less uniform over the (narrow) cell size range for $\delta = 0.9$. For low δ values, however, the smaller cells carry strains close to or even less than the applied macroscopic strain, while the larger cells undergo large deformation resulting in strains up to 2 to 4 times the applied strain. Also large normalized shear strains can be observed for large cell sizes.

By analysing the spatial deformation pattern at the cell scale, the same has also been observed as high strain regions covering mainly the large cells. The large cells are mostly elliptical in shape. Compared to the more equiaxed cells, these elliptical cells are more compliant and are found to be the severely deforming cells in the collapse bands in Alporas (Bastawros et al., 2000). Increasingly elliptical cells increase the angle between two cell walls at the junction and introduce a T-like junction - another morphology responsible for the *"weak"* behaviour of the cell (Bastawros et al., 2000). The system forms the damage process zone by identifying the weakest path by connecting these elliptical cells forming high strain zones. Since the large and high aspect ratio cells contain long struts, locally the relative density is low producing a locally less stiff and less strong cellular material, resulting in large strains. This is still the case for $\delta = 0.4$, but for a regularity of $\delta = 0.9$, the strains are more uniform across the structure for small strains. In nearly regular structures, the cells with T-like junctions or rhombus-shaped cells are found to be responsible for the initiation of localized deformation.

Fig. 4.14 shows the peak stress and peak strain as a function of relative density for different δ. Fig. 4.14(a) shows that the peak stress of structures with $\delta = 0.9$ is slightly larger than the peak stress for the other two values of δ. However, a clear ordering of the peak stress cannot be observed at low δ values. The peak strain in Fig. 4.14(b) clearly decreases with increasing structural randomness, especially for small relative densities. At low δ the strains are localized around large cells and attain values much larger than the average. As a result of this nonuniform distribution, critical strains can already be reached at small average strains, leading to lower peak strains

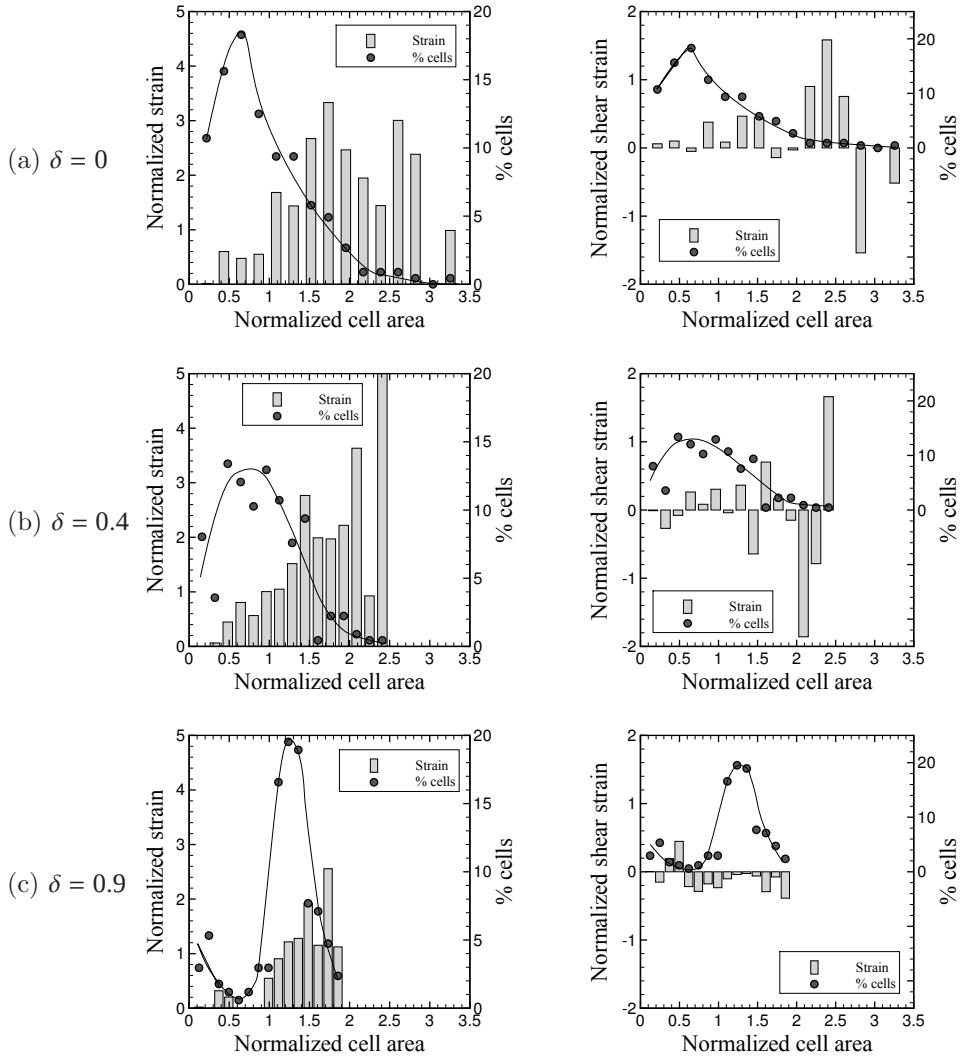

Figure 4.13: Cell level distribution of mean tensile strain along the loading direction (first column) and shear strain (second column) for the structures in the top row. Fig. 2.6 shows the typical structure for these randomness values. The cell strains are normalized with the current applied macroscopic strain $\epsilon^* = 0.004$. The cell area is normalized by the average area per cell (i.e. the total area of the Voronoi divided by the total number of cells). In this picture, $\overline{\rho} = 0.1$ and $N_s = 0.05$.

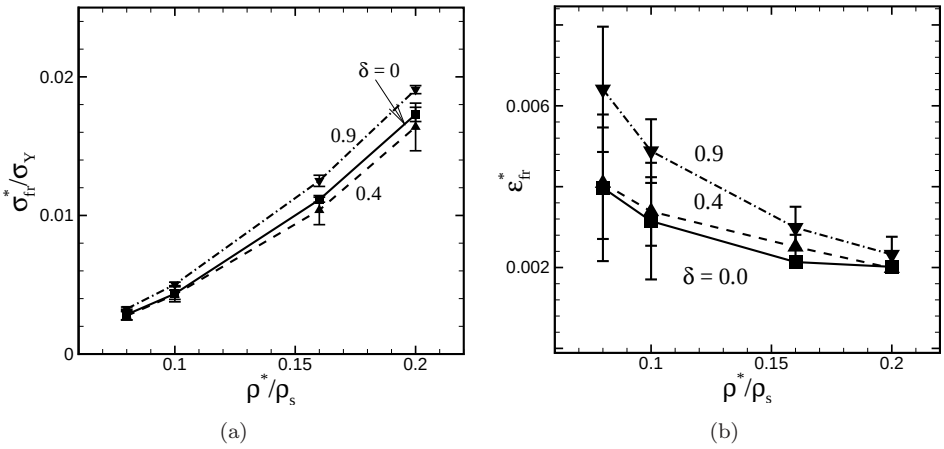

Figure 4.14: Effect of randomness on (a) the peak stress, (b) the peak strain.

compared to the more uniformly strained $\delta = 0.9$ structures.

4.4.2 The effect of cell shape anisotropy

Anisotropic Voronoi structures have been produced from initially isotropic Voronois ($\delta = 0.9$) by an affine scaling of the vertical dimensions while keeping the horizontal dimension unaffected. To allow for a clean study of the effect of anisotropy, we adjust the thickness of the struts of the anisotropic structures such that the relative density remains constant for different values of R. Fig. 4.15(a) shows the effect of anisotropy on the overall stress-strain response for three samples with $\bar{\rho} = 0.1$, loaded in the vertical direction. The first sample is generated by extending the vertical dimension with a factor $R = 1.3$ so that this sample is loaded in the rise direction (RD). The second sample is scaled with a factor $1/R$ in the vertical direction, so that this sample is effectively loaded in the transverse direction (TD). The RD and TD cases are compared to the original isotropic structure. The corresponding strain maps are shown in Fig. 4.16. Clearly, Fig. 4.15(a) shows that the elastic modulus is higher in the rise direction (RD) and lower in the transverse direction (TD). The yield stress and the peak stress are also higher in RD and lower in TD when compared to the isotropic structure. Damage accumulation in the structure is plotted in Fig. 4.15(b) by means of the number of damage locations as a function of the applied macroscopic strain. The damage initiation strain in RD is smaller than that in the isotropic structure, while it is larger in TD. It can also be observed that the damage accumulates at a slightly higher rate in RD, while it is somewhat lower in TD. This explains the

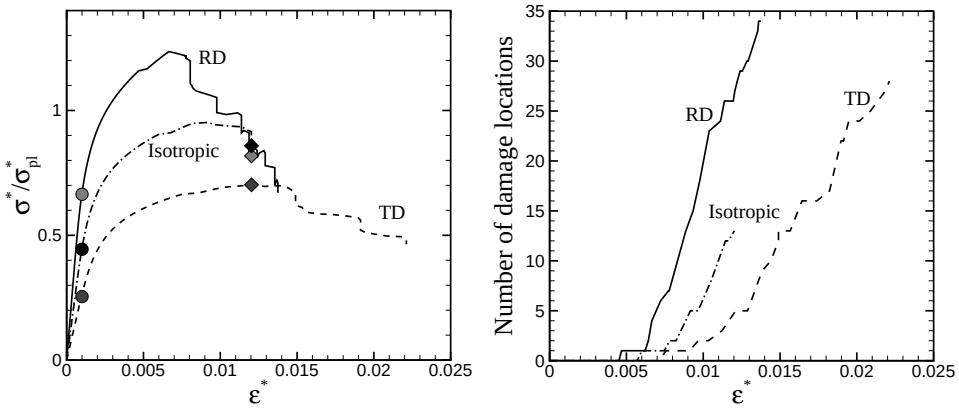

(a) (b)

Figure 4.15: Effect of cell shape anisotropy: (a) Stress-strain curves; (b) damage evolution ($\bar{\rho} = 0.1, N_s = 0.1$ and $R = 1.3$). Symbols in (a) correspond to the strain maps of Fig. 4.16.

lower peak strain for RD and the larger peak strain for TD compared to the isotropic structure. Fig. 4.16 shows the local strain distribution in the structures for small (top row) and large (bottom row) strains corresponding to the labels on the stress-strain curves in Fig. 4.15(a). Since the underlying isotropic structure is the same, the relative position of the "weak links" is unchanged in all the three structures and produces similar strain distribution patterns (the strains have been normalized with the macroscopic strain ϵ^*). Note that for $\epsilon^* = 0.001$ (corresponding to the circles in Fig. 4.15(a)), many more struts have plastically yielded (white portions) for RD compared to TD, although the macroscopic strain ϵ^* is similar. Except for small differences in the local strain levels at a few locations, the overall strain pattern is similar. As has been quantified in Fig. 4.15(b), an increasing amount of damage can be seen in the fracture band for RD compared to the TD structure at large strains (see the bottom row of Fig. 4.16). Clearly, at the mesoscopic level, similar deformation and damage mechanisms exist in anisotropic structures as in isotropic structures (see also section 4.3.1).

The regular hexagonal structure provides a convenient model system to understand the structural response of random Voronois in terms of the cell wall deformation and failure. Similar to the Voronoi structures, the regular hexagonal structure is subjected to an affine scaling in the vertical direction by the prescribed anisotropy ratio R leading to an anisotropic hexagonal structure, defined by t_R, l_R, h_R and θ_R (see the schematic in Fig. 4.17(a)). Hexagonal structures corresponding to RD are produced

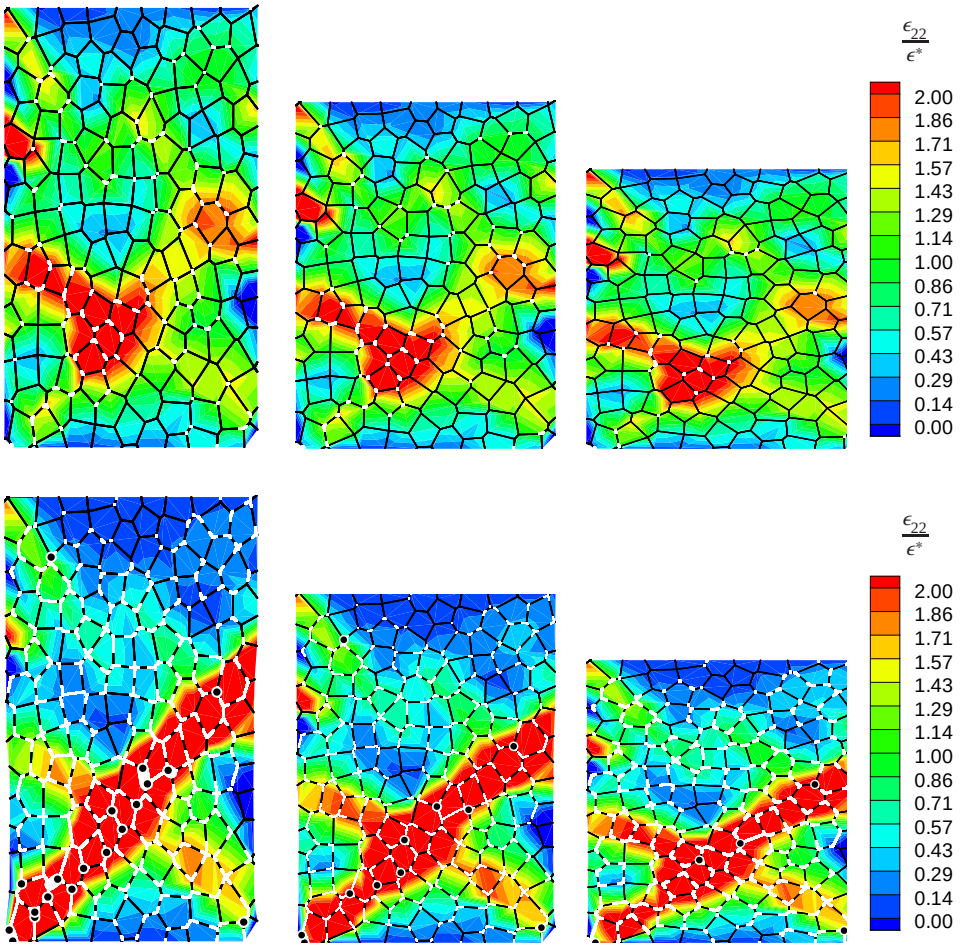

(a) RD (b) Isotropic (c) TD

Figure 4.16: Comparison of strain distribution in structures with cell shape anisotropy. The first and second rows correspond to small and large strain values indicated by the symbols (●) and (◆) in the stress strain curves in Fig. 4.15(a), respectively. On the superimposed Voronoi structure, plastic portions of the struts are shown in white, while damage locations are shown with black filled circles. The thick white struts have completely failed.

with R (R = 1.4), while those in TD have been generated with $1/R$. Subjecting the scaled unit cell (which includes only one-half of the inclined strut length shown in Fig. 4.17(a)) to the same boundary conditions as in Fig. 4.2(a), the resulting overall

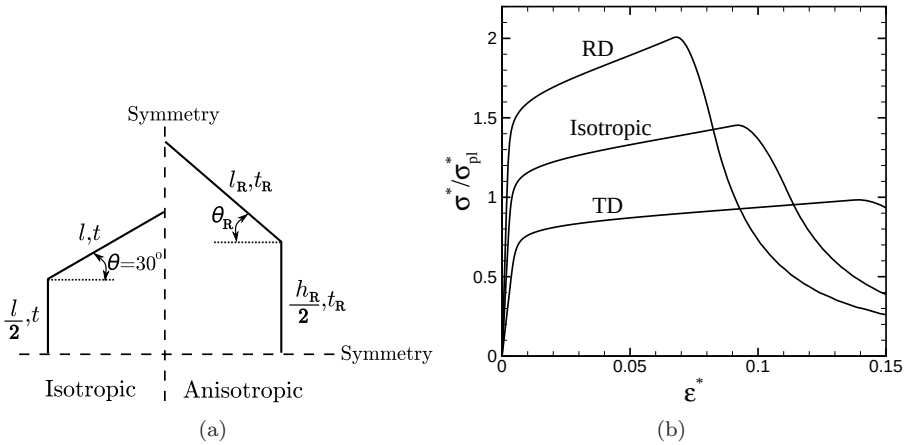

Figure 4.17: (a) Schematic figure showing isotropic and anisotropic ($R > 1$) hexagonal structures (RD). Only one-half of a cell is shown for each case placed adjacently on either side of the vertical symmetry line. (b) Stress-strain curves of anisotropic hexagonal structures with $\overline{\rho} = 0.058$ and $N_s = 0.05$.

stress-strain response is plotted in Fig. 4.17(b). It should be noted here that the thickness of the struts is different in the three cases as the relative density is kept constant, giving rise to a larger thickness for RD than TD. Fig. 4.17(b) shows that the elastic modulus, yield stress and hardening slope is larger for RD compared to TD, while the peak strain is reduced. We can understand the reduced peak strain for RD by using the curvature argument similar to that discussed in section 4.3.2 with respect to Fig. 4.8. Comparing RD ($R > 1$) to the isotropic structures leads to an increase in θ_R, l_R and h_R. Since we keep the relative density unchanged, this will also result in an increase in t_R. Because l_R and h_R increase, the rate at which the curvature at the triple point increases with the macroscopic strain ϵ^* is much larger. In addition, the critical curvature $\kappa_F = 2\varepsilon_F/t_R$ is further decreased because of the increase in t_R. The macroscopic yield stress and peak stress are higher in RD owing to the fact that an increasing $\theta_R(> \theta)$ will decrease the shear force on the inclined strut so that a larger macroscopic stress is required to attain the critical bending moment at the triple point. In addition, the critical bending moment required for yielding and failure is larger due to the larger strut thickness (e.g. $M_P = 1/4\sigma_Y t^2$). An exactly opposite behaviour in TD results from the fact that in this case $\theta_R(< \theta)$ decreases with increasing R. A similar influence of the anisotropy on the strut deformation occurs in the random structures, exhibiting essentially the same trends in the macroscopic behaviour.

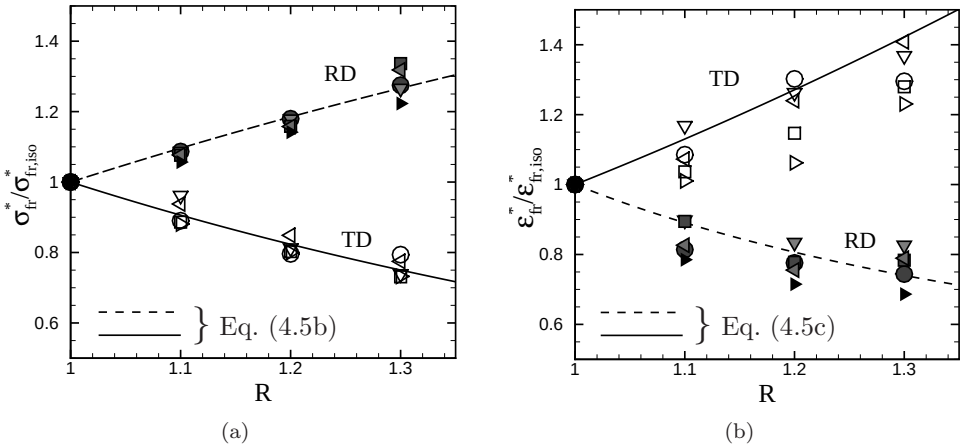

Figure 4.18: Effect of anisotropy on (a) peak stress and (b) peak strain for five relative densities ($\overline{\rho}$ = 0.08, 0.1, 0.16, 0.2 and 0.24) shown in different filled (RD) and open (TD) symbols. The peak stress and peak strain are normalized with those of the isotropic structure for that specific relative density.

We now proceed to study the effect of R on the peak stress and the peak strain for a range of relative densities ($\overline{\rho}$ = 0.08, 0.1, 0.16, 0.2 and 0.24) in Fig. 4.18 for the random Voronoi structures (cf. Fig. 4.15 and 4.16). It can be observed that the peak stress in the rise direction increases, while the peak strain decreases with R. In the transverse direction, an opposite behaviour of the peak stress and the peak strain can be seen. The different symbols are for different relative densities. There is no ordering among the different relative densities, so that the effect of anisotropy appears to be independent of the relative density. From Fig. 4.18(a), it can be deduced that $\sigma^*_{\rm fr} \approx R\sigma^*_{\rm fr,iso}$ for RD and $\sigma^*_{\rm fr} \approx (1/R)\sigma^*_{\rm fr,iso}$ for TD, with the density dependence fully accounted for through $\sigma^*_{\rm fr,iso}$. A similar trend (i.e. $\epsilon^*_{\rm fr} \approx (1/R)\epsilon^*_{\rm fr,iso}$ for RD and $\epsilon^*_{\rm fr} \approx R\epsilon^*_{\rm fr,iso}$ for TD) holds for the peak strain $\epsilon^*_{\rm fr}$ in Fig. 4.18(b).

To explain the above trends in the macroscopic behaviour of random Voronoi structures, we compare them to regular hexagonal structures. The affine scaling of the isotropic hexagonal structure produces vertical and inclined struts of lengths $h_{\rm R}$ and $l_{\rm R}$, respectively (see Fig. 4.17(a)). The initial strut angle θ (=30^o) changes to $\theta_{\rm R}$. The following relations hold between the isotropic and anisotropic hexagonal structures with the same relative density:

$$\left.\begin{array}{rcl} h_{\mathrm{R}} & = & R\,l, \\ l_{\mathrm{R}}\cos\theta_{\mathrm{R}} & = & l\cos\theta, \\ t_{\mathrm{R}} & = & 3\dfrac{R\cos\theta_{\mathrm{R}}}{R\cos\theta_{\mathrm{R}}+\sqrt{3}}\,t, \end{array}\right\} \tag{4.2}$$

where $\theta_{\mathrm{R}} = \tan^{-1}(R\tan\theta)$. According to Gibson and Ashby (1997), the scaling relations for the elastic modulus and plastic collapse stress can be written as

$$\frac{E^*_{\mathrm{iso}}}{E_{\mathrm{s}}} = \left(\frac{t}{l}\right)^3 \frac{1+\sin\theta}{\cos^3\theta}\,, \quad \frac{\sigma^*_{\mathrm{pl,iso}}}{\sigma_{\mathrm{Y}}} = \left(\frac{t}{l}\right)^2 \frac{1}{2\cos^2\theta}, \tag{4.3}$$

$$\frac{E^*_{\mathrm{R}}}{E_{\mathrm{s}}} = \left(\frac{t_{\mathrm{R}}}{l_{\mathrm{R}}}\right)^3 \frac{h_{\mathrm{R}}/l_{\mathrm{R}}+\sin\theta_{\mathrm{R}}}{\cos^3\theta_{\mathrm{R}}} \quad \text{and} \quad \frac{\sigma^*_{\mathrm{pl,R}}}{\sigma_{\mathrm{Y}}} = \left(\frac{t_{\mathrm{R}}}{l_{\mathrm{R}}}\right)^2 \frac{1}{2\cos^2\theta_{\mathrm{R}}}, \tag{4.4}$$

respectively. Here the subscript 'iso' refers to the isotropic regular hexagonal structure, while the subscript 'R' refers to the anisotropic hexagonal structure. It follows from Eqs. (4.2)-(4.4) (and the fact that $\theta = 30^o$) that

$$\frac{E^*_{\mathrm{R}}}{E^*_{\mathrm{iso}}} = 18\sqrt{3}\frac{(R\cos\theta_{\mathrm{R}})^4}{(R\cos\theta_{\mathrm{R}}+\sqrt{3})^3}, \tag{4.5a}$$

$$\frac{\sigma^*_{\mathrm{pl,R}}}{\sigma^*_{\mathrm{pl,iso}}} = 9\left(\frac{R\cos\theta_{\mathrm{R}}}{R\cos\theta_{\mathrm{R}}+\sqrt{3}}\right)^2 \tag{4.5b}$$

and by using $\epsilon^*_{\mathrm{pl}} = \sigma^*_{\mathrm{pl}}/E^*$,

$$\frac{\epsilon^*_{\mathrm{pl,R}}}{\epsilon^*_{\mathrm{pl,iso}}} = \frac{1}{2\sqrt{3}}\frac{R\cos\theta_{\mathrm{R}}+\sqrt{3}}{(R\cos\theta_{\mathrm{R}})^2}. \tag{4.5c}$$

We compare Eqs. (4.5b) and (4.5c) for the normalized plastic collapse stress and strain with the numerical results for the peak stress and peak strain in Fig. 4.18. It follows that Eq. (4.5b) nicely captures the dependence of the peak stress on anisotropy, while Eq. (4.5c) slightly overestimates the peak strain. Clearly, when normalized with the properties of the isotropic structure, the effect of anisotropy can be carefully captured by the simple expressions in Eq. (4.5) both for plastic collapse as well as fracture.

4.4.3 Size effects

In this section, we explore the effect of specimen size on the overall mechanical properties. The relative density and the strain hardening exponent are fixed at $\bar{\rho} = 0.1$ and $N_{\mathrm{s}} = 0.1$. The effect of specimen size is studied in two ways. In the first set of

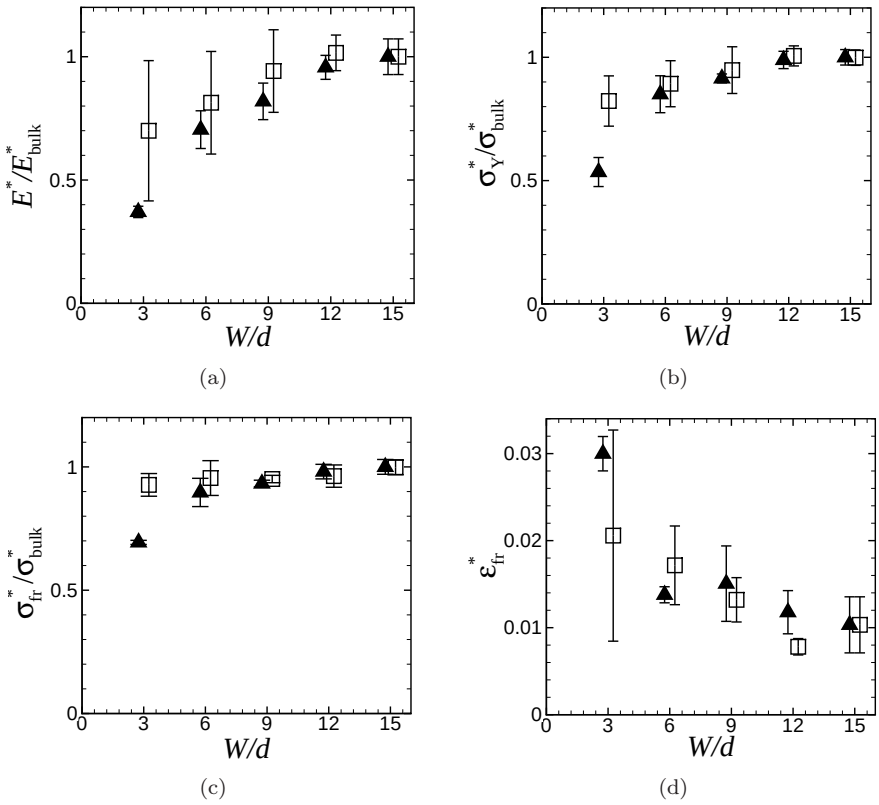

Figure 4.19: Size effect on the macroscopic properties of Voronoi structures. The (▲) symbols correspond to fixed H/d, while the (□) symbols correspond to fixed aspect ratio H/W calculations. For clarity, the points are offset horizontally by an amount of ±0.25. The "bulk" properties correspond to the properties at $W/d = 15$.

calculations, the height of the specimen is kept constant ($H/d = 20$) and the width is varied ($W/d = 3$ to 15). These results correspond to the filled triangles in Fig. 4.19. The change in the elastic modulus E^* is shown in Fig. 4.19(a). The modulus is low at small specimen widths and increases with W/d, showing a convergence roughly for $W/d \geq 12$. Fig. 4.19(b) shows the variation in the yield strength σ^*_Y as a function of the specimen width W/d. The yield strength σ^*_Y is taken as the stress at which the stress-strain curve starts to deviate from linearity. The yield strength also shows a similar behaviour as the modulus; it is low at small specimen widths and exhibits an increasing trend with W/d until it converges at $W/d \geq 12$ to a value representing the bulk yield strength. These trends are consistent with the findings of Bastawros

et al. (2000); Bastawros and Evans (2000); Andrews et al. (2001); Onck et al. (2001); Tekoğlu and Onck (2008) and Tekoğlu et al. (2010). The reason for this behaviour in modulus and strength is related to the compliant and stress-free boundary layers which are of fixed width for any W/d. As the left and right boundaries are stress-free (see Fig. 4.1), the local stresses will increase from zero at the free edge to a uniform value in the interior (bulk) over a short distance, which is approximately one cell in width for any W/d. These compliant boundary layers decrease the overall modulus for small W/d. Increasing the number of cells in the bulk will reduce the effect of these free-edges and the modulus increases with W/d, resulting in the observed size effect. Due to the lower stress in the boundary layers, force equilibrium in the loading direction requires that the local stress σ_{22} in the center of the specimen to be larger than the macroscopic stress σ^* calculated based on the specimen width W. The smaller the normalized width W/d, the higher is the bulk stress value, since the free-edge-influenced regions cover a greater fraction of the width. This leads to an early yielding at small W/d. With increasing number of cells in the width, the difference between the bulk stress and the macroscopic stress decreases and the yield strength of the structure eventually becomes independent of the specimen width at large W/d. The effect of specimen width on the fracture stress shows a very similar trend as the yield stress (see Fig. 4.19(c)), which can also be understood from the same arguments of local stress distribution across the specimen width. The fracture strain, on the other hand, is large at low specimen widths and shows a decreasing trend with W/d before it converges to a bulk value (see Fig. 4.19(d)).

In the other set of calculations (the square symbols in Fig. 4.19), the aspect ratio H/W is fixed at $4/3$ and W/d is varied from 3 to 15. We have observed similar trends in macroscopic properties in both specimen geometries, although the drop in modulus, yield strength and peak stress and the increase in peak strain are less pronounced. When the aspect ratio is fixed, the constraints at the top and bottom boundaries result in rigid specimen volumes of a few cell layers. These rigid cell layers produce extra stiffening and strengthening effects at small H/d. Hence, the data points corresponding to the fixed aspect ratio simulations lie above those of the fixed height calculations for the modulus, yield stress and peak stress.

To explain the effect of specimen size on the fracture strain (Fig. 4.19(d)), we analyze the damage accumulation. In Fig. 4.20, the damage evolution is plotted as a function of the macroscopic strain for different W/d and for a fixed $H/d = 20$. The amount of damage, i.e. the number of damage locations, is normalized with the total number of struts in the individual structures. The damage onset strain is shown to decrease with increasing W/d, while the rate of damage accumulation does not appear to be influenced by the specimen width. For small widths, the enhanced onset strain appears to be responsible for the large ductility for small samples.

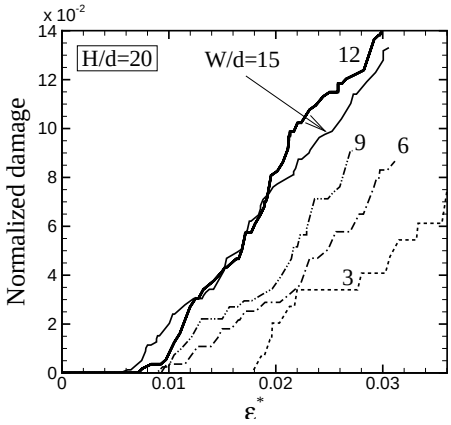

Figure 4.20: Damage evolution in Voronoi structures of a fixed height $H/d = 20$ but with different widths W/d.

4.5 Discussion

In this chapter, we explore the effect of the microstructure on the overall fracture behaviour and internal damage evolution of two-dimensional metallic foams. Two microstructural levels can be identified: that of the struts themselves (determining the solid properties $\sigma_{\rm Y}$, $N_{\rm s}$, $\sigma_{\rm F}$ etc.) and that of the cellular architecture. Differences in the cellular architecture affect the mesoscopic (cell scale) deformation process and thus the overall stress-strain response. For example, regular hexagonal structures show three distinct regimes in their macroscopic stress-strain response corresponding to elastic deformation, plastic deformation and fracture in the struts (see Fig. 4.2). At the end of the second regime, the peak stress is reached soon after the first fiber failure in the plastic zones near the triple point. Due to the symmetry of these perfect structures, yielding and subsequent fiber failure occurs at the same instant for all the triple points. In random structures, however, an additional distinct regime can be identified along with the above three, where a competition occurs between the strain hardening and softening due to damage (see e.g. regimes III and IV of Fig. 4.3). Motz and Pippan (2001) have also reported four regimes in Alporas foams subjected to tension. They have associated the rearrangement of high strain pockets of approximately one cell diameter (formed during plastic deformation and before damage initiation) with the wavyness in the cell walls. In our simulations with straight cell walls, we also found similar high strain regions occurring from plastic deformation of relatively large cells (see Fig. 4.13). Dillard et al. (2005) and Amsterdam et al. (2006c, 2008a) have reported a pre-peak regime of damage

accumulation and Marchi et al. (2004) and Amsterdam et al. (2008b) argue that the rate of internal damage accumulation is crucial in the formation of the peak stress. These arguments are in line with our simulations, in which we observe that the competition between the strain hardening and softening due to damage controls the damage development. Subsequent damage localization occurs in various competing regions to form a fracture band. Once this fracture band has been formed, the peak stress will be attained followed by crack propagation in regime IV of the stress-strain curve (Fig.4.3).

Care should be taken in relating our 2D simulation results to experiments on 3D foams. In our simulations, the fracture bands have always been observed around 45° orientations with respect to the loading axis (see Figs. 4.4, 4.5 and 4.16) as also observed in the absence of damage (Silva and Gibson, 1997a; Badiche et al., 2000; Alkhader and Vural, 2008; Mangipudi et al., 2010). In a recent analysis (Tekoğlu et al., 2010), it has been shown that only one mechanism of cell level deformation, namely a distortion plus rotation, exists in 2D Voronoi honeycombs, whereas Bastawros et al. (2000) have observed that the cells in Alporas foams can deform either by only distortion or distortion plus rotation or distortion plus in-plane shear. Bart-Smith et al. (1998) have pointed out that the cells that undergo severe deformation inside the localization bands have either elliptical cell morphologies or cells having a T-shaped cell wall junctions. Such more compliant cells cannot deform in an isolated manner as they are constrained by the surrounding cells. In contrast to 2D, these 3D cells are subjected to additional constraints in the out-of-plane direction. This explains the difference between the orientation of the deformation bands in our simulations compared to experimental bands which are often almost perpendicular to the loading axis, only rarely reaching 70°.

We have investigated the effect of cell shape anisotropy and found an increasing peak stress and decreasing peak strain in the rolling direction (RD) with increasing R. The opposite effect was found in the transverse direction (TD). The observation that the peak stress in RD is larger and peak strain is lower compared to TD is consistent with a number of experimental observations (Banhart and Baumeister, 1998; Dillard et al., 2006; Amsterdam et al., 2008d). In RD, we found an early damage onset and higher damage accumulation rate, owing to the decreased critical curvature and increased rate of curvature development at the triple points. The peak stress and peak strain behaviour can be nicely captured by closed-form expressions based on plastic yielding (Eq. 4.5).

A key parameter in metal foams is the relative density. We found that the exponent of the power-law relating the peak stress to the relative density is close to 2 for a wide range of different material parameters (including the heat treatment study) and different topologies (anisotropy and structural randomness) considered here, iden-

tical to that of the plastic yield (collapse) strength of two-dimensional structures. The peak strain also has a strong dependence on the relative density, showing higher peak strains at lower densities with a power-law exponent approximately equal to -1. These trends are consistent with experimental studies, in which the power-law dependence of the peak stress on relative density was found to be similar to that of the plastic collapse stress (McCullough et al., 1999b; Amsterdam et al., 2008b). In addition, similar trends in peak strain were reported in Duocel foams tested in tension (Amsterdam et al., 2008b), Al-Si-Cu foams tested in compression (Banhart and Baumeister, 1998) and in Alporas tested both in tension and compression (Markaki and Clyne, 2001), with low relative density samples exhibiting higher peak strains compared to the higher relative densities.

We have also explored the effect of heat treatment by imposing solid properties corresponding to a tempering and annealing treatment, resulting in a larger peak stress and smaller peak strain for tempered compared to annealed, in agreement with experiments (Banhart and Baumeister, 1998; Krishna et al., 2007; Amsterdam et al., 2008b). Since almost all material parameters differ (σ_Y, N_s, ε_F and Γ_0) for the two heat treatment conditions, the question remains as to what is the key parameter that causes this effect. Here, we can gain valuable insight from the simulations of section 4.3.2 in which we only changed the hardening exponent, while keeping all other parameters unaffected. Fig. 4.7(a) shows that the peak stress scales with relative density power 2 for all hardening exponents and that hardening increases the peak stress. Increasing hardening in the solid for a fixed fracture strain ε_F also increases the fracture stress σ_F, suggesting a possible correlation with σ_F. Indeed, Fig. 4.21(a) shows that by normalizing the peak stress with σ_F all data points (including the heat treated materials) collapse on one curve that can be accurately fitted by

$$\frac{\sigma^*_{fr}}{\sigma_F} = C_1 \left(\frac{\rho^*}{\rho_s}\right)^2. \tag{4.6}$$

Here, $C_1 \approx 0.32$ is a dimensionless proportionality factor which depends on structural topology only. We have also plotted the results for cell shape anisotropy (section 4.4.2) on Fig. 4.21(a). The effect of anisotropy can be approximated by $C_1' = RC_1$ for RD and by $C_1' = C_1/R$ for TD. In case of structural randomness (section 4.4.1), the effect is to lower the value of C_1 (e.g. $C_1 = 0.27$ for $\delta = 0$). However, a relationship of C_1 with δ could not be obtained due to the lack of a clear ordering at low δ. We have carried out a similar exercise for the peak strain. The peak strain is primarily dependent on the fracture strain ε_F which governs the damage onset in the struts (see Fig. 4.8 and the discussion). For a fixed ε_F, Fig. 4.7(b) shows that the peak strain is also directly proportional to N_s. After normalizing the peak strain data

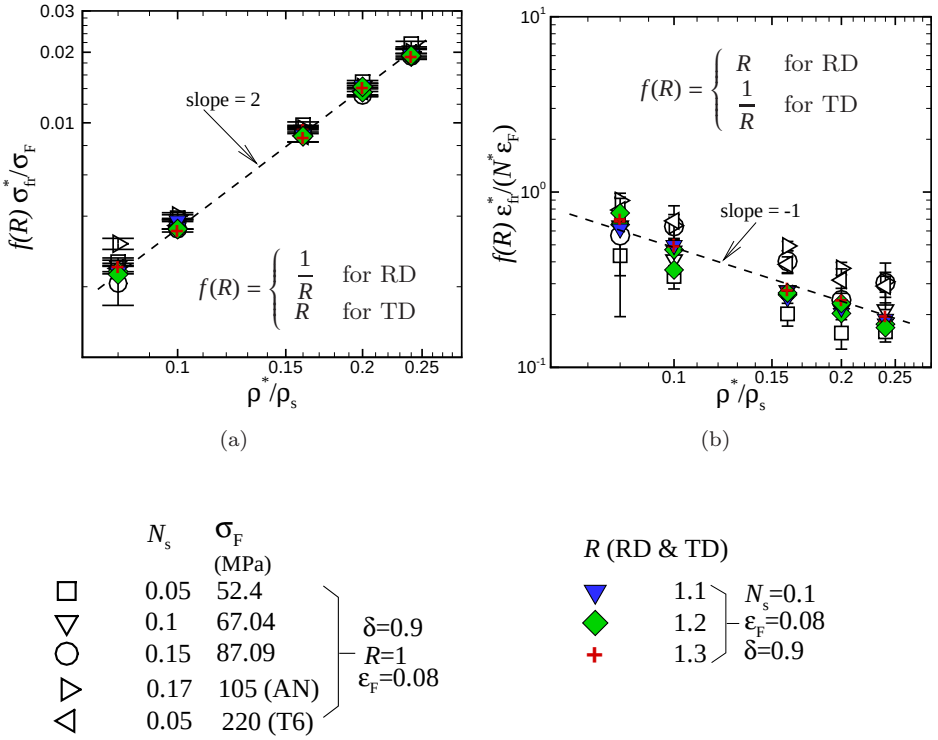

Figure 4.21: Normalized peak stress as a function of relative density. Shown below is the legend representing both the figures.

from Figs. 4.7(b) and 4.10(b) using $N_s\varepsilon_F$, all data collapsed except the data from T6, whose yield stress σ_Y differs strongly from the rest of the data, suggesting an influence of the yield strain $\varepsilon_Y = \sigma_Y/E$ on the inelastic deformation regimes (regimes II and III in the stress-strain curve). It has been shown in Mangipudi et al. (2010) that an interaction of ε_Y with N_s produces an enhanced overall hardening of the cellular material N^*, which can be written as

$$N^* = N_s + a_1\sqrt{\varepsilon_Y} \tag{4.7}$$

with a_1 a dimensionless constant and by neglecting the effect of relative density, which was found to be small. By using N^* instead of N_s for normalization, all the data were

found to cluster around a power -1 dependence of relative density, according to

$$\left(\frac{\epsilon^*_{\mathrm{fr}}}{N^*\varepsilon_{\mathrm{F}}}\right) = C_2\left(\frac{\rho^*}{\rho_{\mathrm{s}}}\right)^{-1} \tag{4.8}$$

with $C_2 = 0.05$ and $a_1 = 5.6$ in Eq. 4.7. Fig. 4.21(b) shows all data from Figs. 4.7(b) and 4.10(b), to which we have also added data from the anisotropic structures of Fig. 4.18(b) by using the function $f(R) = R$ for RD and $1/R$ for TD. Although the normalization does not yield a similar strong correlation as the peak stress, the widespread unnormalized peak strain data closely agglomerates around one curve, indicating that Eq. 4.8 is able to capture the collective effect of all parameters that are important in determining the peak strain, i.e. N_{s}, σ_{Y}, $\bar{\rho}$ and ε_{F}.

4.6 Conclusions

The various trends observed so far are summarized in Fig. 4.22, elucidating the opportunities to optimize the strength and ductility of cellular metallic structures. From a practical point-of-view, materials for structural engineering applications require a good combination of ductility and strength. Increasing relative density increases the strength at the expense of ductility, due to an early onset of damage initiation and an increased damage accumulation rate for larger densities (see Fig. 4.6). For a required density, conventional metallurgical techniques can be used, aimed at enhancing the strength of the constituent material through alloying and heat treatments, such as e.g. tempering of Al-alloys. To enhance the strength, the primary goal of these techniques is to produce second phase particles and grain boundary precipitates which create obstacles for the movement of dislocations. Unfortunately, at the same time, these second phase particles and grain boundary precipitates also knock down the ductility in foams. The effect of brittle precipitates has been shown to be most deleterious and leads to a reduction of both ductility and strength. Aluminium alloys in tempered (T6) conditions possess a low strain hardening capacity besides loosing ductility in the process of increasing the yield strength. This solid material behaviour is carried over to the cellular metal resulting in enhanced strength at lower ductility. Among all parameter variations in the heat treatment, the solid's fracture stress was found to be dominant in enhancing the peak strength (see Eq. 4.6 and Fig. 4.21(a)). Most beneficial for metal foams turns out to be an enhanced strain hardening at fixed fracture strain, which postpones the onset of damage accumulation and leads to an increase of both strength and ductility (see Fig. 4.6 and 4.22).

Apart from the solid material properties, the cellular architecture also plays an important role in determining the overall mechanical response. Decreasing the struc-

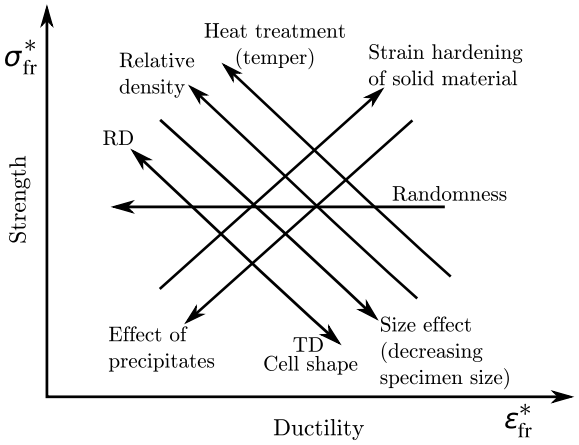

Figure 4.22: Schematic summarizing the influence of various material and structural parameters on the strength and ductility of cellular solids.

tural randomness increases the ductility while leaving the peak stress relatively unaffected. When the loading direction is known a-priori, cell shape anisotropy at constant relative density can help increasing the strength, but at the expense of ductility (RD in Fig. 4.18 and 4.22). Transverse to that direction, an exactly opposite behaviour can be observed (TD). Closed-form expressions based on overall plastic properties were found to yield excellent agreement with the simulations (see Eq. 4.5 and Fig. 4.18). Finally, for specimens consisting of only a few cell sizes in width, it was found that the ductility increases with decreasing size accompanied by a (modest) reduction in strength. The knowledge of the effects of various material and architectural parameters as summarized in Fig. 4.22 can help in designing metal foams with improved fracture properties.

Based on: K.R. Mangipudi and P.R. Onck – *"Notch sensitivity of ductile metallic foams: A computational study"*, Acta Mater., Vol. 59, No. 19, p.7356-7367, 2011.

Chapter 5
Notch sensitivity of ductile metallic foams

A fact is a simple statement that everyone believes. It is innocent, unless found guilty. A hypothesis is a novel suggestion that no one wants to believe. It is guilty, until found effective.

Edward Teller

The role of notches on the fracture strength of metal foams has been studied using a multiscale model based on a two-dimensional Voronoi representation of the cellular architecture. The effect of the crack length to the specimen width ratio on the net section strength of double edge notch (DEN) specimens and central crack panels (CCP) has been investigated in two ways: (i) by fixing the number of cells in the width and (ii) by fixing the number of cells in the ligament. Notch strengthening has been observed in DEN specimens in excellent agreement with experiments. Analysis of the strain fields suggests that in the DEN configuration, the constraint imposed on the rotation fields in the notch tip zones of the ligament enhances the net section strength. In CCP specimens, stress concentration and free-edge effects produced a small level of notch weakening. Our results show that both the ligament length as well as the notch length (normalized by the cell size) influence the notch behaviour in two-dimensional metal foams.

5.1 Introduction

Fabrication of the foam components in certain cases requires the deliberate introduction of extrinsic macroscopic defects like holes, corners and notches. Also, internal defects like cracks may be generated due to service-induced damage. Stress inhomogeneities develop around these defects affecting the macroscopic mechanical

behaviour. On the other hand, the cell size of the commercially available metal foams is about 1-10 mm, which is often of the same order as the minimum structural dimension of the foam components. Hence, a thorough understanding of the role of these defects at these length scales is necessary for an efficient design of damage tolerant foam components.

Several experimental studies have reported the role of edge notches, central cracks and holes on the maximum net-section stress in both tension and compression. The presence of these defects can lead to a higher or lower maximum net-section stress compared to the unnotched samples, which is generally termed notch-strengthening or notch-weakening, respectively. The reported behaviour can be categorized into two regimes: the first in samples with few cells where cell size effects might be expected, and the second in samples containing a relatively large number of cells displaying "bulk" behaviour. In both the regimes, the general trend for central crack panels (CCP), single edge notch (SEN) specimens and samples with holes is a notch insensitive behaviour in both compression and tension. In specimens containing around twenty cells in width, Onck (2003) and Antoniou et al. (2004) found notch insensitive behaviour in CCP and SEN specimens. Paul et al. (1999) have investigated closed-cell Alporas foam samples with approximately two to three cells in the thickness and reported a notch insensitive behaviour for centrally located sharp cracks, and found notch weakening in case of holes. For the same range of hole size to cell size ratios, but in thicker (more than seven cells) specimens, Olurin et al. (2001) reported notch insensitive behaviour in Alporas, Alcan and Inco foams, in both tension and compression up to a hole diameter to sample width ratio (D/W) of 0.4. They predicted a toughness-dependent transition leading to notch-weakening at very large hole size to cell size ratios (ratios up to 100). McCullough et al. (1999a) have also found a notch insensitive behaviour, for holes up to $D/W = 0.4$ in Alulight foams under compression. Experiments by Fleck et al. (2001) and the finite element calculations of Chen et al. (2001a) treating the foam as a continuum (with the Deshpande and Fleck (2000) yield function appended with a cohesive zone model) also support these findings. The explanation for this notch insensitivity is that below the toughness-dependent flaw size, failure is strength controlled (Paul et al., 1999; Olurin et al., 2001) and thus the ligament can accommodate the deformation through simple crushing (Antoniou et al., 2004). In the continuum approximation, Fleck et al. (2001); Chen et al. (2001a) showed that indeed a notch ductile-brittle transition (i.e. a severe reduction in net section strength) occurs beyond this transition flaw size.

In large double edge notch (DEN) metal foam samples under compression, no notch strengthening is predicted, since–in contrast to the dense solids–metal foams cannot develop plastic constraints as the plastic Poisson's ratio ν_p is close to zero for many low density foams (Ramamurty and Kumaran, 2004; Gioux et al., 2000;

Deshpande and Fleck, 2000). Numerical simulations of DEN specimens in compression have indeed shown the inability of the compressible continuum to develop a plastic constraint in the ligament under compressive loading for $\nu_p < 0.3$ (Onck, 2001a). However, in a recent study by Combaz et al. (2010), it is shown by means of continuum finite element simulations that strain hardening in tension can lead to an enhanced stress triaxiality in notched cylindrical specimens which could explain the notch strengthening found in replicated Al foam with $\nu_p < 0.3$. On the other hand, smaller DEN specimens have exhibited notch strengthening in a number of tension/compression experiments on Duocel (Andrews and Gibson, 2001a), Alporas (Sugimura et al., 1997; Motz and Pippan, 2001; Onck and Bastawros, 2000; Antoniou et al., 2004) and Alulight (McCullough et al., 1999a), in addition to the numerical simulations (not accounting for damage) by Andrews and Gibson (2001b) and Onck (2001b, 2003).

When a strong plastic constraint is not present, cell level interactions were suggested to cause the notch strengthening. Andrews and Gibson (2001a) have proposed a mechanism of notch strengthening due to the localized shear at the notch tip in addition to the axial yielding of the ligament. The same mechanism can also be envisaged as a cell size effect of the uncracked ligament width, always accompanied by a shear zone of fixed width near the notch tips (Onck and Bastawros, 2000). Based on the observation of the inclined strain fields at the crack tip in Alporas DEN specimens, Antoniou et al. (2004) explained the notch strengthening also as a cell size effect of the ligament, but now due to a constraint-based enhancement of the flow stress in a limited-sized shear zone at the crack tip. The success of these models in explaining the experimental trends emphasize the role of the characteristic length scale (i.e. the cell size) which is not contained in the classical continuum models of metal foams.

An idealization of the discrete foam as a compressible continuum is only valid at length scales much larger than the cell size (Deshpande and Fleck, 2000; Badiche et al., 2000). When the structural length scale becomes comparable to the cell size, size effects are exhibited (see e.g. Tekoğlu et al. (2010)). In order to capture the size effects, either the classical continuum has to be extended to include a characteristic length scale in the constitutive description or the cellular structure has to be explicitly accounted for using micromechanical modelling. Dillard et al. (2006); Neff and Forest (2007) and Tekoğlu and Onck (2008) have applied different higher order continuum theories to study the strain fields around a hole in an infinite medium and were able to capture some of the cell size effects observed in the experiments by Dillard et al. (2006). Discrete micromechanical models of the foam have also been used to study the elastic strain fields around the holes (Tekoğlu and Onck, 2008) as well as the effect of sharp notches in DEN specimens on the macroscopic yield properties (Andrews

and Gibson, 2001b; Onck, 2001b). Nevertheless, these modelling studies on finite sized samples have been limited to elasto-plastic deformations and did not include damage. Using a multiscale model of the foam based on a Voronoi representation of the cellular architecture, we will study the effect of notches and holes in finite sized cellular structure under tension in the presence of damage.

The chapter is organized as follows. Section 5.2 provides the details of the finite element simulations. In section 5.3, the results on double-edge notched (DEN) structures and central crack panel (CCP) will be presented, followed by a study on the notch tip radius. At the end of section 5.3, cell size effects in the notched structures will be investigated. The results are discussed in section 5.4 in relation to the experiments and previous modelling studies. Finally, the conclusions are presented in section 5.5.

5.2 Finite element simulations

We will use the model described in section 2.3. Finite element calculations will be carried out on DEN (double edge notch) and CCP (central crack panel) structures shown in Fig. 5.1. It is common in continuum modelling to exploit the symmetry of the problem, and to make a computationally convenient choice of modelling only one-quarter of the complete structure. Such a choice for random cellular structures, however, infers the existence of cells with unacceptable shapes and concavity positioned at the symmetry axes. This is particularly unwanted in small samples where the variation in the stress/strain fields is expected to be on the order of a few cell diameters. The horizontal symmetry axis passes through the highly loaded notch tip regions in the DEN and CCP structures and hence symmetry boundary conditions cannot be prescribed along this axis. The vertical symmetry axis in the DEN specimens also passes through the stressed notch tip regions which forces us to model the complete DEN structure (see Fig. 5.1(a)). However, in the CCP configuration, the cells near the vertical symmetry axis are shielded by the central crack and therefore experience very low stresses, which allows us to consider only one-half of the structure (see the shaded portion in Fig. 5.1(b)). We found that the error introduced by this assumption is less than 4% in the mean peak stress (taken over four random realizations) compared to full CCP specimens for a range of a/W values from 0.19 to 0.73, see Fig. 5.4(b). Owing to the computational advantage, we will use symmetric CCP specimens in our simulations.

From the various length scales involved, one can identify $H/d, W/d, B/d, a/W$ and b/d as a choice of non-dimensional lengths, with d being the cell size. Note that these are not all independent, since $B/d = (W/d)(1 - a/W)$. The Voronoi structures have been generated using a regularity parameter of 0.9 (Zhu et al., 2001b). All

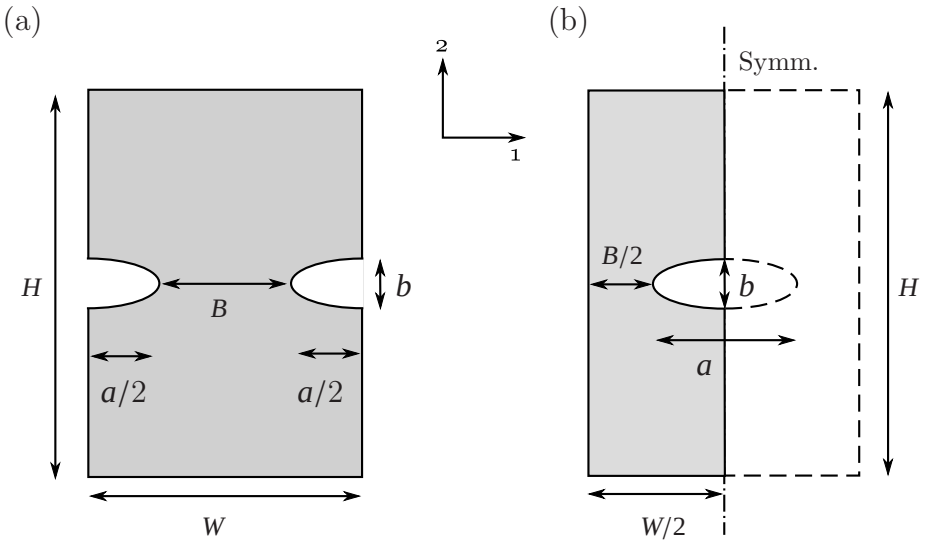

Figure 5.1: (a) Double edge notched (DEN) and (b) Central crack panel (CCP) configurations. The shaded areas indicate the portion of the structure chosen for the calculations. For CCP structures, symmetry boundary conditions are enforced along the symmetry line.

the calculations will be performed with a fixed structure height of $H/d = 40$. This height has been found large enough not to affect the results. While investigating the effect of a/W or b/d, we keep the normalized width W/d constant at 21 and 22 for the DEN and CCP structures, respectively. The mesh consists of a converged discretization of 40 equal-sized beam elements per strut. All the calculations have been performed for a relative density of $\bar{\rho} = \rho^*/\rho_s = 10\%$, where ρ^* is the density of the Voronoi structure and ρ_s is the density of the solid material. A uniform strut thickness $t_{avg} = \bar{\rho}(WH/L)$ is assigned to each strut, where W and H are the width and the height of the structure and L is the sum of all the strut lengths before the introduction of the notches. Struts that were partly cut during the generation of the notches will be stress-free and hence have been removed.

For both types of structures, the boundary conditions are such that the vertical displacement $v = U_{app}$ and $v = 0$ at the top and bottom edges, respectively, in addition to $f_x = m = 0$ with f_x being the force in the horizontal direction and m the moment. These boundary conditions allow for a horizontal displacement u and rotation ϕ of the top and bottom boundary nodes. In the DEN structures, one node from the bottom boundary is fully constrained to avoid rigid body modes. Symmetry boundary conditions ($u = \phi = f_y = 0$) are additionally imposed at the nodes along the

vertical symmetry line of the CCP structures (see Fig. 5.1(b)). Here, f_y is the force in the vertical direction. All the calculations have been conducted with a fixed set of solid material properties given by a Young's modulus $E = 70$ GPa, yield stress $\sigma_{\mathrm{Y}} = 41$ MPa, critical fracture strain $\varepsilon_{\mathrm{F}} = 0.08$, power-law strain hardening exponent $N_s = 0.1$ and fracture energy $\Gamma_0 = 5\sigma_{\mathrm{Y}}^2 l_0/(2E)$. The net section stress is calculated as $\sigma^{\mathrm{net}} = F/B$, where F is the sum of all the vertical forces at the top/bottom boundary and B is the initial ligament width. The applied strain is calculated as $\epsilon^* = U/H$, where U is the applied vertical displacement at the top boundary. The net section fracture stress $\sigma_{\mathrm{fr}}^{\mathrm{net}}$ is defined as the net section stress at the peak in the net section stress-strain curve. Four random realizations are used for statistical averaging of macroscopic properties throughout this chapter.

A strain mapping algorithm similar to the one proposed by Onck (2001b) and Tekoğlu and Onck (2008) has been used to visualize the strain fields at the cell scale, as often done experimentally using digital image correlation techniques. In this technique, the set of Voronoi cell nodes are triangulated and the displacements of the cell nodes are tracked. From these displacements, constant strain triangles are used to calculate the strains and local rotations for each triangle. The mean strain in a cell is obtained from the area weighted sum of the strains from the triangles belonging to a cell, which is then mapped back to the cell nodes. The strains and rotations are defined as $\varepsilon_{ij} = (u_{i,j} + u_{j,i})/2$ and $\omega_{ij} = (u_{j,i} - u_{i,j})/2$, respectively, where $u_{i,j} = \partial u_i/\partial x_j$ for $i, j = 1, 2$. Additionally, a cell stress mapping procedure has been developed in Mangipudi and Onck (2011a) which will be used to visualize the stress distribution at the cell level. If σ_{ij} and ε_{ij} are the "local stress" and "local strain" in these two-dimensional structures, the corresponding mean stress/strain and the effective stress/strain are defined as

$$\left.\begin{aligned} \sigma_{\mathrm{m}} &= \tfrac{1}{2}\sigma_{ii} \quad \text{and} \quad \sigma_{\mathrm{e}} = \sqrt{2\sigma'_{ij}\sigma'_{ij}} \\ \varepsilon_{\mathrm{m}} &= \tfrac{1}{2}\varepsilon_{ii} \quad \text{and} \quad \varepsilon_{\mathrm{e}} = \sqrt{\tfrac{1}{2}\varepsilon'_{ij}\varepsilon'_{ij}} \end{aligned}\right\} \qquad (i = 1, 2), \tag{5.1}$$

with $\sigma'_{ij} = \sigma_{ij} - \sigma_{\mathrm{m}}$ and $\varepsilon'_{ij} = \varepsilon_{ij} - \varepsilon_{\mathrm{m}}$.

5.3 Results

In the following sections, we will study the effect of notch depth to width ratio a/W on the net section fracture strength of DEN and CCP specimens. To investigate the effect of the ligament size B/d on the net section stress, we will also vary a/W independently by changing W/d for a fixed value of B/d.

5.3.1 The effect of notch depth in DEN specimens

Fig. 5.2(a) shows typical stress-strain curves of the DEN structures with elliptical notches of fixed $b/d = 1$, $W/d = 21$ and varying a/W. Since the specimen width W/d is kept constant, the B/d ratio changes with a/W, according to $B/d = (W/d)(1 - a/W)$. The net section stress σ^{net}, normalized with the fracture stress of the unnotched structure σ_{UTS}, is plotted as a function of the macroscopic strain ϵ^*. The stress-strain curves show a clear ordering in the elastic and plastic regimes. The simulations were discontinued arbitrarily after the peak which does not correspond to breaking of the sample. The net section fracture stress can be found to increase with increasing notch depth. Fig. 5.2(b) shows the normalized net section fracture stress $\sigma^{\text{net}}_{\text{fr}}/\sigma_{\text{UTS}}$ as a function of the notch depth a/W. The net section fracture stress increases with increasing notch depth below $a/W = 0.6$. For the largest notch-depth with $a/W = 0.76$ (or $a/d = 8$), the normalized net section strength shows a decrease, but remains much larger than the unnotched fracture strength. For this notch depth, the uncracked ligament ($B = 5d$) contains only three or four load bearing struts. For comparison, we also plot the results for the unnotched samples with a width equal to the ligament width of the notched samples. A gradual weakening with decreasing sample width can be observed up to $B/d = 6$, below which the strength drops considerably. This weakening is attributed to free-edge effects resulting in a boundary layer of weak cells that contribute less to the load carrying capacity of the structure compared to the cells located in the interior of the sample (see Mangipudi and Onck (2011a) and

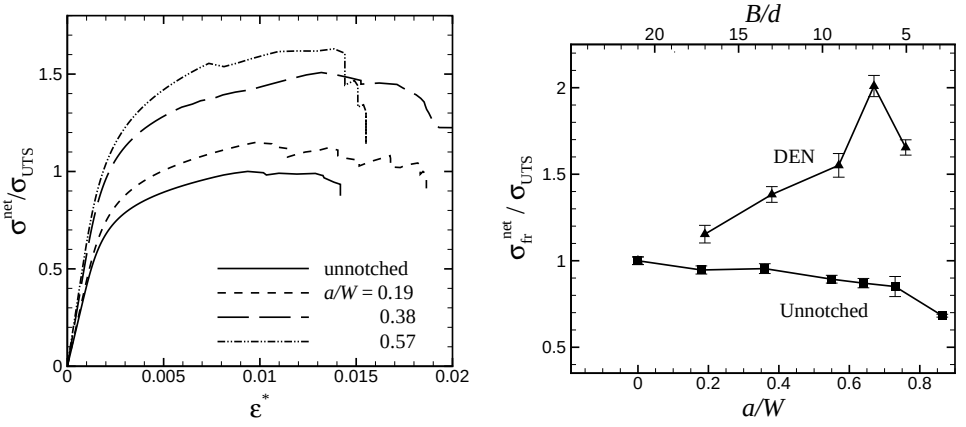

(a) (b)

Figure 5.2: (a) Typical stress-strain curves of DEN structures produced from the same initial structure. (b) The effect of notch depth on the uniaxial fracture strength in DEN structures.

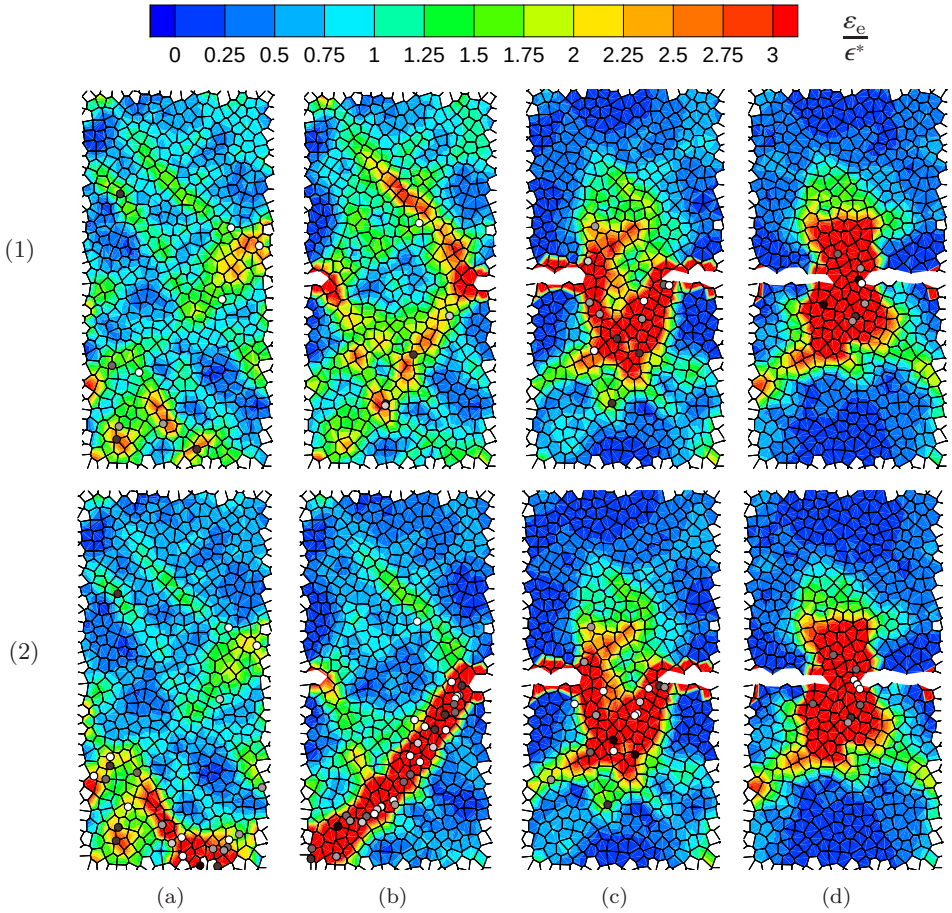

Figure 5.3: continued on next page...

Tekoğlu et al. (2010) for a recent review of size effects).

Fig. 5.3 shows the change in the strain and rotation fields as the crack length is changed. Note that the base structure is the same for all the crack lengths. The first two rows in Fig. 5.3 show the effective strain ε_e (see Eq. 5.1) normalized with the applied macroscopic strain ϵ^*. The local rotations ω_{12} (counterclockwise positive) are plotted in the third row. The damage locations (i.e. softening beam elements) are identified with filled circular symbols in gray scale with the black symbols representing complete strut failure. These are plotted at the peak of the individual structures (see Fig. 5.2(a)). The first column (a1 to a3) in Fig. 5.3 shows the fracture mech-

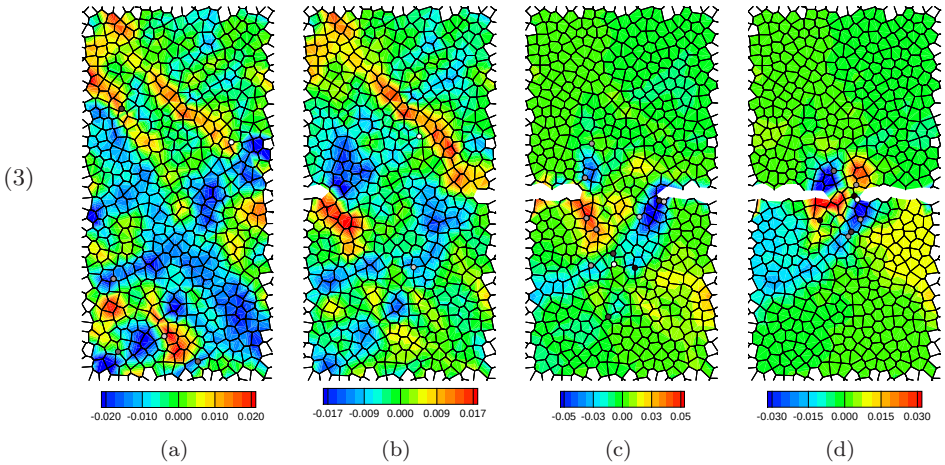

Figure 5.3: Strain maps plotted at the peak (first row) and the final failure mode (second row) for $a/W = 0, 0.19, 0.57$ and 0.76. Local rotation ω_{12} at the peak (bottom row) which corresponds to the strain maps in the top row. Note the different scale for each of the rotation plots. The stress-strain curves for some of the structures are shown in Fig. 5.2(a).

anism in the unnotched samples. In unnotched samples, preferential plastic strain development is followed by damage initiation and the final failure mode consists of localized fracture bands oriented close to 45° to the loading axis (Mangipudi and Onck, 2011a). A few such band-like regions with higher distortional strains and some damage can be found in Fig. 5.3(a1), one of which will become the final fracture band, see Fig. 5.3(a2). This is the lowest energy fracture mode for this structure. One of the cell level deformation modes consists of distortion combined with rotation (compare the strain fields in Fig. 5.3(a1) and the rotation fields in Fig. 5.3(a3)), as also observed experimentally by Bastawros et al. (2000). The rotation fields have to be accommodated elasto-plastically by the surrounding material[1]. Since the free-edges can easily accommodate rotations, these fields prefer to end up at the free-edges. In notched samples, three factors are found to be responsible for the notch strengthening exhibited in Fig. 5.2(b): (i) activation of fracture band(s) different from the lowest energy mode of fracture compelled to emanate from the notch(es) (compare columns 'a' and 'b' in Fig. 5.3), (ii) a decreasing material volume between the notch tips and thus a decreasing defect initiation probability at large a/W, see Figs. 5.3(c2)

[1] A certain minimum volume of material above and below these bands is required to accommodate the rotational fields. This produces a characteristic spacing between two neighbouring bands. A similar band spacing has also been reported by Bastawros et al. (2000) in three-dimensional samples under compression.

and (d2), and (iii) an increasing interaction and confinement of the counteracting notch tip rotation fields due to a decreasing ligament material volume resulting in constraints imposed on the deformation of the ligament volume at large a/W, see Figs. 5.3(c3) and (d3).

When a notch is introduced, the stress and strain concentrations at the notch tips will trigger deformation bands to form that emanate from these notch tips as shown in Fig. 5.3(b1). One of these notch tip deformation bands can lead to final failure either by connecting to a similar band from the other notch tip or by connecting to the opposing stress-free edge. Whether a notch tip band joins the other band or the stress-free boundary depends on the relative proximity of the stress-free boundary and the opposite notch tip. Figs. 5.3(a3) and (b3) show that in the unnotched and shallow-notched specimens the rotational fields nearly run across the specimen width and reach the specimen boundaries. For deeper notches, the stress-free boundaries are no more easily accessible for the notch tip fields and the strains and rotations are confined to the ligament. Under these conditions, small and intense rotation fields develop between the notch tips, which now provide another means of accommodating the applied strains (see Figs. 5.3(c3) and (d3)). Hence, the lowest energy mode in the presence of short notches is to connect to the stress-free specimen boundaries and for deeper notches it is by connecting the two notch tip deformation bands.

5.3.2 The effect of notch depth in CCP specimens

Central crack panels of fixed width (W/d) with elliptical notches (with $b/d = 1$) have been studied by varying the notch length (a/W). Typical stress-strain curves are shown in Fig. 5.4(a) and the variation in the net section fracture stress with the crack length is shown in Fig. 5.4(b). In this figure, results for the full CCP specimens are also added, from which the mean net section fracture stress of the symmetric samples deviates by less than 4%. The size effect in the fracture stress of unnotched specimens, shown in Fig. 5.2(b), is also added to Fig. 5.4(b) for comparison.The net section fracture strength exhibits an increase with the introduction of a short notch. With increasing notch depth, the net section fracture strength decreases and becomes lower than that of the unnotched specimen at large a/W. For the notched specimens, the net section strength decreases much more rapidly than the strength of unnotched samples. A large scatter for the deeper notches can be observed for the symmetric specimens (wide-flanged error bars in Fig. 5.4(b)), while the full CCP specimens (short-flanged error bars in Fig. 5.4(b)) show relatively less scatter. The large scatter is due to modelling a half specimen with symmetric boundary conditions. Due to the stochastic nature of the structures, the effective notch depth may sometimes be extended by an additional cell diameter if the notch tip just intersects a cell wall.

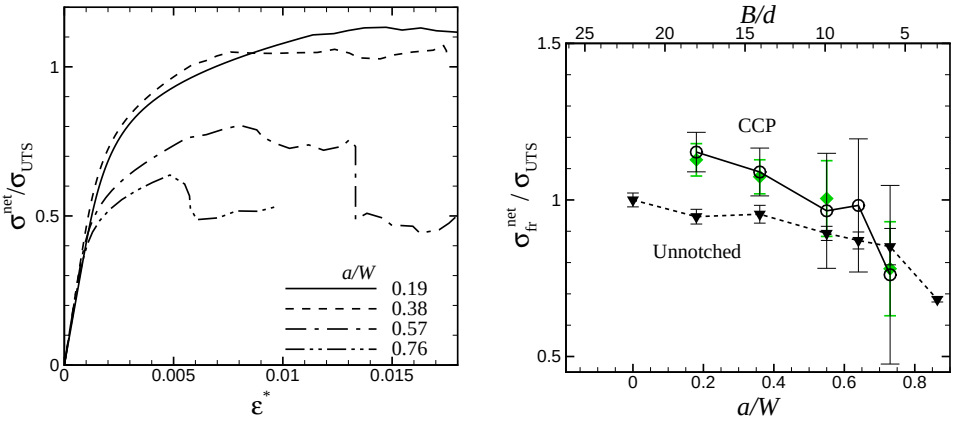

(a) (b)

Figure 5.4: (a) Typical stress-strain curves of (symmetric) CCP structures produced from the same initial structure. (b) The effect of notch depth on the net section fracture strength of CCP structures. The diamond symbols with short-flanged error bars in (b) represent the full CCP structures, while the circles correspond to symmetric CCP specimens.

This implies that the crack is extended by roughly two additional cell diameters, producing large scatter in case of deep notches.

Fig. 5.5 shows the strain and stress distribution[2] in CCP specimens as the notch depth is increased in the same initial structure. Note that the mirror images of the actually modelled CCP specimens have been added for better visualization (see Fig. 5.1(b)). For $a/W = 0.19$, the notch tip stress and strain fields in the elastic regime are not very different from the bulk behaviour (see Fig. 5.6). No notch tip stress and strain concentrations were observed, as the stress and strain levels near the notch tip are comparable to the local stress and strain variations away from the notch (see Figs. 5.5 and 5.6). It is apparent form the stress and strain maps shown in Fig. 5.5(a) that the effect of this short notch is only to introduce an additional pocket of elevated stress and to alter the location of the fracture band such that it emanates from the notch tip. Since now the fracture path is different from the lowest unnotched energy mode, the structure with a short notch is stronger than the unnotched structure. As the notches become deeper, two factors contribute to the lowering of the net section strength: (i) a stress/strain concentration at the notch tip and (ii) the increasing proximity of stress-free specimen boundaries. With increasing

[2]In contrast with chapter 4, strain maps in this chapter are produced by excluding the boundary cells, to avoid the error due to rigid rotations of the unconnected struts.

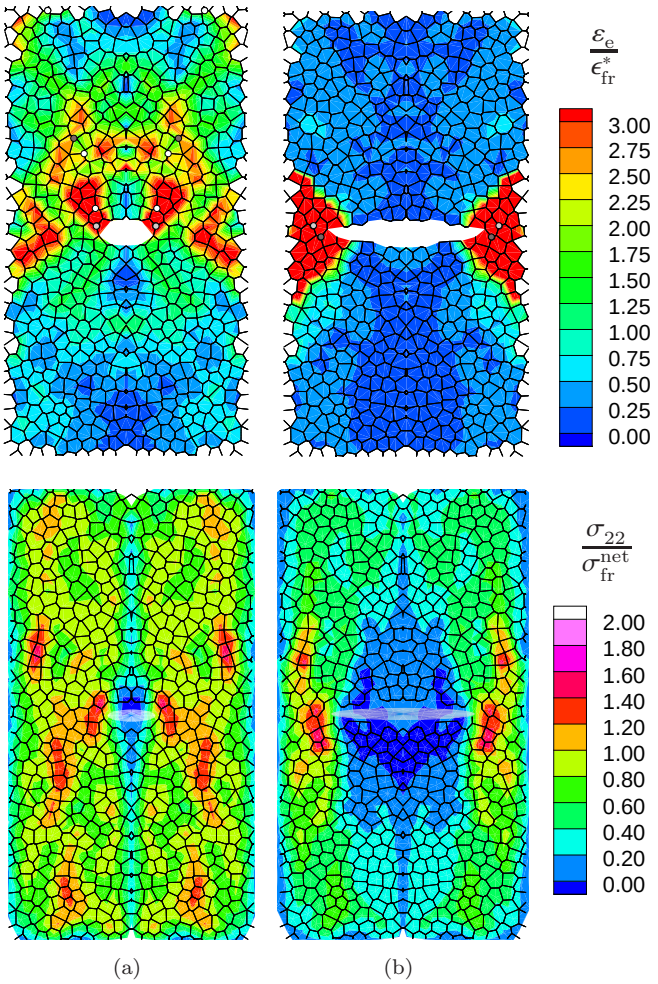

Figure 5.5: Normalized strain maps (top row) and stress maps (bottom row) for increasing crack lengths (with $a/W = 0.19$ and 0.55 for (a) and (b), respectively) plotted at their respective peak stress (see Fig. 5.4(a)). Mirror images of the half specimens are adjoined for better visualization.

notch depth, a clear elastic strain concentration emerges as shown in Fig. 5.6 and the maximum strain level increases with a/W. As a result, compared to the rest of the specimen volume, the ligament is highly stressed and localizes all deformation around the tips (see 5.5(b)). Due to this stress concentration, damage may be initiated at a lower macroscopic stress, decreasing the net section strength (see Fig. 5.4). In

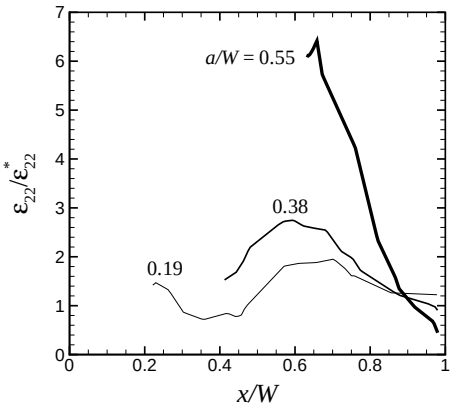

Figure 5.6: Elastic strain fields in front of the notch tip along the major axis of the notch in a CCP specimen. The center of the notch is at $x/W = 0$.

addition, the nearby stress-free edge also contributes to a decrease in the net section strength as the ligament size decreases, similar to the unnotched size effects.

5.3.3 The effect of notch tip radius

In Fig. 5.7, the effect of the notch tip radius on the net section fracture stress is plotted for DEN and CCP samples. The notch depth is fixed at $a/W = 0.55$ with $a/d = 12$. The minor axis b of the elliptical notch is changed from d to $12d$, where $b/d = 12$ produces a circular hole. The net section fracture stress of the notched structures is normalized with the peak stress of the unnotched samples. For DEN samples, the net section fracture stress of the smallest notch tip size (b/d=1) is larger than the unnotched specimen for the reasons discussed in section 5.3.1. Increasing the notch tip radius by changing the minor axis b of the elliptical crack (see Fig. 5.1(a)) produces only a minor increase in the net section fracture stress (see Fig.5.7). The sharp notches form inclined strain bands, while the circular notches tend to localize the strains in the ligament volume (results not shown). This confinement of strains in the ligament leads to a stronger interaction of the rotation fields near the circular notches, which slightly increased the peak stress. Also for CCP structures, the effect of the notch tip radius is to increase the strength, but the increase is very small (less than 10% in going from a sharp crack to a hole).

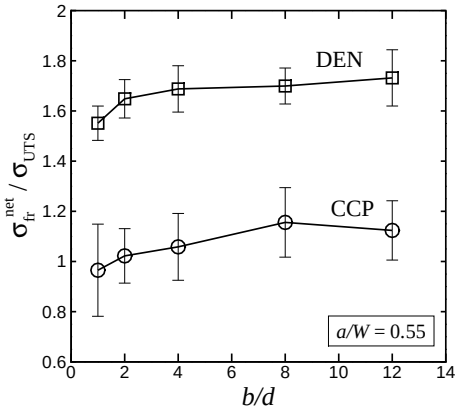

Figure 5.7: The effect of notch tip radius on the net section fracture stress.

5.3.4 Cell size effects

In the preceding sections, we have fixed the non-dimensional width W/d and varied the notch depth a/W. The range of structural dimensions are on the order of the cell diameter, for which cell size effects have been found to be exhibited by the unnotched structures (see Fig. 5.2(b)). Hence, the cell size may be expected to have an influence on the notch behaviour as well and must be distinguished from the role of the notch geometry alone. In order to investigate this, we have varied the non-dimensional width W/d between 10 and 34 (see the results in Fig. 5.8(a)). A clear cell size effect can be noticed here. For a given a/W, decreasing W/d shows an enhancement in the net section strength. This is true for all notch depths with the effect being stronger for deeper notches. By decreasing W/d we also decrease B/d for a given a/W, bringing the two notch tips closer together. The mechanisms found in section 5.3.1 that are connected to the reduced ligament volume (i.e. the geometric constraints imposed by cell level rotations and the reduced probability of finding a low strength defect) are expected to cause the net section strength enhancement with increasing W/d as well. Fig. 5.8(a) shows that the net section strength for $W/d = 34$ is nearly 27% lower compared to $W/d = 9$ at a notch depth of $a/W \approx 0.56$. This decreasing trend in the level of notch strengthening is expected to result in notch insensitive behaviour for $W \gg d$ as predicted by the continuum models for foams.

A similar analysis is conducted for CCP structures as well by varying W/d between 22 and 36, see Fig. 5.8(b). Unlike the DEN structures, no strong cell size effect has been observed in this case. The data for $W/d = 36$ showed less scatter, but nearly all the data points lie within the scatter bands of $W/d = 22$. Although a tendency

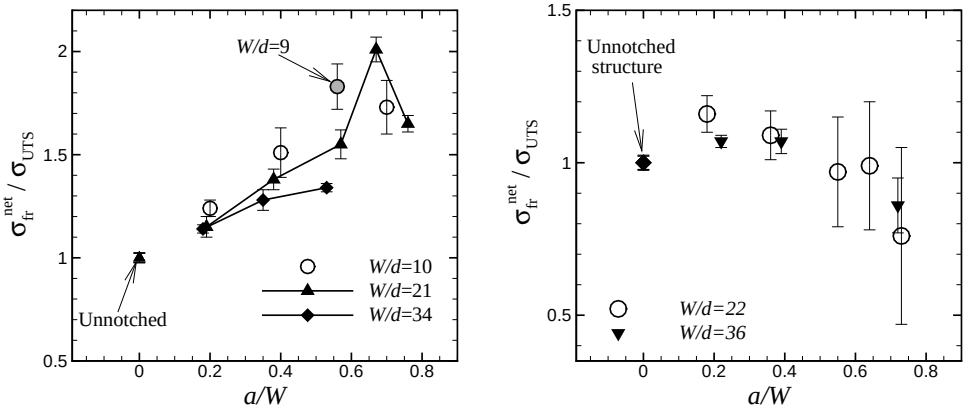

Figure 5.8: The effect of the number of cells in the specimen width on the notch behaviour in (a) DEN and (b) CCP structures.

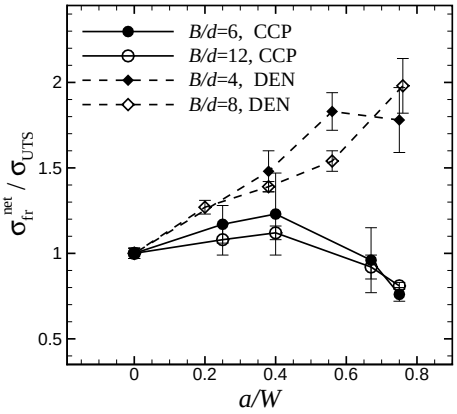

Figure 5.9: The effect of ligament width (B/d) on the notch behaviour.

towards notch insensitive behaviour seems to be emerging as W/d is increased, the large scatter makes it difficult to draw any firm conclusions.

The phenomenological model of Antoniou et al. (2004) explains the notch strengthening observed in three-dimensional DEN specimens of Alporas foams as a ligament size (B/d) effect[3]. Although a decreasing B/d has been identified to be partly respon-

[3] This model reduces to the one by Andrews and Gibson (2001a) by taking the flow stress enhancement factor to be equal 2 and the width of the shear zone to be equal to one cell size.

sible for the notch strengthening in Fig. 5.8(a), varying a/W at fixed W/d or varying W/d at fixed a/W, both lead to a simultaneous change of B/d and a/d, so that it remains unclear to which extent B/d or a/d contribute to strengthening. To investigate this further, we will now study the variation in net section strength as a function of the notch depth in Fig. 5.9 for two values of the non-dimensional ligament width B/d. Clearly, decreasing B/d from 8 to 4 increases the net section fracture stress of DEN structures for all notch depths except for $a/W = 0.76$. However, a strong dependence on a/W can still be seen despite the fact that B/d is fixed. In Fig. 5.10, the rotation fields clearly show the influence of the free-edge proximity (and thus the effect of a/W). Similar to Fig. 5.3, when the number of cells in the crack face is small (i.e. at small a/W) the bands reach out to the nearby free boundaries and for large a/d (i.e. at large a/W) they are confined within the specimen volume increasing the geometric constraint. Clearly, not only the number of cells between the notches (B/d) plays a role, but also the proximity of the cell edges to the notch tips (a/d) affects the strengthening behaviour.

Fig. 5.9 also shows a similar analysis for CCP structures. Also here, the B/d is kept constant for each curve while varying a/W. A similar effect as for a fixed W/d (Fig. 5.8(b)) can be seen also for a fixed B/d, although the direct effect of B/d is slightly stronger than that of a/d. The main trend for CCP, however, is that increasing the sample dimensions further eliminates existing cell size effects, leading to predominantly notch insensitive behaviour for CCP.

5.4 Discussion

Despite the two-dimensional nature of our model, our results on notch strengthening in DEN specimens are in excellent agreement with the notch strengthening observed in experiments on both open-cell and closed-cell foams (with samples containing a comparable number of cells in the width) as shown in Fig. 5.11. Similar trends have also been reported in a number of experimental findings (McCullough et al., 1999a; Motz and Pippan, 2001; Andrews and Gibson, 2001a; Antoniou et al., 2004; Combaz et al., 2010) and in finite element calculations (Andrews and Gibson, 2001b; Onck, 2001b). Accounting for strain hardening before damage in the present study predicts a slightly higher enhancement in the net section fracture strength in contrast to the previous numerical studies based on yield strength (Andrews and Gibson, 2001b; Onck, 2001b) for a comparable W/d. Different mechanisms of strength enhancement have been suggested in the literature. In specimens with relatively large number of cells in the diameter, Combaz et al. (2010) have recently shown in experiments-supported by continuum modelling-that the notch strengthening in notched cylindrical replicated Al foam specimens under tension is associated with stress triaxiality in

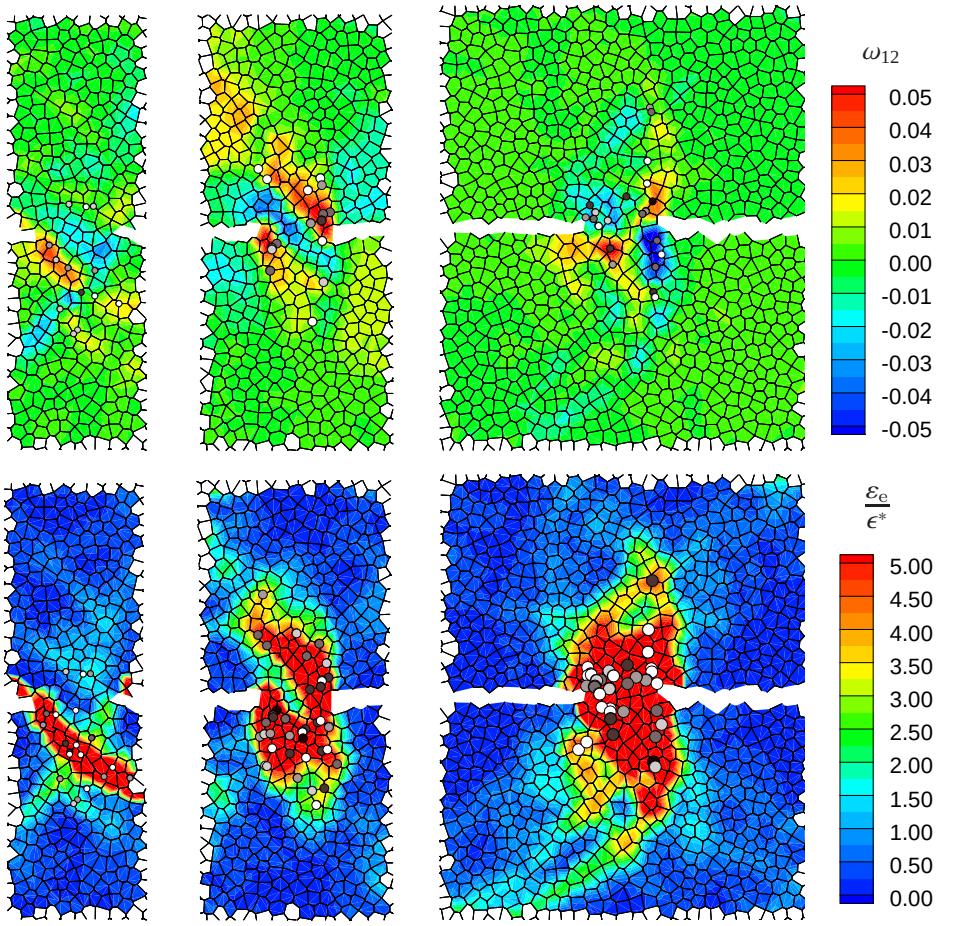

(a) $a/W = 0.38$ (b) $a/W = 0.56$ (c) $a/W = 0.76$

Figure 5.10: Local rotation (top row) and effective strain maps (bottom row) for structures with $B/d = 8$. The rotation maps are plotted at the peaks, while the strain maps are plotted beyond the peak but at different macroscopic strains showing the failure mode.

the ligament developed due to large strain hardening. In our simulations, an average stress triaxiality has been calculated as the area-weighted triaxiality of the triangles in the strain map in a circular region between the notch tips (results not presented here). Although we have observed a triaxiality larger than 0.5 (triaxiality in uniaxial tension in two-dimensional stress state) in front of the notch tips, no systematic variation in the amount of triaxiality, which is consistent with the net section variation

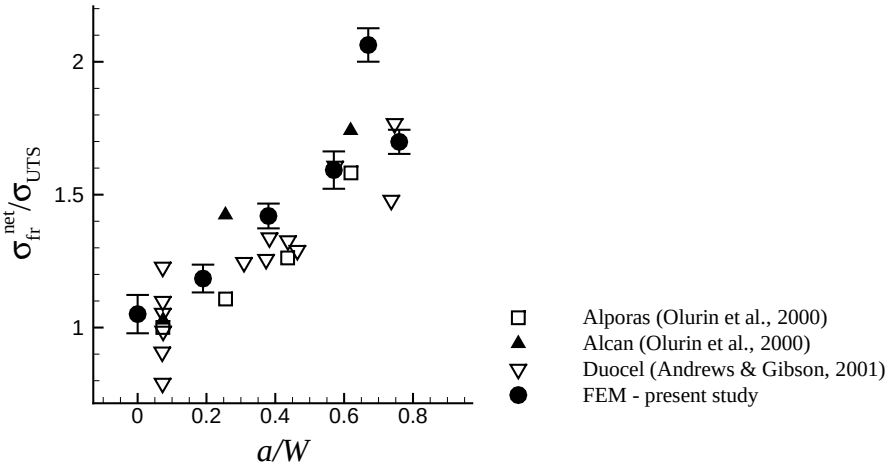

Figure 5.11: The effect of sharp notches on the tensile strength of DEN specimens: comparison with experiments.

in the Figs. 5.2(b), 5.8(a) and 5.9, could be observed. Clearly, the present specimens contained fewer number of cells in their width to be treated as continuum. For such specimens, a simple model based on the plastic yielding in the uncracked ligament and localized shear at the notch tip has been proposed (Antoniou et al., 2004; Andrews and Gibson, 2001a; Onck and Bastawros, 2000), which can be interpreted as a pure ligament size effect (B/d) with no dependence on either crack depth (a/d) or specimen geometry (a/W). These models correctly predict notch insensitivity at very large W/d and are able to describe the trend in the notch strengthening at small W/d. Our results on two-dimensional metal foams also suggest that the observed notch effects in DEN specimens are due to cell level interactions at the scale of the ligament. However, in our simulations we clearly observe a competition between these ligament-scale constraint effects (DEN) leading to strengthening and the weakening effect due to the proximity of the free edges. As a result, we found a dependence on both B/d and a/d (or a/W). Care must be taken, however, in directly extending these results to three-dimensions because out-of-plane constraints imposed by the three-dimensional structure might reduce the dependence on a/d.

The CCP specimens showed a slight increase in net section strength at small a/W in contrast to the experiments (Antoniou et al., 2004; Paul et al., 1999; Olurin et al., 2001). This increase has been attributed to the fact that the introduction of a notch changes the location of the deformation path, which is different from the lowest

energy mode of the unnotched specimen. The difference between the experimental and modelling results could be related to a higher defect probability in real foams due to the presence of brittle precipitates and cell wall defects. Furthermore, experimental observations for short cracks (small a/W) show that a fracture path forms through the center crack that stretches from one side of the sample diagonally to the other (Paul et al., 1999). In full CCP structures we have found exactly the same mode of diagonal failure, which is absent in Fig. 5.5(a) as a consequence of the symmetry considerations. However, the peak stress of the full and symmetric CCP structures was found to be nearly the same (within 4% error), which is due to the fact that the breaking of symmetry in the strain patterns only happens at large strain levels, beyond the levels at which the peak stress is attained. For larger values of a/W, no pronounced difference could be observed between the full and symmetric simulations.

5.5 Conclusions

The fracture behaviour of two-dimensional metal foams in tension is studied in the presence of notches and holes using a multiscale model incorporating power-law strain hardening and damage development leading to strut failure. The results are summarized in Fig. 5.12. Strong notch strengthening has been observed in DEN specimens which is related to the near-tip constraints imposed on the rotation fields. The devel-

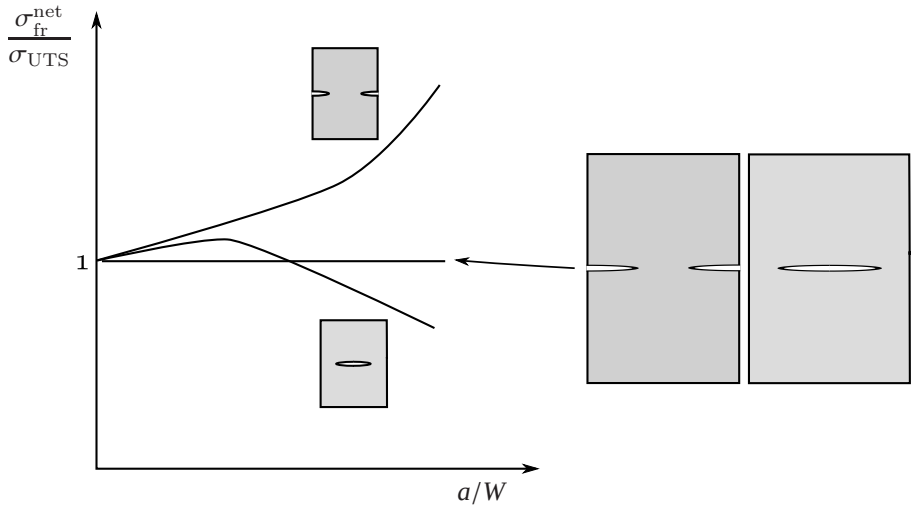

Figure 5.12: Summary of notch effects in two-dimensional foams showing the influence of the notch geometry and scale effects.

opment of these constraints is affected by the proximity of the stress-free specimen boundaries. On the other hand, a combination of stress concentration and stress-free boundaries produced slight notch weakening in CCP structures. The results exhibit a tendency to approach the continuum limit of notch insensitivity for both notch geometries as the sample size (relative to the cell size) is increased. Increasing the notch tip radius has been found to produce a marginal increase in the net section strength of both DEN and CCP samples.

Based on: K.R. Mangipudi and P.R. Onck – *"Tensile failure of two-dimensional quasi-brittle foams,"* submitted to Int. J. Solids Struct.

Chapter 6

Fracture strength of trabecular bone

When modern man builds large load-bearing structures, he uses dense solids: steel, concrete, glass. When nature does the same, she generally uses cellular materials: wood, bone, coral. There must be good reasons for it.

M.F. Ashby

In this chapter, we explore the influence of trabecular architecture and trabecular mechanical properties on the strength of cancellous bone. By using an elastic-fracturing material law in the model described in section 2.3, we will vary the relative density, trabecular cross-sectional profile, fracture strain and fracture energy. We will also explore how the net section strength is varied in a central crack configuration. We will interpret the effect of osteoporosis and two of its common clinical treatments on the fracture strength of trabecular bone. By comparing the results with a strain hardening solid material for an identical structure, we will discuss the differences in the damage accumulation behaviour between ductile and quasi-brittle solids.

6.1 Introduction

Trabecular bone, also known as cancellous or spongy bone, is a type of bone with an open-cell structure which accounts for up to 20% of the bone mass in humans. It is found in vertebrae, in the ends of long bones and in flat bones such as the pelvis. Its porosity may range from 30% to 90%. Loss of bone quality due to disease (Carbonare et al., 2005) or aging (Chappard et al., 2008; Chen et al., 2010) decreases bone strength increases fracture risk, leading to severe injuries or even death depending

on where the fracture occurs. It is now recognized that the mechanical properties of bone are dependent on both its density and microarchitecture. In this chapter, we will investigate the influence of bone material and microarchitectural changes on the fracture strength of trabecular bone.

Bone mass and form are acquired during childhood and adolescence, reaching a peak bone density around the age of 25 to 30 years in humans. The isotropic 'plate-like' dense trabecular network from the childhood gets adapted, resulting in aligned (anisotropic) trabeculae along the direction of mechanical stress/strain during adolescence (Chappard et al., 2008). This process is known as bone remodelling, which is a combination of two processes: resorption of metabolically or mechanically less competent bone followed by the formation of new bone elements advantageous to the local conditions. Bone mass is maintained due to an equilibrium of the two processes. Aging and disease may offset this equilibrium so that higher resorption rates lead to loss in bone mass and deterioration of microarchitecture. Age-related changes in bone are often reported in terms of a reduction in trabecular thickness, trabecular number (i.e. the number of trabeculae intersecting a unit line length on a two-dimensional cross section), connectivity density and bone density, while the trabecular spacing, number of free-ends and the structure model index (SMI) show an increase (Chappard et al., 2008; Chen et al., 2010). An increase in SMI represents a change in trabecular morphology from a 'plate-like' to a 'rod-like' shape (Hildebrand et al., 1999; Jinnai et al., 2002; Chen et al., 2010). The physiological mechanism responsible for this change in SMI during aging is a homogeneous resorption perforating the trabecular plates in the center. In males, connectivity changes are minimal due to aging while in postmenopausal osteoporotic women a much higher loss in connectivity occurs in addition to the loss in bone mass. The nature of the osteoporotic changes in microarchitecture are usually dependent on the metabolic/hormonal changes caused by either disease or other factors (Chappard et al., 2008). For example, in glucocorticoid (a class of steroid hormones) induced osteoporosis, trabeculae become thin preserving the connectivity, while alcoholism leads to a severe loss in connectivity in addition to trabecular thinning.

Common clinical treatment methods for osteoporosis includes antiresorptive and/or bone formation medication. Two common classes of antiresorptive medications are bisphosphonates (BP) and selective estrogen receptor modulators (SERM) (Benhamou, 2007; Migliaccio et al., 2007; Siegmund et al., 2010). Risedronate and alendronate are examples of BP, while raloxifene is the only available SERM at present. Both these classes of medication distinctly modify the bone matrix properties. The internal structure of the bone matrix consists of collagen fibrils and mineral. At this microscopic level, the mineralized collagen fibrils play an important role in determining the composite properties of the bone matrix. BP increase bone density

with a corresponding increase in trabecular thickness. This treatment will increase the trabecular elastic modulus by changing the state of cross-linking and collagen maturity, but does not alter the strength (Siegmund et al., 2010). The fracture energy is reduced increasing the brittleness. On the other hand, SERM is expected to bring a small reduction in the strength and modulus following a small degree of reduction in collagen maturity. However, a SERM treatment increases the peak strain and fracture energy (Siegmund et al., 2010). No significant change in the bone density (or the trabecular thickness) has been observed. Both these treatments do not cause a significant change in the trabeculae spacing and connectivity. Microcracks are present in trabeculae under both treatment conditions. In contrast to the antiresorptive agents, bone formation drugs (e.g. Teriparatide) increase connectivity by bone growth (Benhamou, 2007).

Clearly, the bone microarchitecture (i.e. the shape of the trabeculae and bone density) and the trabecular matrix properties are altered in osteoporosis and are also the target parameters in remedial treatments. Therefore, in this chapter, we will investigate the influence of trabecular shape, relative density, matrix fracture stress and critical fracture separation of the bone matrix under tension. Additionally, we also study the variation in net section strength in the presence of an internal crack, i.e. reflecting the central crack panel (CCP) as studied in chapter 5.

6.2 Simulation details

We use the same discrete modelling framework as presented in section 2.3. The material law in this case is initially linear-elastic until a critical fracture stress is reached, followed by a linear traction-separation relation during failure (see Fig. 6.1). Uniaxial calculations on unnotched specimens will be carried out with the boundary conditions as shown in Fig. 4.1, while the notch tests are performed on CCP specimens with the boundary conditions as specified in Fig. 5.1(b). Unless otherwise specified, the relative density is equal to 0.1, while the default values for the material parameters are $E = 70$ GPa, $\sigma_{\text{F}} = 41$ MPa and the normalized specific fracture energy $2E\Gamma_0/(\sigma_{\text{F}}^2 l_0) = 7$, where l_0 is the average strut length. The randomness of the structures is specified by $\delta = 0.9$ in the Voronoi generation. All the simulations presented in this chapter on unnotched specimens have been carried out with structures with 21 cells in the width and 40 cells in their height. The symmetric CCP specimens are 40 cells in height and 11 cells in their width so that $W/d = 22$ (see Fig. 5.1(b)).

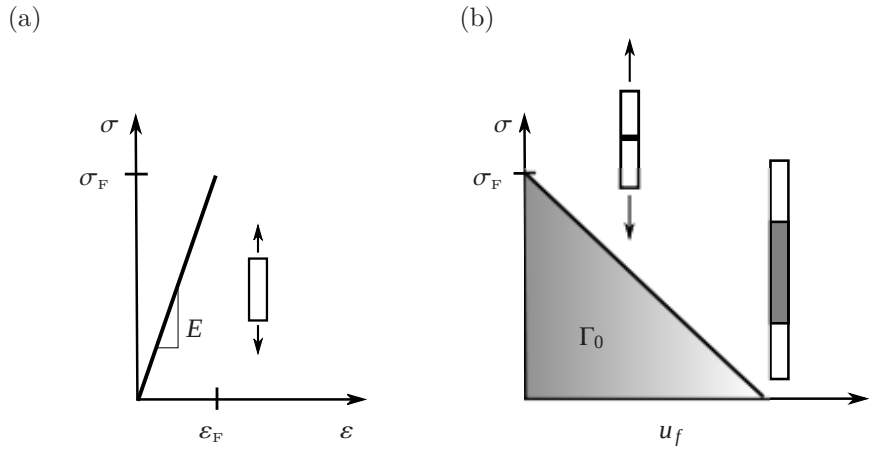

Figure 6.1: Constitutive behaviour of the strut material incorporated into the multiscale model shown in Fig. 2.3: (a) the elastic stress-strain law and (b) the traction-separation relation during failure.

6.3 Results

We start by examining the separate stages of deformation and failure during tensile loading. A typical stress-strain curve is shown in Fig. 6.2. The default elastic modulus and yield stress values are used, while the normalized fracture energy is taken to be 5. The macroscopic stress σ^* is normalized by the fracture strength of a regular hexagonal honeycomb made of the same material, $\sigma^*_{\mathrm{fr,HC}} = \sigma_{\mathrm{F}}(1/3)(\rho^*/\rho_{\mathrm{s}})^2$ (Gibson and Ashby, 1997). Three macroscopic regimes can be identified in the tensile response shown in Fig. 6.2: (i) a linear regime, approximately up to 'B', with no macroscopically permanent strain, (ii) a non-linear regime (from 'B' to 'C') where mechanisms responsible for determining the fracture path are operative, and (iii) a softening regime of crack formation and propagation leading to final failure (from 'C' onwards). Within the first regime, the structure is essentially elastic everywhere until the instant 'A', which marks the first damage initiation event (see the stress-strain curve in Fig. 6.2). During this first phase the local stress and strain distribution is more or less homogeneous over the structure, with a few exceptions where slightly larger local stresses and strains develop due to the structural randomness. Beyond this, a number of struts distributed uniformly over the structure begin to damage, although only a few of them have been found to continue the damage process. It may be noticed in Fig. 6.2(B) that only one strut dissipates greater than 1% of the total fracture energy by the end of the first regime at 'B'. After the instant 'B', the second regimes starts when accumulation of damage in the structure reduces the overall stiff-

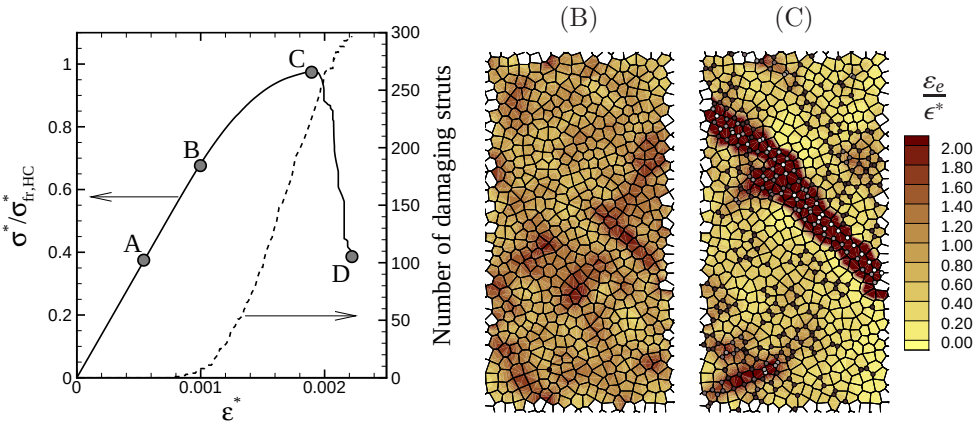

Figure 6.2: Failure of a quasi-brittle Voronoi honeycomb: Stress-strain curve and effective strain maps. The strain maps correspond to the labels on the stress-strain curve. The damage locations (which dissipated more than 1% of the total fracture energy) are labeled on the strain maps with (●) symbols in gray scale, where white denotes complete damage.

ness, and the stress-strain response becomes non-linear. This is an important regime as it hosts the processes that ultimately determine the peak stress of the structure. Among the various damaging struts, only a few struts show accelerated damage. These are generally situated in the regions that show locally higher strains as can be noted in strain map B of Fig. 6.2. The applied strains are accommodated in these regions assisted by local damage. Such a situation exists in different parts of the structure, where groups of damaging struts form active sites, interact and compete with each other in order to negotiate an energetically favourable failure path. During this phase, the stresses continue to increase and new struts will initiate and develop damage. When a collection of these regions link-up through accelerated damage development, the peak is reached and a fracture path is formed (see strain map C in Fig. 6.2). Later, strains localize in this fracture band and damage elsewhere will cease. The rest of the structure elastically unloads, while the macroscopic stress also reduces. A large crack forms from the right edge of the specimen, which finally leads to complete separation of the specimen.

In Fig. 6.3, we explore the stress-strain behaviour as a function of relative density. The underlying structure for the four relative densities is unchanged, while the strut thickness is adjusted in tune with the relative density. The material properties are also kept constant at the default values. All the unnormalized stress-strain curves for different relative densities collapse onto nearly one curve when the macroscopic stress σ^* is normalized with $\sigma^*_{\mathrm{fr,HC}}$ and the macroscopic strain ϵ^* with

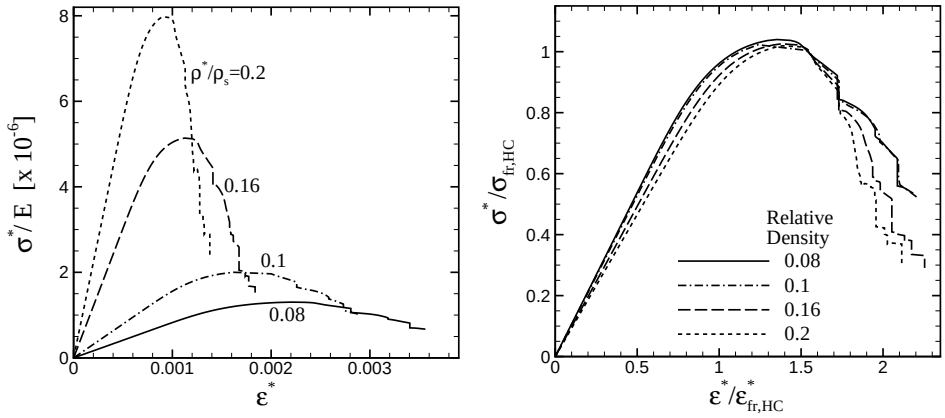

Figure 6.3: Macroscopic stress-strain curves for different relative densities with fixed material properties and for the same Voronoi structure (left). The figure on the right shows the same data after normalization.

$\epsilon^*_{\mathrm{fr,HC}} = (2/9)(\sigma_{\mathrm{F}}/E)(\rho^*/\rho_{\mathrm{s}})^{-1}$, suggesting that the peak stress and peak strain scale with a power 2 and -1, respectively, with the relative density. Note that the peak strain of ductile structures also exhibits a similar scaling exponent (see chapter 4). A small deviation from collapsing onto a single curve along with clear ordering with relative density can be observed. The reason for this deviation is related to the increase in the overestimation of the relative density due to overlapping struts at the junctions.

The results presented above have been conducted on structures with constant thickness along the strut length. In the following, we vary the strut thickness t along the length according to

$$\frac{t(\xi)}{t_0} = p\xi^4 + \xi^2 + 1, \quad \xi = (2x/L - 1) \quad \text{and} \quad \xi \in [-1, 1], \tag{6.1}$$

where t_0 is the strut thickness at the middle of the strut and p is a constant (Gong et al., 2005). The default solid material properties and randomness parameter will be used.

Stress-strain curves for the structures with $p = 10$ and 86 are compared with a uniform strut cross section in Fig. 6.4 for a constant relative density equal to 0.1. A small degree of non-uniformity introduced for $p = 10$ has increased the elastic modulus compared to the uniform strut cross-section. This is due to the fact that the bending stiffness first increases with increasing non-uniformity and then decrease below a specific midspan thickness depending on the strut profile (Harders et al., 2005).

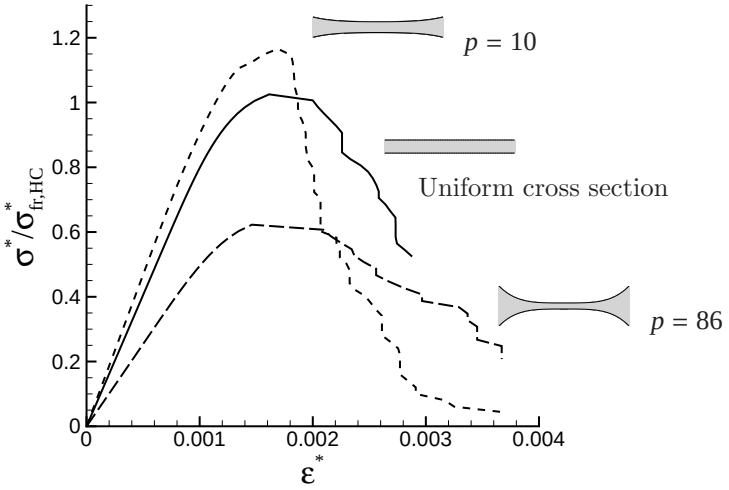

Figure 6.4: Influence of non-uniform cross section on the stress-strain curves. Next to each curve, the corresponding strut profiles are shown in the same scale.

For mildly non-uniform struts, the increased strut thickness near the triple point gives a stiffer response in bending due to the cubic dependence of bending stiffness on the thickness. However, in case of highly non-uniform strut profiles (corresponding to $p = 86$ for instance), for which the strut thickness decreases very rapidly producing a long slender strut with thick ends, the thinner cross-section becomes responsible for a low bending stiffness. Fig. 6.4 also shows that the fracture stress first increases with the strut profile parameter p and then decreases. Apparently, there is no significant variation in the peak strain for the values of p chosen in this study. The mechanism of strength variation with strut profile can be best explained by considering a regular hexagonal structure. The peak stress of a regular hexagonal honeycomb with an elastic-fracture material behaviour shows a similar behaviour for the two strut non-linearities. The critical locations of damage initiation are $0.145l_0$ and $0.165l_0$ from the triple point for $p = 10$ and 86, respectively. The strut thickness at the critical locations is $0.88t_{\text{uni}}$ and $0.56t_{\text{uni}}$ for $p = 10$ and $p = 86$, respectively, with t_{uni} referring to the thickness of a uniform strut of a regular hexagonal honeycomb with the same relative density. For the $p = 86$ profile, the curvature developed at the critical location is nearly 3.7 times the curvature at the critical location of the $p = 10$ profile for a given macroscopic stress. Hence, the critical fracture strain will be reached for a lower macroscopic stress in the highly non-uniform case with $p = 86$. Note, however, that no correction for the relative density has been made here to account for the material redundancy due to overlapping struts at a triple point. As

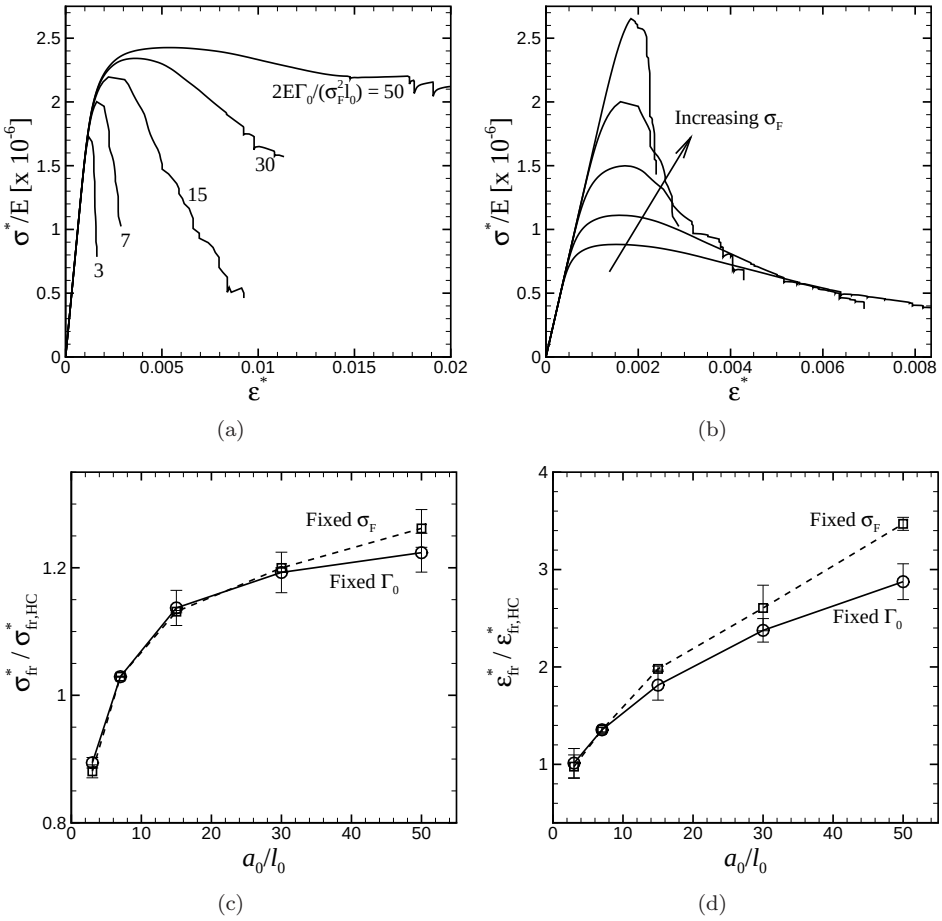

Figure 6.5: Influence of the fracture energy and fracture stress on the stress-strain behaviour is shown in (a) and (b), respectively. The fracture stress σ_F is fixed in (a), while the specific fracture energy Γ_0 is fixed in (b). The relative density and the Voronoi structure are the same for all the stress-strain curves shown in (a) and (b). Variation in the peak stress and peak strain with a_0/l_0 is shown in (c) and (d), respectively.

the strut thickness near the triple point increases with increasing non-uniformity in strut thickness, the uncorrected relative density is an overestimation. This overestimated relative density might also be partly responsible for the decrease in peak stress displayed by the highly non-uniform struts in Fig. 6.4.

In Fig. 6.5, we study the peak stress behaviour by independently varying the

fracture energy and the fracture stress. Here, the elastic modulus E is fixed at the default value. The fracture stress is kept constant at $\sigma_{\text{F}} = 41$ MPa in Fig. 6.5(a) and Γ_0 is varied by changing the fracture displacement u_f (see Fig. 6.1). In Fig. 6.5(b), the fracture energy is $\Gamma_0 = 7(1/2)(41\times10^6)^2(l_0/E)$, corresponding to a normalized fracture energy equal to 7 in Fig. 6.5(a). By changing the fracture stress σ_{F} at constant fracture energy, u_f is adjusted accordingly (see Fig. 6.1). The relative density is 0.1 in both cases and the cellular architecture is the same for all the curves in Fig. 6.5(a) and Fig. 6.5(b). As the fracture energy is increased in Fig. 6.5(a), the second regime is extended, increasing both the peak stress and the peak strain. It can also be seen that with increasing fracture energy a shallow unloading slope results. When the fracture stress is increased in Fig. 6.5(b), the peak stress and peak strain also clearly increase. The second regime gets shortened and the overall softening slope becomes steeper with increasing fracture stress. To capture the effect of both the fracture stress and fracture energy, we introduce the dimensionless parameter

$$\frac{a_0}{l_0} = \frac{2E\Gamma_0}{\sigma_{\text{F}}^2 l_0}, \tag{6.2}$$

which is a measure of the ratio of the fracture energy to the stored elastic energy in a strut, and is related to the fracture displacement through $a_0 = u_f E/\sigma_{\text{F}}$. The normalized peak stress and peak strain are plotted as a function of the parameter a_0/l_0 in Fig. 6.5(c) and Fig. 6.5(d), respectively. Clearly, both the peak stress and peak strain increase monotonically with a_0/l_0. At small values of a_0/l_0, a quick enhancement in the strength is achieved with increasing a_0/l_0, while for large values of a_0/l_0, the gain in the strength has slowed down. The peak stress values for both the fixed σ_{F} and fixed Γ_0 cases coincide (except for $a_0/l_0 = 50$). In contrast, the normalized peak strain shows a gradual increase in both cases for the range of a_0/l_0 values considered here. The normalized peak strain for the fixed σ_{F} case is larger than the fixed Γ_0 case, with the difference increasing with a_0/l_0, showing a 17% larger value for the largest a_0/l_0 value. By fitting the data in Figs. 6.5(c) and 6.5(d) to power-law relations, we find that $\sigma^*_{\text{fr}}/\sigma^*_{\text{fr,HC}}$ shows a (weak) power 0.15 dependence on a_0/l_0 (excluding the data for $a_0/l_0 = 50$), while $\epsilon^*_{\text{fr}}/\epsilon^*_{\text{fr,HC}}$ shows a slightly larger power of 0.4. The dependence of the peak on a_0/l_0 can be explained by considering the damage process during the second regime. When a strut starts to damage in a loaded structure, the energy for the dissipative damage process will be provided by the stored elastic energy in the structure. If the stored elastic energy is more than the required fracture energy, a brittle failure results with a local snap back instability. On the other hand, when the stored elastic energy is less than the fracture energy, additional energy has to be supplied to the system beyond damage initiation by increasing the macroscopic stress in order to continue the damage. As a result, the

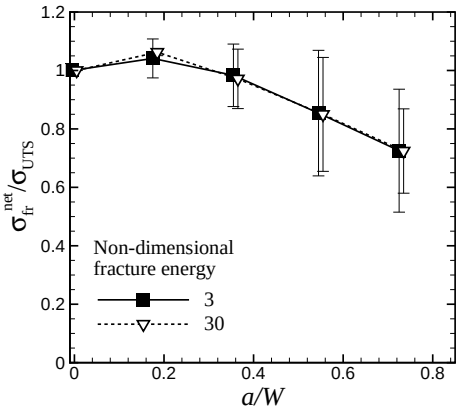

Figure 6.6: Net section strength variation with notch depth in quasi-brittle structures with a centrally located crack. Note that the data points are slightly separated horizontally for clarity.

peak stress and peak strain increase with increasing ratio of the fracture energy to the elastic energy (a_0/l_0).

We have also analysed central crack panels by varying the crack length to specimen width ratio a/W for two fracture energy values for constant specimen width W/d (d being the cell size). The boundary conditions are shown in Fig. 5.1. The non-dimensional specific fracture energies $2E\Gamma_0/(\sigma_f^2 l_0)$ are taken to be 3 and 30 in each set. The net section strength normalized by the peak stress of unnotched structures σ_{UTS} is shown in Fig. 6.6. The net section strength is slightly (about 5%) larger than the unnotched structure at $a/W = 0.18$, after which a clear and monotonic decrease in net section strength can be observed as the notch depth is increased. The observed notch weakening can be attributed to the contribution from two factors: the stress-free boundaries and the notch tip stress concentration. A stress concentration at the notch tip is responsible for the early onset of damage along with an accelerated damage development in the ligament region. The stress-free specimen boundaries also contribute to a reduction in the net section stress in a similar fashion as in the case of unnotched specimen size effects (Mangipudi and Onck, 2011b), see Fig. 5.4(b) and the related discussion in section 5.3.2. The large scatter for deeper notches is a consequence of using a symmetric half-specimen in the CCP configuration. The normalized net section strength at all notch depths has not been affected even when the fracture energy is changed by one order of magnitude.

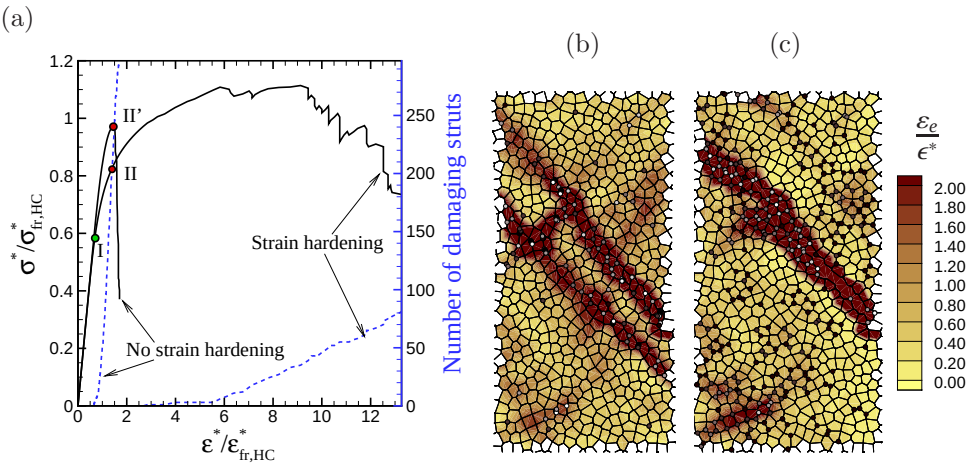

Figure 6.7: (a) Comparison of stress-strain behaviour in quasi-brittle and ductile structures. The solids lines are the stress-strain curves and the dashed lines represent the number of damaging struts. The normalized effective strain maps in (b) and (c) show the fracture modes in structures with and without strain hardening, respectively, plotted at the end of the corresponding stress-strain curves in (a). The damage locations (which dissipated more than 1% of the total fracture energy) are labeled on the strain maps with (●) symbols in gray scale, where white denotes complete damage.

6.4 Discussion

6.4.1 Comparison of fracture in ductile and quasi-brittle foams

The present study also reveals some interesting differences between the damage behaviour of quasi-brittle and ductile foams. The difference arises because of the presence of strain hardening. Fig. 6.7 compares the stress-strain curve from Fig. 6.2 with that of a ductile strain hardening solid material, for the same Voronoi realization. In this case, the critical fracture stress of the non-hardening solid is equal to the yield stress of the ductile solid. The ductile solid has a strain hardening exponent of $N_s = 0.1$ and a fracture strain $\varepsilon_F = 0.08$, while the relative density, elastic modulus and the normalized specific fracture energy are the same as the non-hardening structure. Although damage in a couple of struts has already occurred before the instant (I), no gross differences in the stress and strain distribution have been found. Roughly beyond this instance, the stress-strain curve becomes non-linear for both structures. In the quasi-brittle structure, a quick increase in the number of damaging struts can be observed (see the dashed line in Fig. 6.7). The increment in the

local effective stress (not shown here) between (I) and (II) is more or less uniform in the ductile structure due to the stress redistribution facilitated by strain hardening, while in the quasi-brittle structure the incremental local effective stress distribution between (I) and (II') is inhomogeneous with unloading in some parts. It is also interesting to note that for the ductile foam the damage evolution is guided by the preceding plastic deformation and damage appears only in the regions that showed prior preferential plastic strain growth (see Fig. 6.7(b)). In contrast, a large number of struts from various parts of the specimen begin to damage (about 150 struts at the peak) in the quasi-brittle structure, see Fig. 6.7(c). From the location of struts with accelerated damage aiding the formation of the final crack in both specimens (see the white symbols on the strain maps in Fig. 6.7), it can be noticed that the same structural features contribute to local failure, while the differences in the damage evolution and the final fracture mode are dependent on the stress redistribution caused by strain hardening.

In notched specimens, the net section strength behaviour in quasi-brittle structures is qualitatively similar to what has been found in ductile structures at large a/W ratios (see Figs. 5.4(b) and 6.6). However, the increase in net section strength with the introduction of a short crack is not very significant in quasi-brittle structures. This is due to the presence of a large number of damaging struts distributed across the structure, which assist in finding a low energy alternate fracture mode.

6.4.2 Influence of osteoporosis treatments on bone mechanical properties

The results of the present study can provide a qualitative insight into the influence of osteoporosis medications, although the numerical values of the material and structural parameters used in this study do not coincide with those of bone. Osteoporosis and the clinical treatments for its cure usually accompany a simultaneous change in more than one material and architectural parameter. The basic and easily detectable change in osteoporosis is the bone density, i.e. the relative density of the cellular structure. A decrease in the bone density alone will strongly decrease the strength of the bone, as the strength scales with the relative density power 2 (see Fig. 6.3). This is in line with the high fracture risks predicted with a decreasing bone density due to aging (Ross et al., 1990; Carbonare et al., 2005). The thinning of trabecula during aging and postmenopause osteoporosis will make the trabecular profile highly non-linear. As can be seen from Fig. 6.4, a large decrease in the thickness of the trabecula in the middle can reduce the strength by as much as a factor of two for a fixed relative density. For a simultaneous decrease in the relative density and the trabecular profile change, the cumulative influence of the two will greatly reduce

both the bone stiffness and the strength. The increase in the relative density and the trabecular matrix modulus through BP treatment compared to the affected bone can help to recover some of the strength loss due to osteoporosis (see Figs 6.3 and 6.5(c)). However, as the trabecular connectivity is also lost during osteoporosis, restoring the relative density would not be sufficient to recover the strength completely (Silva and Gibson, 1997b). Besides these influences, BP treatment will decrease the energy during fracture which will in turn decrease the strength and brittleness (see Figs. 6.5(c) and 6.5(d)). However, since the effect of fracture energy on bone strength is rather weak, the relative density displays the dominating effect with a power 2 dependence on strength and hence ultimately leads to a gain in the trabecular bone strength during BP treatment. On the other hand, the relatively low strength-restoring effect of SERM treatment is mainly due to the increase in the specific fracture energy as this treatment produces a negligible variation in relative density and only a small reduction in the modulus and strength of the trabecular matrix.

6.5 Concluding remarks

We have explored the influence of relative density, non-uniform strut profile and the fracture energy on the damage and failure in quasi-brittle Voronoi structures to gain insight into the effects of osteoporosis medication on bone strength. A power-law dependence on the relative density has been observed for the peak stress with an exponent of 2. A highly non-uniform strut profile reduces the strength of quasi-brittle foams, while a small deviation from a uniform profile may be beneficial for both strength and stiffness. The influence of both the specific fracture energy and the critical fracture stress are captured in a non-dimensional parameter which is the ratio of the fracture energy to the stored elastic energy at the onset of fracture. The peak stress and peak strain show a relatively weak power-law dependence on this parameter with powers of 0.15 and 0.4, respectively.

The qualitative effect of the commonly available clinical treatments for osteoporosis on the trabecular bone strength can be inferred from the results of the present study. From the perspective of bone stiffness and strength, the BP treatment may be beneficial compared to SERM with the danger of increased bone brittleness.

Chapter 7

Summary

The aim of science is to seek the simplest explanation of complex facts.

Alfred North Whitehead

The central goal of this thesis is to investigate the role of strut microstructure and cellular architecture on the macroscopic mechanical behaviour and to explore the microstructural mechanisms of deformation and fracture in cellular metals. To pursue this, we have developed, in chapter 2, a discrete multiscale model of two-dimensional metal foams incorporating strain hardening and material damage.

Mechanism-based scaling relations for cellular solids in the literature have been very successful in predicting the power-law dependence of the macroscopic stiffness and plastic strength on the foam's relative density. Strain hardening has either been neglected or has been spatially limited to a highly localized hinge at the strut junctions at small deformations. We have shown in chapter 3 that strain hardening significantly influences the triple point deformation. In a strut with uniform cross section, a redistribution of stress occurs away from the triple point due to strain hardening, advancing the yield-front towards the middle of the strut length. This modifies the curvature development along the strut length compared to a perfectly-plastic strut, and has been found to play a important role in damage initiation in chapter 4.

For a non-uniform strut cross section studied in chapter 3, initial yielding takes place in a location along the strut away from the strut junction. The symmetric profile of the elastic-plastic front during bending-dominated loading suggests a necking down mechanism observed in ductile foams. When the local conditions are such that the strut also experiences significant axial loading, a shear band formation is predicted by the highly asymmetric elastic-plastic boundary profile, agreeing well with the experimental findings.

In ductile foams, struts reorient towards the tensile loading axis. Even for a perfectly-plastic solid material, a small amount of overall hardening has been introduced by the increased axial loading of reorienting struts due to finite deforma-

tions, which we refer to as "geometric hardening". For a strain hardening material this interacts synergistically with the intrinsic strain hardening producing a higher macroscopic hardening, with the effect being larger at low relative densities. Random foams feature one more additional contribution to the hardening from the mesostructure, originating from the progressively increasing number of yielding strut junctions at different locations, which significantly enhances the overall foam hardening coefficient. The results from the simulations from chapter 3 yield a relation for the overall hardening as a linear combination of intrinsic material hardening and 'geometric hardening' with an inverse dependence on the relative density and square root dependency on the yield strain.

In chapter 4, we have studied the relation between damage processes at different scales and the uniaxial peak stress behaviour, along with their dependence on the material and structural parameters. In regular hexagonal structures, failure initiates in all the inclined struts simultaneously due to symmetry. The peak stress is reached in the regular structures almost immediately after the first fiber fractures. In random structures, a pre-peak damage regime has been found. In this regime, strain hardening competes with softening due to damage, influencing the initiation and accumulation of damage and the peak formation. Both the failure strain and failure stress are enhanced when the strain hardening exponent is increased, which is connected to an increase in the damage onset strain. Microstructurally, the mechanism of delayed damage onset in high strain hardening materials has been identified to be the slowdown in curvature development at the strut junctions, postponing the initiation of fiber failure. On the other hand, damage in fibers initiates at lower macroscopic strains when the relative density is increased, resulting in a lower fracture strain. The fracture stress has been found to have a power 2 scaling with relative density, similar to the plastic collapse strength. In a study on the effect of heat treatment, the fracture strength of a structure with T6 tempered solid properties is higher compared to a structure with annealed properties at the expense of ductility. Brittle precipitates have shown a deleterious effect on both the overall fracture strength and ductility.

In the second part of chapter 4, we investigated the effect of structural randomness and anisotropy on the fracture stress and fracture strain. In highly random structures, in which the cell size distribution is broad, the macroscopic strains are accommodated primarily by the large cells which are few in number, while the small cells which make up the majority are subjected to relatively low strains. This inhomogeneous deformation lowers the fracture strain with increasing randomness. When loaded in the rise direction, we found that anisotropic structures are stiffer and stronger but less ductile (lower fracture strain) compared to loading in the transverse direction. Analytical expressions for yielding in affinely-scaled regular hexagonal structures have

been found to capture the fracture stress dependence on relative density and cell shape in the irregular structures. When the specimen size is well decreased, the influence of the stress-free specimen boundaries produces a weakening size effect in fracture stress, while it increases the damage onset strain and the strain to fracture.

By a careful analysis of the data from various parametric studies from the first and second parts of chapter 4, we found that the macroscopic fracture stress normalized with the solid's fracture stress is proportional to the second power of relative density. We found the dimensionless proportionality constant for the (architecturally) isotropic structures to be nearly the same as the prefactor in the scaling of a perfectly brittle regular hexagonal honeycomb. When structural anisotropy is introduced by an affine scaling, the prefactor has to be multiplied by the affine scaling ratio. On the other hand, the overall fracture strain has been found to be proportional to the overall strain hardening exponent (given by the relation found in chapter 3), the solid's fracture strain and the inverse of the relative density. In this case, the prefactor has to be divided by the affine scaling ratio to account for structural anisotropy.

In chapter 5, we have investigated the net section strength of samples with pre-existing cracks. In accordance with previous studies on double edge notch specimens, we found that the net section strength increases with the crack length to specimen width ratio a/W. Since changing the crack length in fixed width specimens is also associated with a simultaneous change in the ligament width B/d (d being the cell size), we have also studied the effect of a/W for a fixed ligament width B/d, with the aim to identify which one of the two is responsible for the observed notch strengthening. Interestingly, we found that both the ligament width and the crack length play a role in notch strengthening. By analysing the notch tip deformation fields, we conclude that notch strengthening in two-dimensional metal foams is indeed due to a cell size effect: both the number of cells in the crack face a/d (but not a/W) as well as the ligament width B/d are responsible for the notch strengthening. We have also studied the influence of the stress-free specimen boundaries in central crack specimens, which showed a mild notch weakening behaviour due to the stress concentration at the notch tips and the proximity of the stress-free specimen boundaries. The net section strength has been observed to be nearly insensitive to the notch tip radius.

In chapter 6, we have studied the mechanical behaviour of trabecular bone with the aim to investigate the influence of osteoporosis and two of its clinical treatments on the mechanical properties. We have explored the effect of relative density, non-uniform strut cross section, fracture stress and fracture energy. While the relative density showed the strongest influence on the trabecular bone strength with a power-law exponent of 2, the strength of the bone is also found to be sensitive to the non-uniformity in the trabecular profile. The effect of the fracture energy and the fracture stress has been shown to be captured by the ratio of the fracture energy and

the stored elastic energy at the onset of fracture. The fracture strength, normalized by the fracture strength of a purely brittle regular honeycomb, increases when this ratio is increased. From the known influence of the osteoporosis treatments using either bisphosphonates (BP) or selective estrogen receptor modulators (SERM) on the trabecular matrix material properties and cellular architecture, our results suggest that the BP treatment results in a larger recovery of the bone strength than the SERM treatment, while slightly enhancing the brittleness.

The difference between chapter 6 and the preceding chapters 4 and 5 is that the constitutive law for the trabecular matrix does not include strain hardening. Damage is found to initiate in a large number of struts distributed throughout the structure in quasi-brittle structures, while a plasticity-guided damage initiation has been observed in ductile structures.

We would like to conclude by providing guidelines for the design of metal foams based on our results. One of the technological relevances is the influence of the strain hardening on the plateau region of the compressive stress-strain curve discussed in section 3.2.2. For impact absorption applications, the characteristics of a good absorber are a constant plateau stress, keeping the impact forces constant at a low level and a high densification strain for high energy absorption. An unwanted effect is that the strain hardening during the plateau stage increases the stresses, and thus increasing the impact forces on the body to be protected. Hence, a low strain hardening foam may be recommended for such applications. Strain hardening in commercial foams can also influence the failure behaviour as these foams contain unwanted microstructural features in the form of inclusions, second phase particles and grain boundary precipitates. We found in chapter 3 that the increase in stresses in the neighbourhood of a triple point due to strain hardening can possibly trigger failure in precipitates located away from the triple point.

We also found that a higher strain hardening capacity enhances the overall strength and ductility. However, this is achieved in our simulations with the critical fracture strain kept constant. Strain hardening in a metal is usually enhanced by increasing the resistance to the motion of dislocations, typically by the addition of solute atoms, addition of precipitate forming elements and altering precipitate morphology in the strut microstructure either through heat treatment or by other alloy additions. Most of these processes are also known to reduce the critical fracture strain on which the foam's peak strain has been found to have a primary dependence (Eq. 4.8). In addition, brittle grain-boundary precipitates severely knock-down the foam strength and ductility and must be avoided. When fastening foam components requires the introduction of multiple notches or holes, for a higher strength it is recommended to configure them sufficiently close enough mimicking the DEN configuration. Similarly, notches or holes should be placed away from stress-free specimen boundaries. It is

expected that our results on material and structural influences on fracture strength and ductility, summarized in Figs. 4.22 and 5.12, can assist in constructing guidelines for material selection and design, and can help in improving alloy composition and foam processing technologies.

Samenvatting

Metaalschuimen zijn materialen die enerzijds een microstructuur bevatten op de microschaal (de schaal van de celwanden), maar anderzijds ook een mesoscopische microstructuur hebben (op de schaal van de celstructuur). Deze micro- en mesoscopische structuren zijn gevoelig voor het productieproces van het schuim en beïnvloeden bovendien de mechanische eigenschappen. Het doel van dit proefschrift is te onderzoeken wat de invloed van deze twee structuurniveaus op de mesoscopische vervormings- en schademechanismen is en te begrijpen hoe deze de macroscopische mechanische eigenschappen beïnvloeden. Voor dit doel werd een meerschalig model van een tweedimensionaal schuim ontwikkeld, waarbij Voronoi tessellaties werden gebruikt om de cellulaire structuur te beschrijven. Door nauwgezet de plastische vloeigrens in de celwanden op cellulair niveau te volgen, kon een geometrisch verstevigingsmechanisme worden geïdentificeerd dat hand in hand gaat met het intrinsieke verstevigen van het metaal zelf. Tevens kon worden vastgesteld dat de competitie tussen versteviging door plastische deformatie en verzwakking ('softening') door inwendige schadeontwikkeling belangrijk is bij het bepalen van de macroscopische treksterkte en ductiliteit. Met toenemende intrinsieke versteviging wordt de ontwikkeling van buiging in de celwanden afgeremd en daarmee ook de initiatie van schade, hetgeen de treksterkte en ductiliteit van het schuim verhoogt. In onregelmatige celstructuren met een brede verdeling van celgrootten is de mesoscopische deformatieverdeling niet-uniform, hetgeen leidt tot een verlaging van de ductiliteit. Voor schuimen met een structurele anisotropie werd aangetoond dat het schuim sterker en minder ductiel is in de trekrichting parallel aan de grootste cel-as, vergeleken met een trekrichting daar loodrecht op. Op basis van de numerieke berekeningen konden eenvoudige uitdrukkingen worden afgeleid die de macroscopische versteviging, treksterkte en ductiliteit beschrijven in termen van de materiaaleigenschappen van de celwanden en geometrische parameters van de cellulaire architectuur. Ook is er onderzoek gedaan

naar het effect van interne scheuren op de treksterkte. Vastgesteld werd dat proefstukken met rand-kerven ('edge-notches') verstevigingsgedrag vertonen, terwijl proefstukken met inwendige scheuren juist verzwakken. Ten slotte is in dit proefschrift ook het falen van poreus bot ('trabecular bone') onderzocht, waarbij de effectiviteit van twee klinische behandelmethoden voor osteoporose werden vergeleken.

Appendices

A Closed-form expressions for the stress resultants during plastic loading

If we define $\beta = E/\sigma_{\rm Y}$ then the power law hardening relation in Eq.(2.11) can be rewritten to take the form

$$\sigma = \frac{\varepsilon}{|\varepsilon|}\sigma_{\rm Y}\left(1+\beta|\varepsilon^{p}|\right)^{N}. \tag{A-1}$$

The same form of hardening law can be reduced to linear hardening by replacing β with $H/\sigma_{\rm Y}$ and $N = 1$.

After evaluating the integral and some algebraic manipulation, Eq.(2.16) takes the form

$$\begin{aligned} M(\bar{\varepsilon},\kappa) \;=\; & -b\Bigg\{\frac{\sigma_{\rm Y}}{(N+1)\beta\kappa}\Big[-\Big(1+\beta(|\bar{\varepsilon}+\kappa\tfrac{t}{2}|-\varepsilon_{\rm Y})\Big)^{N+1}\,\tfrac{t}{2}-\big(1+\beta(|\bar{\varepsilon}-\kappa\xi^{\ominus}|-\varepsilon_{\rm Y})\big)^{N+1}\,\xi^{\ominus}\Big] \\ & + \frac{\sigma_{\rm Y}\ \mathrm{Sign}(\bar{\varepsilon}+\kappa\frac{t}{2})}{(N+1)(N+2)\beta^{2}\kappa^{2}}\Big[\Big(1+\beta(|\bar{\varepsilon}+\kappa\tfrac{t}{2}|-\varepsilon_{\rm Y})\Big)^{N+2}-\Big(1+\beta(|\bar{\varepsilon}-\kappa\xi^{\ominus}|-\varepsilon_{\rm Y})\Big)^{N+2}\Big] \\ & + E\Big[\frac{\kappa}{3}\left(\xi^{\ominus 3}-\xi^{\oplus 3}\right)+\frac{\bar{\varepsilon}}{2}\left(\xi^{\oplus 2}-\xi^{\ominus 2}\right)\Big] \\ & + \frac{\sigma_{\rm Y}}{(N+1)\beta\kappa}\Big[\Big(1+\beta(|\bar{\varepsilon}-\kappa\xi^{\oplus}|-\varepsilon_{\rm Y})\Big)^{N+1}\,\xi^{\oplus}-\Big(1+\beta(|\bar{\varepsilon}-\kappa\tfrac{t}{2}|-\varepsilon_{\rm Y})\Big)^{N+1}\,\tfrac{t}{2}\Big] \\ & + \frac{\sigma_{\rm Y}\ \mathrm{Sign}(\bar{\varepsilon}-\kappa\frac{t}{2})}{(N+1)(N+2)\beta^{2}\kappa^{2}}\Big[\Big(1+\beta(|\bar{\varepsilon}-\kappa\xi^{\oplus}|-\varepsilon_{\rm Y})\Big)^{N+2}-\Big(1+\beta(|\bar{\varepsilon}-\kappa\tfrac{t}{2}|-\varepsilon_{\rm Y})\Big)^{N+2}\Big]\Bigg\}, \end{aligned} \tag{A-2}$$

where $\xi^{\oplus}$ and $\xi^{\ominus}$ are given by Eq.(2.15).

The axial force is obtained in a similar fashion to give

$$\begin{aligned} P(\bar{\varepsilon},\kappa) \;=\; & -b\Bigg\{\frac{\left[1+\beta(|\bar{\varepsilon}+\kappa\tfrac{t}{2}|-\varepsilon_{\mathrm{Y}})\right]^{N+1}-\left[1+\beta(|\bar{\varepsilon}-\kappa\xi^{\ominus}|-\varepsilon_{\mathrm{Y}})\right]^{N+1}}{(1+N)\beta\kappa} \\ & + E\left[\frac{\kappa}{2}\left(\xi^{\ominus 2}-\xi^{\oplus 2}\right)+\bar{\varepsilon}\left(\xi^{\oplus}-\xi^{\ominus}\right)\right] \\ & + \frac{\left[1+\beta(|\bar{\varepsilon}-\kappa\tfrac{t}{2}|-\varepsilon_{\mathrm{Y}})\right]^{N+1}-\left[1+\beta(|\bar{\varepsilon}-\kappa\xi^{\oplus}|-\varepsilon_{\mathrm{Y}})\right]^{N+1}}{(1+N)\beta\kappa}\Bigg\}. \end{aligned} \tag{A-3}$$

However, these equations cannot be directly employed for a perfectly plastic material. For this case, the force and moment have to be obtained separately so that

$$M(\bar{\varepsilon},\kappa) = b\tfrac{\sigma_{\mathrm{Y}}}{2}\left[\mathrm{Sign}(\bar{\varepsilon}+\kappa\tfrac{t}{2})(\tfrac{t^2}{4}-\xi^{\ominus 2})+\mathrm{Sign}(\bar{\varepsilon}-\kappa\tfrac{t}{2})(\xi^{\oplus 2}-\tfrac{t^2}{4})\right]+\tfrac{2b}{3}E\kappa\left(\xi^{\oplus 3}-\xi^{\ominus 3}\right) \tag{A-4}$$

and

$$P(\bar{\varepsilon},\kappa) = -b\sigma_{\mathrm{Y}}\left[\mathrm{Sign}(\bar{\varepsilon}+\kappa\tfrac{t}{2})(\xi^{\ominus}+\tfrac{t}{2})+\mathrm{Sign}(\bar{\varepsilon}-\kappa\tfrac{t}{2})(\xi^{\oplus}-\tfrac{t}{2})\right]+\tfrac{b}{2}E\kappa\left(\xi^{\oplus 2}-\xi^{\ominus 2}\right). \tag{A-5}$$

B Generalized viscoplastic strain rates

By using $\dot{\kappa}^{vp} = \dfrac{d\dot{\theta}^{vp}}{dx}$ and $\dot{\theta}^{vp} = \dfrac{d\dot{v}^{vp}}{dx}$, we can integrate Eq.(2.35) and Eq.(2.36) along the length of the beam which gives

$$l\dot{\bar{\epsilon}}_1^{vp} = \int_x \dot{\varepsilon}_0\left(\frac{P}{P_0}\right)^n dx = \dot{\varepsilon}_0\left(\frac{P}{P_0}\right)^n x + c_1, \tag{B-6a}$$

$$\dot{\theta}^{vp} = \frac{\dot{\kappa}_0}{{M_0}^n(n+1)V}\left(M_2 - V(l-x)\right)^{n+1} + c_2 \tag{B-6b}$$

and

$$\dot{v}^{vp} = \frac{\dot{\kappa}_0}{M_0^n(n+1)(n+2)V^2}\left(M_2 - V(l-x)\right)^{n+2} + c_2 x + c_3 \tag{B-6c}$$

where c_1, c_2 and c_3 are integration constants. For $V \neq 0$, these constants are evaluated by substituting the boundary conditions

$$\begin{array}{lcll} \dot{e}_1^{vp} & = & l\dot{\bar{\epsilon}}_1^{vp} & = \; l\dot{\varepsilon}_0\left(P/P_0\right)^n, \\ \dot{e}_2^{vp} & = & (\dot{v}_1 - \dot{v}_2 + \dot{\phi}_1 l) & = \; C_A({T_1}^{n+2} - {T_2}^{n+2}) + C_B({T_1}^{n+1}), \\ \dot{e}_3^{vp} & = & (\dot{\phi}_2 - \dot{\phi}_1)l & = \; C_B({T_2}^{n+1} - {T_1}^{n+1}), \end{array} \tag{B-7}$$

where

$$C_A = \frac{\dot{\kappa}_0}{(n+1)(n+2)}\left(\frac{M_0}{V}\right)^2, \quad C_B = \frac{l\dot{\kappa}_0}{n+1}\frac{M_0}{V}, \quad T_1 = \frac{M_2 - Vl}{M_0}, \quad \text{and} \quad T_2 = \frac{M_2}{M_0}.$$

When $V = 0$, i.e. for pure bending, $\dot{e}_1$ is neglected and for the bending related generalized strains we have

$$\dot{e}_2^{vp} = -\dot{\kappa}_0 \frac{l^2}{2}\left(\frac{M_2}{M_0}\right)^n, \tag{B-8}$$

and

$$\dot{e}_3^{vp} = \dot{\kappa}_0 l^2 \left(\frac{M_2}{M_0}\right)^n. \tag{B-9}$$

C Perzyna-type viscoplastic framework with damage

In this section, an elasto-plastic Euler-Bernouli beam element for inelastic problems involving hardening/softening problems has been developed within a Perzyna type viscoplastic framework. This element formulation enables a quick and easy implementation of the dissipative mechanisms in a beam model compared to the classical inelasticity algorithms. Unloading conditions follow naturally, eliminating the need to track the history explicitly. The yield surface is followed closely, in an average sense, depending on the exponent of the over-stress function. When modelling rate-independent processes the computational costs associated with this method are high, especially when required to follow the yield surface closely. This poses a limitation on the size of the structure and the degree of nonlinearities to be modelled.

A viscoplastic formulation using an overloading function defined in terms of yield surface has been proposed by Zienkiewicz and Cormeau (1974). This method has been applied by Badiche et al. (2000) to model a Nickel foam with a phenomenological plasticity approach. To improve the estimate of the viscoplastic strains (and thereby the computational efficiency), a rate tangent formulation based on the effective stress was devised by Pierce et al. (1984). These rate sensitive versions can be used to model rate-independent plasticity in the limit that the creep exponent goes to infinity. This method has been adopted to study void growth for rate sensitive materials (Koplik and Needleman, 1988; Becker et al., 1988) and interface delamination (Abdul-Baqi and Van der Giessen, 2001) and ductile fracture (Scheyvaerts, 2008) with rate-independent plasticity. A combination of the above two ideas will be utilized in this work. For 2D beams, we follow a lumped plasticity model along similar lines as used in a rate-independent formulation given by Marante et al. (2004) and Croce et al. (2003). A Perzyna-type viscoplastic framework (Zienkiewicz and Cormeau,

1974) to model the plastic deformation and failure of beams will be developed here. The yielding of the beam is given by the interaction diagram in the stress resultant space. The various available yield functions during plasticity and fracture will be summarized after establishing the general framework.

C.1 General framework for a two-dimensional EB beam

Let the lumped yield function (or the interaction diagram) at the nodes be written as a function of the stress resultants $\mathbf{s}$ and the dissipation energy μ:

$$\boldsymbol{\psi}(\mathbf{s}, \boldsymbol{\mu}) = \mathbf{0} \tag{C-1}$$

where

$$\boldsymbol{\psi} = \begin{Bmatrix} \psi_1(P, M_1, D_1) \\ \psi_2(P, M_2, D_2) \end{Bmatrix}. \tag{C-2}$$

Here $D_i, i = 1, 2$ are the damage parameters which are functions of the dissipated energy μ_i at the nodes.

The Perzyna viscoplastic (generalized) strain rates are given by Zienkiewicz and Cormeau (1974)

$$\dot{\mathbf{e}}^{vp} = \langle \boldsymbol{\Psi}(\boldsymbol{\psi}) \rangle \frac{\partial \boldsymbol{\psi}}{\partial \mathbf{s}}^T \boldsymbol{\lambda} \tag{C-3}$$

where

$$\boldsymbol{\lambda} = \begin{Bmatrix} \lambda_1 \\ \lambda_2 \end{Bmatrix}, \tag{C-4}$$

$$\frac{\partial \boldsymbol{\psi}}{\partial \mathbf{s}} = \begin{bmatrix} \dfrac{\partial \psi_1}{\partial P} & \dfrac{\partial \psi_1}{\partial M_1} & 0 \\ \dfrac{\partial \psi_2}{\partial P} & 0 & \dfrac{\partial \psi_2}{\partial M_2} \end{bmatrix}. \tag{C-5}$$

The overloading function $\boldsymbol{\Psi}$ is defined such that

$$\langle \Psi_i \rangle = \begin{cases} (\psi_i + 1)^{n_c} & \text{if } \psi_i \geq 0, \\ 0 & \text{if } \psi_i < 0. \end{cases} \tag{C-6}$$

The plastic dissipation energy $\boldsymbol{\mu}$ is defined as

$$\dot{\boldsymbol{\mu}} = \begin{Bmatrix} \dot{\mu}_1 \\ \dot{\mu}_2 \end{Bmatrix} = \mathbf{L}\boldsymbol{\lambda} \quad \text{and} \quad \mu_j = \int_{t_i}^{t_f} \dot{\mu}_j dt \tag{C-7}$$

with

$$\mathbf{L} = \begin{bmatrix} l_1 & 0 \\ 0 & l_2 \end{bmatrix} = \begin{bmatrix} P\dfrac{\partial \psi_1}{\partial P} + M_1 \dfrac{\partial \psi_1}{\partial M_1} & 0 \\ 0 & P\dfrac{\partial \psi_2}{\partial P} + M_2 \dfrac{\partial \psi_2}{\partial M_2} \end{bmatrix}. \tag{C-8}$$

Here t_i and t_f correspond to the moment of initiation and completion of fracture.

C.2 Yield function

Form of the yield functions

Ilyushin has derived a yield surface for plates and shells and has been used by many authors (for example, Burgoyne and Brennen (1993b,a)). To this yield surface many approximations and improvements have been made. Crisfield uses one such approximation and improved it to include initial 'fiber-yield' (Crisfield, 1997) which will be used here.

Initial fiber yield at any point along the length of the beam occurs for the *generalized stress* state given by the surface (Crisfield, 1997)

$$\psi \equiv \left(\frac{P}{P_0}\right)^2 + 3m\frac{P}{P_0}\frac{M}{M_0} + \frac{9}{4}\left(\frac{M}{M_0}\right)^2 - 1 = 0. \tag{C-9}$$

Assuming a perfectly plastic behaviour and that the yield stress has been reached at all the points through the thickness, a simple form of the yield surface can be obtained (Crisfield, 1997) for 'full-section yield':

$$\psi \equiv \left(\frac{P}{P_0}\right)^2 + m\frac{M}{M_0} - 1 = 0 \tag{C-10}$$

Here $m = M/|M|$ and P_0 and M_0 are the yield force and moments. For developing a multisurface plasticity framework for a rate-independent formulation, Crisfield proposed an approximation of the above equation including the gradual 'fiber yield' Crisfield (1997):

$$\psi \equiv \left(\frac{P}{P_0}\right)^2 + \frac{m}{\alpha\sqrt{3}}\frac{P}{P_0}\frac{M}{M_0} + \frac{1}{\alpha^2}\left(\frac{M}{M_0}\right)^2 - 1 = 0 \tag{C-11}$$

with $\alpha \in [2/3, 1]$ with increasing plastic curvature fitted to the moment/plastic curvature relation in pure bending via

$$\alpha = 1 - 0.4\exp\left(-2.6\sqrt{\frac{Et\kappa_p}{3\sigma_Y}}\right). \tag{C-12}$$

For a 'full-section yield' surface represented by Eq.(C-10), the direction of loading is

given by

$$\frac{\partial \boldsymbol{\psi}}{\partial \mathbf{s}} = \begin{bmatrix} \frac{2P}{P_0^2} & \frac{m_1}{M_0} & 0 \\ \frac{2P}{P_0^2} & 0 & \frac{m_2}{M_0} \end{bmatrix}. \tag{C-13}$$

Evolution of the yield surface with strain hardening/softening

Isotropic evolution of the yield surface can be achieved through different techniques. One method is to make the yield force and yield moment (P_0 and M_0, respectively) a function of a suitably defined hardening/softening parameter (Marante et al., 2004). Thus these major and minor axes of the yield surface evolve with the plastic strains and change the yield surface size. This technique has been adopted during the plastic deformation of the beam using the evolution equations for $P_0(\bar{\varepsilon}, \kappa, N)$ and $M_0(\bar{\varepsilon}, \kappa, N)$ as given in Mangipudi et al. (2010).

Another method is to define a hardening/softening parameter to directly scale the size of the yield surface (Ehrlich and Armero, 2005; Armero and Ehrlich, 2006). Such a modification to the yield function in Eq.(C-10) would look like

$$\psi(P, M, D) \equiv \left(\frac{P}{P_0}\right)^2 + m\frac{M}{M_0} + D - 1 = 0. \tag{C-14}$$

This function is used during damage with P_0 and M_0 corresponding to the initial failure surface. If the fracture energy per unit area of cross section is Γ_0, then a damage parameter is defined as

$$D_i = \frac{\mu_i}{\Gamma_0 t}, \tag{C-15}$$

where the dissipation energy μ is given by Eq.(C-7).

Bibliography

Abdul-Baqi, A., Van der Giessen, E., 2001. Indentation-induced interface delamination of a strong film on a ductile substrate. Thin Solid Films 381, 143.

Alkhader, M., Vural, M., 2008. Mechanical response of cellular solids: Role of cellular topology and microstructural irregularity. Int. J. Eng. Sci. 46, 1035–1051.

Aly, M. S., Almajid, A., Nakano, S., Ochiai, S., 2009. Fracture of open-cell copper foams under tension. Mater. Sci. Eng. A 519 (1-2), 211–213.

Amsterdam, E., 2008. Structural performance and failure analysis of Aluminium foams. Ph.D. thesis, University of Groningen, The Netherlands.

Amsterdam, E., Babcsán, N., De Hosson, J. Th. M., Onck, P. R., Banhart, J., 2006a. Fracture behaviour of metal foam made of recycled MMC by the melt route. Mat. Trans. 47 (9), 2219–2222.

Amsterdam, E., De Hosson, J. Th. M., Onck, P. R., 2006b. Failure mechanisms of closed-cell aluminium foam under monotonic and cyclic loading. Acta Mater. 54, 4465–4472.

Amsterdam, E., De Hosson, J. Th. M., Onck, P. R., 2008a. On the plastic collapse stress of open-cell aluminum foam. Scripta Mater. 59, 653–656.

Amsterdam, E., de Vries, J. H. B., De Hosson, J. Th. M., Onck, P. R., 2008b. The influence of strain-induced damage on the mechanical response of open-cell aluminum foam. Acta Mater. 56 (3), 609–618.

Amsterdam, E., Goodall, R., Mortensen, A., Onck, P. R., De Hosson, J. Th. M., 2008c. Fracture behavior of low-density replicated aluminum alloy foams. Mater. Sci. Eng. A 496, 376–382.

Amsterdam, E., Onck, P. R., De Hosson, J. Th. M., 2006c. Fracture and microstructure of open cell aluminium foam. J. Mater. Sci. 40, 5813–5819.

Amsterdam, E., Van Hoorn, H., De Hosson, J. Th. M., Onck, P. R., 2008d. The influence of cell shape anisotropy on the tensile behaviour of open-cell aluminum foam. Adv. Eng. Mater. 10 (9), 877–881.

Andrews, E. W., Gibson, L. J., 2001a. The influence of crack-like defects on the tensile strength of an open-cell aluminum foam. Scripta Mater. 44, 1005–1010.

Andrews, E. W., Gibson, L. J., 2001b. The influence of cracks, notches and holes on the tensile strength of cellular solids. Acta Mater. 49, 2975–2979.

Andrews, E. W., Gioux, G., Onck, P. R., Gibson, L. J., 2001. Size effects in ductile cellular solids. Part II: experimental results. Int. J. Mech. Sci. 43, 701–713.

Andrews, E. W., Sanders, W., Gibson, L. J., 1999. Compressive and tensile behaviour of aluminium foams. Mater. Sci. Eng. A 270, 113–124.

Antoniou, A., Onck, P. R., Bastawros, A., 2004. Experimental analysis of compressive notch strengthening in closed-cell aluminum alloy foam. Acta Mater. 52, 2377–2386.

Armero, F., Ehrlich, D., 2006. Numerical modelling of softening hinges in thin euler-bernoulli beams. Computers & Structures 84, 641–656.

Ashby, M. F., Evans, A., Fleck, N. A., Gibson, L. J., Hutchinson, J. W., Wadley, H. N. G., 2000. Metal Foams: A Design Guide. Butterworth-Heinemann, Oxford.

Badiche, X., Forest, S., Guibert, T., Bienvenu, Y., Bartout, J. D., Ienny, P., Croset, M., Bernet, H., 2000. Mechanical properties and non-homogeneous deformation of open-cell foals: application of the mechanics of cellular solids and of porous materials. Mat. Sci. Eng. A 289, 276–288.

Banhart, J., 2001. Manufacture, characterization and application of cellular metals and metal foams. Prog. Mater. Sci. 46, 559–632.

Banhart, J., Baumeister, J., 1998. Deformation characteristics of metal foams. J. Mater. Sci. 33, 1443–1440.

Bart-Smith, H., Bastawros, A. F., Mumm, D. R., Evans, A. G., Sypeck, D. J., Wadley, H. N. G., 1998. Compressive deformation and yielding mechanisms in cellular al alloys determined using x-ray tomography and surface strain mapping. Acta Mater. 46 (10), 3583–3592.

Bastawros, A. F., Bart-Smith, H., Evans, A. G., 2000. Experimental analysis of deformation mechanisms in a closed-cell aluminum alloy foam. J. Mech. Phys. Solids 48 (3), 301–322.

Bastawros, A. F., Evans, A. G., 2000. Deformation hetrogeneity in cellular al alloys. Adv. Eng. Mater. 2 (4), 210–214.

Beals, J. T., Thompson, M. S., 1997. Density gradient effects on aluminium foam compression behaviour. J. Mater. Sci. 32 (13), 3595–3600.

Becker, R., Needleman, A., Richmond, O., Tvergaard, V., 1988. Void growth and failure in notched bars. J. Mech. Phys. Solids 36 (3), 317–351.

Benhamou, C., 2007. Effects of osteoporosis medications on bone quality. J. Bone Spine 74, 39–47.

Benouali, A., Froyen, L., Dillard, T., Forest, S., N'guyen, F., 2005. Investigation on the influence of cell shape anisotropy on the mechanical performance of closed cell aluminium foams using micro-computed tomography. J. Mater. Sci. 40 (22), 5801–5811.

Burgoyne, C., Crisfield, M. A., 1990. Numerical integration strategy for plates and shells. Int. J. Num. Meth. Eng. 29, 105–121.

Burgoyne, C. J., Brennen, M. G., 1993a. Calculation of elasto-plastic rigidities using the exact ilyushin yield surface. Int. J. Solids Struct. 30 (8), 1133–1145.

Burgoyne, C. J., Brennen, M. G., 1993b. Exact ilyushin yield surface. Int. J. Solids Struct. 30 (8), 1113–1131.

Carbonare, L. D., Valenti, M. T., Bertoldo, F., Zanatta, M., Zenari, S., Realdi, G., Cascio, V. L., Giannini, S., 2005. Bone microarchitecture evaluated by histomorphometry. Micron 36, 609–616.

Chappard, D., Baslé, M., Legrand, E., Audran, M., 2008. Trabecular bone micro architecture: A review. la microarchitecture de l'os trabéculaire: une revue. Morphologie 92, 162–170.

Chen, C., Fleck, N. A., Lu, T. J., 2001a. The mode I crack growth resistance of metallic foams. J. Mech. Phys. Solids 49, 231–259.

Chen, C., Lu, T. J., 2001. A phenominological framework of constitutive modelling for incompressible and compressible elasto-plastic solids. Int. J. Solids Struct. 49, 231–259.

Chen, C., Lu, T. J., Fleck, N. A., 1999. Effect of imperfections on the yielding of two dimensional foams. J. Mech. Phys. Solids 47, 2235–2272.

Chen, C., Lu, T. J., Fleck, N. A., 2001b. Effect of inclusions and holes on the stiffness and strength of honeycombs. Int. J. Mech. Sci. 43, 487–504.

Chen, H., Zhou, X., Shoumura, S., Emura, S., Bunai, Y., 2010. Age- and gender-dependent changes in three-dimensional microarchitecture of cortical and trabecular bone at the human femoral neck. Osteoporos Int. 21, 627–636.

Christensen, R. M., 1986. Mechanics of low density materials. J. Mech. Phys. Solids 34 (6), 563–578.

Chuang, C.-H., Huang, J.-S., 2002. Elastic moduli and plastic collapse strength of hexagonal honeycombs with plateau borders. Int. J. Mech. Sci. 44, 1827–1844.

Combaz, E., Rossoll, A., Mortensen, A., 2010. Hole and notch sensitivity of aluminium replicated foam. Acta Mater. 59 (2), 572–581.

Crisfield, M. A., 1991a. The 'eccentricity' issue in the design of beam, plate and shell elements. Communications in Appl. Num. Meth. 7, 47–56.

Crisfield, M. A., 1991b. Non-linear finite element analysis of solids and structures: Essentials. Vol. 1. John Wiley & Sons.

Crisfield, M. A., 1997. Non-linear finite element analysis of solids and structures: Advanced topics. Vol. 2. John Wiley & Sons.

Croce, L. D., Venini, P., Nascimbene, R., 2003. Numerical simulation of an elasto-plastic plate via mixed finite elements. J. Eng. Mathematics 46, 69–86.

Degischer, H.-P., Kriszt, B., 2002. Handbook of Cellular Metals. Wiley-VCH Verlag GmbH & Co., Weinheim.

Deshpande, V. S., Fleck, N. A., 2000. Isotropic constitutive models for metallic foams. J. Mech. Phys. Solids 48, 1253–1283.

Despois, J. F., Mueller, R., Mortensen, A., 2004. Uniaxial deformation of microcellular metals. Acta Mater. 54, 4129–4142.

Dillard, T., Forest, S., Ienny, P., 2006. Micromorphic continuum modelling of the deformation and fracture behaviour of nickel foams. Eur. J. Mech. A Solids 25, 526–549.

Dillard, T., Nguyen, F., Maire, E., Salvo, L., Forest, S., Bienvenu, Y., Bartout, J.-D., Croset, M., Dendievel, R., Cloetens, P., 2005. 3D quantitative image analysis of open-cell nickel foams under tension and compression loading using X-ray microtomography. Phil. Mag. A 85, 2147–2175.

Ehrlich, D., Armero, F., 2005. Finite element methods for analysis of softening plastic hinges in beams and frames. Computational Mechanics 35, 237–264.

Fleck, N. A., Olurin, O. B., Chen, C., Ashby, M. F., 2001. The effect of hole size upon the strength of metallic and polymeric foams. J. Mech. Phys. Solids 49, 2015–2030.

Free Online Pictures, 2010. Naturall honeycomb. http://thundafunda.com/33/travel-world-pictures/Honeycomb.php.

Gent, A. N., Thomas, A. G., 1959. The deformation of foamed elastic materials. J. Appl. Polym. Sci. 1, 107–113.

Gibson, L. J., 2000. Mechanical behaviour of metallic foams. Annu. Rev. Mater. Sci. 30, 191–227.

Gibson, L. J., Ashby, M. F., 1982. The mechanics of three-dimensional cellular materials. Proc. R. Soc. Lond. A 382, 43–59.

Gibson, L. J., Ashby, M. F., 1997. Cellular Solids, 2nd Edition. Cambridge University Press, Cambridge.

Gibson, L. J., Ashby, M. F., Schajer, G. S., 1982. The mechanics of two-dimensional cellular materials. Proc. R. Soc. Lond. A 382, 25–42.

Gibson, L. J., Ashby, M. F., Zhang, J., Triantafilliou, T. C., 1989. Failure surfaces for cellular materials under multi-axial loads-I. modeling. Int. J. Mech. Sci. 31 (9), 635–663.

Gioux, G., McCormack, T. M., Gibson, L. J., 2000. Failure of aluminum foams under multiaxial loads. Int. J. Mech. Sci. 42 (6), 1097–1117.

Gong, L., Kyriakides, S., Jang, W. Y., 2005. Compressive response of open-cell foams. Part-I: Morphology and elastic properties. Int. J. Solids Struct. 42, 1355–1379.

Grenestedt, J. L., 1998. Influence of wavy imperfections in cell walls on elastic stiffness of cellular solids. J. Mech. Phys. Solids 46 (1), 29–50.

Harders, H., Hupfer, K., Rosler, J., 2005. Influence of cell wall shape and density on the mechanical behaviour of 2D foam structures. Acta Mater. 53, 1335–1345.

Harte, A. M., Fleck, N. A., Ashby, M. F., 1999. Fatigue failure of an open cell and a closed cell aluminium alloy foam. Acta Met. Matrer. 47 (8), 2511–2524.

Harwel Subroutine Library, 2007. A Collection of Fortran codes for large-scale scientific computation. http://www.hsl.rl.ac.uk.

Hildebrand, T., Laib, A., Müller, R., Dequeker, J., Rüegsegger, P., 1999. Direct three-dimensional morphometric analysis of human cancellous bone: microstructural data from spine, femur, iliac crest and calcaneus. J. Bone Miner. Res. 14 (7), 1167–1174.

Huang, J., Chang, F., 2005. Effects of curved cell edges on the stiffness and strength of two-dimensional cellular solids. Comp. Str. 69, 183–191.

Intel MKL, 2007. Intel Math Kernel library. http://software.intel.com/en-us/intel-mkl/.

Jinnai, H., Watashiba, H., Kajihara, T., Nishikawa, Y., Takahashi, M., Ito, M., 2002. Surface curvatures of trabecular bone microarchitecture. Bone 30 (1), 191–194.

Kim, H. S., Al-Hasani, S. T. S., 2001. A morphological elastic model of general hexagonal columnar structures. Int. J. Mech. Sci. 43, 1027–1060.

Kim, H. S., Al-Hasani, S. T. S., 2002. The effect of doubly tapered strut morphology on the plastic yield surface of cellular materials. Int. J. Mech. Sci. 44, 1559–1581.

Koplik, J., Needleman, A., 1988. Void growth and coalescence in porous plastic solids. Int. J. Solids Struct. 24 (8), 835–853.

Krishna, B. V., Bose, S., Bandyopadhyay, A., 2007. Strength of open-cell 6101 aluminium foams under free and constrained compression. Mat. Sci. Eng. A 452-453, 178–188.

Landau, L. D., Lifshitz, E. M., 1959. The theory of elasticity. Addison-Wesley.

Lehmhus, D., Banhart, J., 2003. Properties of heat-treated aluminium foams. Mat. Sci. Eng. A 349, 98–110.

Li, K., Gao, X. L., Subhash, G., 2006. Effects of cell shape and strut cross-sectional area variations on the elastic properties of three-dimensional open-cell foams. J. Mech. Phys. Solids 54, 783–806.

Liu, C., Huang, Y., Stout, M. G., 1997. On the asymmetric yield surface of plastically orthotropic materials: A phenominological study. Acta Mater. 45, 2397–2406.

Mangipudi, K. R., Onck, P. R., 2006. Fracture of metal foams. In: Besson, J., Monieau, D., Speglich, D. (Eds.), Local Approach to Fracture. 9th European Mechanics of Materials Conference, pp. 193–196.

Mangipudi, K. R., Onck, P. R., 2011a. Multiscale modelling of fracture in two-dimensional metallic foams. J. Mech. Phys. Solids 59 (7), 1437–1461.

Mangipudi, K. R., Onck, P. R., 2011b. Notch sensitivity of ductile metallic foams: A computational study. Acta Mater. 59 (19), 7356–7367.

Mangipudi, K. R., Van Buuren, S. W., Onck, P. R., 2010. The microstructural origin of strain hardening in two-dimensional open-cell metal foams. Int. J. Solids Struct. 47 (16), 2081–2096.

Marante, M. E., Picon, R., Florez-Lopez, J., 2004. Analysis of localization in frame members with plastic hinges. Int. J. Solids Struct. 41, 3961–3975.

Marchi, C. S., Despois, J.-F., Mortensen, A., 2004. Uniaxial deformation of open-cell aluminum foam: the role of internal damage. Acta Mater. 52, 2895–2902.

Marchi, C. S., Mortensen, A., 2001. Deformation of open-cell aluminum foam. Acta Mater. 49, 3959–3969.

Markaki, A. E., Clyne, T. W., 2001. The effect of cell wall microstructure on the deformation and fracture of aluminium-based foams. Acta Mater. 49, 1677–1686.

McCullough, K. Y. G., Fleck, N. A., Ashby, M. F., 1999a. Toughness of aluminium alloy foams. Acta Mater. 47 (8), 2331–2343.

McCullough, K. Y. G., Fleck, N. A., Ashby, M. F., 1999b. Uniaxial stress-strain behaviour of aluminium alloy foams. Acta Mater. 47 (8), 2323–2330.

Migliaccio, S., Brama, M., Spera, G., 2007. The differential effects of bisphosphonates, SERMS (selective estrogen receptor modulators), and parathyroid hormone on bone remodelling in osteoporosis. Clinical Intervensions in Aging 2 (1), 55–64.

Miller, R. E., 2000. A continuum plasticity model for the constitutive and indentation behaviour behaviour of foamed metals. Int. J. Eng. Sci. 42, 729–754.

Motz, C., Pippan, R., 2001. Deformation behaviour of closed-cell aluminium foams in tension. Acta Mater. 49, 2463–2470.

Motz, C., Pippan, R., 2002. Fracture behaviour and fracture toughness of ductile closed-cell metallic foams. Acta Mater. 50, 2013–2033.

Neff, P., Forest, S., 2007. A geometrically exact micromorphic model for elastic metallic foams accounting for affine microstructure. Modelling, existance of minimizers, identification of moduli and computational results. J. Elast. 87, 239–276.

Nieh, T. G., Higashi, K., Wadsworth, J., 2000. Effect of cell morphology on the compressive properties of open-cell aluminium foams. Mat. Sci. Eng. A 283, 105–110.

Olurin, O. B., Fleck, N. A., Ashby, M. F., 2001. Tensile and compressive failure of notched cellular foams. Adv. Eng. Mater. 3 (1-2), 55–58.

Onck, P. R., 2001a. Application of a continuum constitutive model to metallic foam DEN-specimens in compression. Int. J. Eng. Sci. 43, 2947–2959.

Onck, P. R., 2001b. Notch-strengthening in two-dimensional foams. J. Phys. IV 11, 211–217.

Onck, P. R., 2003. Scale effects in cellular metals. MRS Bulletin 28 (4), 279–282.

Onck, P. R., Andrews, E. W., Gibson, L. J., 2001. Size effects in ductile cellular solids. Part I: modelling. Int. J. Mech. Sci. 43, 681–699.

Onck, P. R., Bastawros, A., 2000. Notch effects in metal foams. In: Miannay, D., Costa, P., Francois, D., Pineau, A. (Eds.), Advances in mechanical behaviour, plasticity and damage. Proc. EUROMAT, Elsevier, Amsterdam, pp. 717–722.

Onck, P. R., Merkerk, R. V., De Hosson, J. Th. M., 2004. Fracture of metal foams: In-situ testing and numerical modeling. Adv. Eng. Mater. 6, 429–431.

Ostoja-Starzewski, M., 1987. Graph approach to the constitutive modelling of heterogeneous solids. Mech. Research Commu. 14 (4), 255–262.

Papka, S. D., Kyriakides, S., 1994. In-plane compressive response and crushing of honeycomb. J. Mech. Phys. Solids 42 (10), 1499–1532.

Paserin, V., Marcuson, S., Shu, J., Wilkinson, D., 2004. CVD technique for Inco nickel foam production. Adv. Eng. Mater. 6 (6), 454–459.

Paul, A., Seshacharyulu, T., Ramamurty, U., 1999. Tensile strength of a closed-cell al foam in the presence of notches and holes. Scripta Mater. 40 (7), 809–814.

Pierce, D., Shih, C. F., Needleman, A., 1984. A tangent modulus method for rate dependent solids. Computers & Structures 18 (5), 875–887.

Prakash, O., Sang, H., Embury, J. D., 1995. Structure and properties of Al-SiC foam. Mater. Sci. Eng. A 199 (2), 195 – 203.

Ramamurty, U., Kumaran, M., 2004. Mechanical property extraction through conical indentation of a closed-cell aluminum foam. Acta Meter. 52 (1), 181–189.

Ross, P. D., Davis, J. W., Vogel, J. M., Washich, R. D., 1990. A critical review of bone mass and the risk of fractures in osteoporosis. Calcif Tissue Int. 46, 149–161.

Scheyvaerts, F., 2008. Multiscale modelling of ductile fracture in hetrogeneous metallic alloys. Ph.D. thesis, Universite Catholique de Louvain, Belgium.

Schmidt, I., Fleck, N. A., 2001. Ductile fracture of two-dimensional cellular structures. Int. J. Fracture 111, 327–342.

Schmidt, I., Richter, C., Gross, D., 2003. Ductile crack growth in metallic foams. In: Hutter, K., Baaser, H. (Eds.), Lecture Notes in Applied and Computational Mechanics. Vol. 10. Springer, pp. 363–380.

Seki, Y., Schneider, M. S., Meyers, M. A., 2005. Structure and mechanical behavior of a toucan beak. Acta Mater. 53 (20), 5281–5296.

Siegmund, T., Allen, M. R., Burr, D. B., 2010. Can deterministic mechanical size efects contribute to fracture and microdamage accumulation in trabecular bone? J. Theor. Biology 265, 202–210.

Silva, M. J., Gibson, L. J., 1997a. The effect of non-periodic microstructure and defects on the compressive strength of two-dimensional cellular solids. Int. J. Mech. Sci. 39 (5), 549–563.

Silva, M. J., Gibson, L. J., 1997b. Modeling the mechanical behavior of vertibral trabecular bone: effects of age-related changes in microstructure. Bone 21, 191–199.

Silva, M. J., Hayes, W. C., Gibson, L. J., 1995. The effect of non-periodic microstructure on the elastic properties of two-dimensional cellular solids. Int. J. Mech. Sci. 37 (11), 1161–1177.

Simone, A. E., Gibson, L. J., 1997. The compressive behaviour of porous copper made by the GASAR process. J. Mater. Sci. 32 (2), 451–457.

Simone, A. E., Gibson, L. J., 1998. Aluminum foams produced by liquid-state processes. Acta Meter. 46 (9), 3109–3123.

Sridhar, I., Fleck, N. A., 2005. The multiaxial yield behaviour of an aluminium foam. J. Mater. Sci. 40, 4005–4008.

Sugimura, Y., Meyer, J., He, M. Y., H. Bart-Smith, J. G., Evans, A. G., 1997. On the mechanical performance of closed cell Al alloy foams. Acta Mater. 45 (12), 5245–5259.

Tekoğlu, C., 2007. Size effects in cellular solids. Ph.D. thesis, University of Groningen, The Netherlands.

Tekoğlu, C., Gibson, L. J., Pardoen, T., Onck, P. R., 2010. Size effects in foams: Experiments and modelling. Prog. Mater. Sci. 56 (2), 109–138.

Tekoğlu, C., Onck, P. R., 2005. Size effects in the mechanical behaviour of cellular materials. J. Mater. Sci. 40, 5911–5917.

Tekoğlu, C., Onck, P. R., 2008. Size effects in two-dimensional Voronoi foams: A comparison between generalized continua and discrete models. J. Mech. Phys. Solids 56, 3541–3564.

Thornton, P. H., Magee, C. L., 1975. The deformation of aluminium foams. Metall. Trans. A 6, 1253–1263.

Triantafilliou, T. C., Zhang, J., Shercliff, T. L., Gibson, L. J., Ashby, M. F., 1989. Failure surfaces for cellular materials under multi-axial loads-II. comparison of models with experiment. Int. J. Mech. Sci. 31 (9), 665–678.

Van Buuren, S., 2007. Modelling deformation properties of 2D aluminium foams. Master's thesis, University of Groningen, The Netherlands.

Van Merkerk, R., 2002. Fracture of metal foams. Master's thesis, University of Groningen, The Netherlands.

Wang, Y., Cuitiño, A. M., 2000. Three-dimensional nonlinear open-cell foams with large deformations. J. Mech. Phys. Solids 48, 961–988.

Warren, W. E., Kraynik, A. M., 1987. Foam mechanics: the linear elastic response of two-dimensional spatially periodic cellular materials. Mech. Mater. 6, 27–37.

Warren, W. E., Kraynik, A. M., 1988. The linear elastic properties of open-cell foams. J. Appl. Mech. 55, 341–346.

Warren, W. E., Kraynik, A. M., Stone, C. M., 1989. A constitutive model for two-dimensional nonlinear elastic foams. J. Mech. Phys. Solids 37 (6), 717–733.

Wicklein, M., Thoma, K., 2005. Numerical investigations of the elastic and plastic behaviour of an open-cell aluminium foam. Mat. Sci. Eng. A 397, 391–399.

Wriggers, P., 2008. Nonlinear finite element methods. Springer-Verlag, Berlin.

Zhou, J., Allameh, S., Soboyejo, W. O., 2005. Microscale testing of the strut in open-cell aluminium foams. J. Mater. Sci. 40, 429–439.

Zhou, J., Shrotriya, P., Soboyejo, W. O., 2004. Mechanisms and mechanics of compressive deformation in open-cell al foams. Mech. Mater. 36, 781–797.

Zhu, H. X., Hobdell, J. R., Windle, A. H., 2001a. Effects of cell irregularity on the elastic properties of 2D Voronoi honeycombs. J. Mech. Phys. Solids 49, 857–870.

Zhu, H. X., Thorpe, S. M., Windle, A. H., 2001b. The geometrical properties of irregular two-dimensional Voronoi tessellations. Phil. Mag. A 81 (12), 2765–2783.

Zienkiewicz, O. C., Cormeau, I. C., 1974. Visco-plasticity–plasticity and creep in elastic solids–a unified numerical solution approach. Int. J. Num. Meth. Eng. 8, 821–845.

Zienkiewicz, O. C., Taylor, R. L., 2000. The finite element method: Vol. 1, The Basis, 5th Edition. Butterworth-Heinemann, Oxford.

Publications

Journal publications

1. **Mangipudi, K. R.**, Van Buuren, S. W., Onck, P. R., 2010. The microstructural origin of strain hardening in two-dimensional open-cell metal foams. Int. J. Solids Struct. 47 (16), 2081–2096.

2. **Mangipudi, K. R.**, Onck, P. R., 2011. Multiscale modelling of fracture in two-dimensional metallic foams. J. Mech. Phys. Solids 59 (7), 1437–1461.

3. **Mangipudi, K. R.**, Onck, P. R., 2011b. Notch sensitivity of ductile metallic foams: A computational study. Acta Mater. 59 (19), 7356–7367.

4. **Mangipudi, K. R.**, Onck, P. R., Tensile failure of two-dimensional quasi-brittle foams, submitted to Int. J. Solids Struct.

Conference proceedings

1. **Mangipudi, K. R.**, Onck, P. R., 2010. Multi-scale modelling of fracture in open-cell metal foams, Mechanics of Microstructured Solids 2, Lecture Notes in Applied and Computational Mechanics, Ed. J-F. Ganghoffer, F. Pastrone, Vol 50, p29-36, Springer Berlin, DOI:10.1007/978-3-642-05171-5.

2. Onck, P. R., **Mangipudi, K. R.**, 2009. The effect of cellular architecture on the ductility and strength of metal foams, MRS symposium LL: Architectured Multifunctional Materials, Vol 1188, p29-34, DOI:10.1557/PROC-1188-LL02-03.

3. **Mangipudi, K. R.**, Onck, P. R., 2007. Fracture of open-cell metal foams: a multiscale approach, Proceedings of the IUTAM symposium on Mechanical properties of cellular materials, Ed. Han Zhao, N.A. Fleck, Springer, DOI:10.1007/978-1-4020-9404-0.

4. **Mangipudi, K. R.**, Amsterdam, E., De Hosson, J. Th. M., Onck, P. R. Multiscale modelling of fracture in open-cell metal foams, Proceedings of MetFoam 2007, the 5th International Conference on Porous Metals and Metallic Foams, Ed. L.P. Lefebbre, J. Banhart, D.C. Dunand, DEStech Publications, 2007.

5. **Mangipudi, K. R.**, Onck, P. R., 2006. Fracture of metal foams. In: Besson, J., Monieau, D., Speglich, D. (Eds.), Local Approach to Fracture. 9th European Mechanics of Materials Conference, pp. 193–196.

Acknowledgments

My deepest gratitude goes to my advisor Prof. dr. ir. Patrick R. Onck, who has extended great support in several ways, both on scientific and personal matters. Thank you Patrick, for listening to all the technical difficulties patiently and for your consistent encouragement and guidance throughout this project. Your way of dissection of the physical problem is what I have most admired and will be the important one among the things I have learned from you.

I would like to thank Prof. Jeff De Hosson for many useful discussions during the 'Foam Group' meetings and for accepting to be a part of the reading committee. My sincere thanks are also due to Prof. Norman A. Fleck and Prof. A. Mortensen for kindly accepting to asses my thesis.

I am grateful to Prof. dr. ir. Erik van der Gissen for his consistent interest and for many scientific and technical suggestions. Thank you Erik, for your critical remarks during the 'long' μMeχ group meetings. I would also like to thank our secretary Mrs. Ria Sibma for her help in numerous official matters ranging from Visa to local city administration. Many thanks are also due to our system administrators Martin, Radu and Dogan.

I would like to thank the fellow μMeχ group members-Cihan, Teun, Andreas, Monica, Ratna, Ranjeet, Can, Goran, Ashok, Sietze, Jorn, Yor, Syed, Deep, Siamak, Sandeep and Siva-for the friendly working atmosphere, for those afternoon lunch discussions and the wonderful Christmas and Nerd dinners. I would also like to thank Emiel Amsterdam for all the scientific discussions we had during 'Foam group' meetings. Thanks to Sietze for your contribution to chapter 3 as a Masters student and for helping in translating the summary into Dutch.

I am grateful to my previous supervisor Prof. T. A. Abinandanan and Prof. U. Ramamurty, without whose advice and financial support I would have discontinued my Masters education.

The efforts and professionalism of Dr. Van Assen of Interne Geneeskunde, UMCG during my inpatient and outpatient treatment are highly appreciated. I would also like to thank Mrs. Anneke Toxopeus from International Service Desk of RuG for her help in resolving the issues with health insurance.

Ratna, thanks a lot for your help during my illness and for your time in debugging the codes; you have always been a special friend to me. Syed, it was wonderful to share the office with you and it was both fun and thought-provoking while discussing academic and non-academic topics. I would also like to thank all the Indian friends for the refreshing atmosphere. Upon my arrival in Netherlands, I was lucky to have Vimal, Ajit and Madhu from the Nijenborgh containers who provided a soft landing pad. Later, the social labyrinth of Jotsna, Ravi, Loknadh, Kasinadh, Sriram, Aneesh, Fiaz, Deepa, Ansar-Farida, Anartho-Nivedita, Pramod-Narmada, Ratna-Kalyani, Ranjeet-Kavita, Raj-Sirisha, Mandem & Zo., Syed-Mohsina and Martin-Alphine has worked as an excellent stress-relieving mechanism through sharing wonderful times celebrating many festivals and occasions far from the motherland.

I am indebted to my parents, Bhavaneswara Rao and Gayatri, who have sacrificed many of their comforts to offer me an opportunity to pursue my interests. My little daughter Snigdha, you were born almost at the time of submitting this thesis. Your those innocent smiles pushed the stress many miles away. Last but not least, a huge thanks to my better half, Madhuri. Without your love and support, it would have been very difficult to come this long way through the toughest times.

(Kodanda Ram Mangipudi)